

Aerotherm Final Report 7186-93-15

ASRM Nozzle Thermal Analysis

November 1993

For

**George C. Marshall Space Flight Center
National Aeronautics and Space Administration
Marshall Space Flight Center, AL 35812**

Contract Number: NAS8-39611

By

Forrest Strobel and Belinda King

**Aerotherm Corporation
1500 Perimeter Parkway
Suite 225
Huntsville, AL 35806**

Forward

The work described in this report was performed by the Huntsville Operations of Aerotherm Corporation from July 1992 to August 1993. A number of Aerotherm employees contributed to this effort, including: Belinda King, Robert Ross, Robert Shannon, and Forrest Strobel. The NASA Contracting Technical Representative for this program was Dallas Clark.

TABLE OF CONTENTS

Forward	i
List of Figures.....	iii
List of Tables	vi
1.0 INTRODUCTION.....	1
2.0 MOTOR DESCRIPTIONS.....	2
3.0 NOZZLE FLOWFIELD ANALYSIS.....	8
3.1 MNASA Nozzle Flowfield and Heating Rate Calculation	8
3.1.1 Material Interface Heating.....	22
3.1.2 Particle Flow Calculations.....	22
3.2 ASRM Nozzle Flowfield and Heating Rate Calculations.....	31
3.2.1 Material Interface Heating.....	48
3.2.2 Particle Flow Calculations.....	49
3.3 Surface Thermochemistry	62
4.0 NOZZLE MATERIAL RESPONSE CALCULATIONS.....	65
4.1 Analysis Procedures.....	65
4.2 MNASA Nozzle Erosion	67
4.3 ASRM Nozzle Erosion	72
4.4 ASRM Flex Seal Response	73
5.0 CONCLUSIONS.....	77
6.0 RECOMMENDATIONS.....	78
References	79
Appendix A.....	A1
Appendix B.....	B1

LIST OF FIGURES

Figure 1 MNASA Motor Configuration	2
Figure 2 MNASA Nozzle Configuration	3
Figure 3 ASRM Motor Configuration	3
Figure 4 ASRM Nozzle Configuration	4
Figure 5 Chamber Pressure for MNASA 48-5 Motor Firing.....	6
Figure 6 Estimated Chamber Pressure for ASRM.....	7
Figure 7 MNASA Nozzle Flow Analysis Grid	9
Figure 8 MNASA Nozzle Flow Velocities	10
Figure 9 MNASA Nozzle Pressure Contours.....	10
Figure 10 MNASA Nozzle Temperature Contours	11
Figure 11 MNASA Nozzle Mach Contours	11
Figure 12 MNASA Nozzle Boundary Layer Edge Velocity.....	14
Figure 13 MNASA Nozzle Boundary Layer Edge Pressure.....	14
Figure 14 MNASA Nozzle Boundary Layer Edge Temperature	15
Figure 15 MNASA Nozzle Cutoff Analysis Grid	15
Figure 16 Boundary Layer Edge Velocities for the Submerged Region	16
Figure 17 MNASA Nozzle Convective Heating Conditions	17
Figure 18 MNASA Nozzle Convective Heating Conditions as a Function of Axial Position.....	17
Figure 19 Submerged Region Convective Heating Conditions	19
Figure 20 MNASA Nozzle Thermal Analysis Locations	20
Figure 21 Augmented Heating Rates at the Exit Cone Material Interface	24
Figure 22 MNASA Particle Flow Grid.....	24
Figure 23 Particle Size Distributions from Reference 7	25
Figure 24 MNASA Particle Flow Results, Time = 0.0064 Second.....	27
Figure 25 MNASA Particle Flow Results, Time = 0.00765 Second.....	27
Figure 26 MNASA Particle Flow Results, Time = 0.0079 Second.....	28
Figure 27 MNASA Particle Flow Results, Time = 0.00885 Second.....	28
Figure 28 MNASA Particle Flow Results, Time = 0.0101 Second.....	29
Figure 29 MNASA Particle Flow Results, Time = 0.0103 Second.....	29
Figure 30 Particle Impact Conditions For the MNASA Nozzle	30
Figure 31 ASRM Nozzle Analysis Grid, Initial Grain Geometry	32
Figure 32 ASRM Nozzle Analysis Grid, EOB Grain Geometry.....	32
Figure 33 ASRM Nozzle Velocity Vectors, Initial Grain.....	33
Figure 34 ASRM Nozzle Pressure Contours, Initial Grain.....	34
Figure 35 ASRM Nozzle Temperature Contours, Initial Grain	34
Figure 36 ASRM Nozzle Mach Contours, Initial Grain	35
Figure 37 ASRM Nozzle Velocity Vectors, EOB Grain	35
Figure 38 ASRM Nozzle Pressure Contours, EOB Grain	36
Figure 39 ASRM Nozzle Temperature Contours, EOB Grain.....	36
Figure 40 ASRM Nozzle Mach Contours, EOB Grain.....	37
Figure 41 Boundary Layer Starting Point for ASRM Nozzle.....	37
Figure 42 ASRM Nozzle Edge Velocity.....	38
Figure 43 ASRM Nozzle Edge Pressure.....	39
Figure 44 ASRM Nozzle Edge Temperature	39

Figure 45 ASRM Nozzle Heat Transfer Coefficients.....	40
Figure 46 ASRM Nozzle Edge Velocity, Submerged Region.....	40
Figure 47 ASRM Nozzle Edge Pressure, Submerged Region	41
Figure 48 ASRM Nozzle Edge Temperature, Submerged Region.....	41
Figure 49 ASRM Nozzle Heat Transfer Coefficients, Submerged Region	42
Figure 50 Comparison of Heat Transfer Coefficients for Initial Grain and EOB Geometries.....	44
Figure 51 Comparison of Heat Transfer Coefficients for Initial Grain and EOB Geometries, Submerge Region	44
Figure 52 ASRM Nozzle Thermal Analysis Locations, Forward Region	45
Figure 53 ASRM Nozzle Thermal Analysis Locations, Aft Region	46
Figure 54 Augmented Heating Rates at the Exit Cone Material Interface	49
Figure 55 ASRM Nozzle Particle Flow Grid, Initial Grain Configuration	51
Figure 56 ASRM Nozzle Particle Flow Grid, Intermediate Grain Configuration	51
Figure 57 ASRM Nozzle Particle Flow Grid, EOB Grain Configuration.....	52
Figure 58 ASRM Particle Flow Results, Initial Grain 1 mm Particles, Time = 0.0090 Second.....	54
Figure 59 ASRM Particle Flow Results, Initial Grain 1 mm Particles, Time = 0.0116 Second.....	54
Figure 60 ASRM Particle Flow Results, Initial Grain 1 mm Particles, Time = 0.0343 Second.....	54
Figure 61 ASRM Particle Flow Results, Initial Grain 10 mm Particles, Time = 0.0086 Second.....	55
Figure 62 ASRM Particle Flow Results, Initial Grain 10 mm Particles, Time = 0.0104 Second.....	55
Figure 63 ASRM Particle Flow Results, Initial Grain 10 mm Particles, Time = 0.0195 Second.....	55
Figure 64 ASRM Particle Flow Results, Initial Grain 120 mm Particles, Time = 0.0082 Second.....	56
Figure 65 ASRM Particle Flow Results, Initial Grain 120 mm Particles, Time = 0.0110 Second.....	56
Figure 66 ASRM Particle Flow Results, Initial Grain 120 mm Particles, Time = 0.0163 Second.....	56
Figure 67 ASRM Particle Flow Results, End of Burn 1 mm Particles	57
Figure 68 ASRM Particle Flow Results, End of Burn 10 mm Particles.....	57
Figure 69 ASRM Particle Flow Results, End of Burn 120 mm Particles.....	57
Figure 70 ASRM Particle Flow Results, Intermediate Grain 120 mm Particles.....	58
Figure 71 ASRM Particle Flow Results, Initial Grain, 3.5 mm Particles.....	58
Figure 72 ASRM Particle Mass Fluxes.....	59
Figure 73 ASRM Particle Impact Angles	60
Figure 74 ASRM Particle Impact Velocities.....	60
Figure 75 Particle Mass Fluxes at ASRM Analysis Locations	61
Figure 76 Particle Impact Angles at ASRM Analysis Locations	61
Figure 77 Particle Impact Angles at ASRM Analysis Locations	62
Figure 78 Non Dimensional Ablation Rates for FM5055 Carbon Phenolic.....	63
Figure 79 Non Dimensional Ablation Rates for MX4996 Carbon Phenolic	63

Figure 80 Non Dimensional Ablation Rates for FM5939 Carbon Phenolic.....	64
Figure 81 Calculated Thermochemical Erosion Depths for the MNASA Nozzle	69
Figure 82 Combined Thermochemical and Particle Erosion Depths for the MNASA Nozzle.....	69
Figure 83 Impacting Particle Mass Fluxes for the MNASA Nozzle	70
Figure 84 TAD for MNASA nozzle	70
Figure 85 Calculated Erosion Depths for the ASRM Nozzle	74
Figure 86 Surface Angles for the MNASA and ASRM Nozzles	74
Figure 87 TAD for ASRM Nozzle	75
Figure 88 ASRM Nozzle Flex Seal Recession.....	75
Figure A-1 Comparison of Measured and Calculated TGA Data for MX4996 Carbon Phenolic.....	A2
Figure A-2 Estimated Specific Heat for MX4996.....	A3
Figure A-3 Thermal Conductivity of MX4996 Char Material.....	A5
Figure A-4 Comparison of Measured and Calculated TGA Data for FM5939 Low Density Carbon Phenolic.....	A6
Figure A-5 Estimated Specific Heat of FM5939 Low Density Carbon Phenolic.....	A7
Figure A-6 Thermal Conductivity for FM5939 Low Density Carbon Phenolic.....	A8
Figure B-1 Polyisoprene Surface Energy Balance	B4
Figure B-2 Polyisoprene Recession History.....	B4
Figure B-3 Polyisoprene In-depth Temperatures	B5
Figure B-4 Polyisoprene Thermal Conductivity	B5
Figure B-5 ASTHMA Analysis Grid for MNASA Flex Seal Specimen.....	B6

LIST OF TABLES

Table 1. Propellant Formulation.....	06
Table 2. Propellant Gas Formulation.....	08
Table 3 MNASA Boundary Layer Edge Conditions	13
Table 4 MNASA Nozzle Heating Conditions	21
Table 5 MNASA Nozzle Particle Impact Conditions.....	31
Table 6 ASRM Nozzle Heating Conditions	47
Table 7 ASRM Flex Seal Heating Conditions	48
Table 8 Comparison of Calculated and Approximated Heat Transfer Coefficients.....	48
Table 9 ASRM Nozzle Particle Analysis Cases	52
Table 10 Erosion and TAD Summary for the MNASA Nozzle	71
Table 11 Erosion and TAD Summary for the ASRM Nozzle	76
Table A-1 Decomposition Kinetics for MX4996 Carbon Phenolic	A2
Table A-2 Elemental Composition for MS4996 Carbon Phenolic.....	A3
Table A-3 Estimated Specific Heat for MX4996 Carbon Phenolic	A4
Table A-4 Resin Data.....	A4
Table A-5 Virgin Thermal Conductivity for MX4996 Carbon Phenolic	A4
Table A-6 Estimated Char Thermal Conductivity.....	A4
Table A-7 Decomposition Kinetics for FM5939 Low Density Carbon Phenolic	A5
Table A-8 Elemental Composition for FM5939 Low Density Carbon Phenolic.....	A6
Table A-9 Estimated Specific Heat for FM5939 Low Density Carbon Phenolic.....	A6
Table A-10 Resin Data.....	A7
Table A-11 Virgin Thermal conductivity for FM5930 Low Density Carbon Phenolic.....	A7
Table A-12 Char Thermal Conductivity for FM5939 Low Density Carbon Phenolic	A8

1.0 INTRODUCTION

This report describes results from the Nozzle Thermal Analysis (NTA) contract NAS8-39611 which has been performed for NASA/Marshall Space Flight Center in support of the Advanced Solid Rocket Motor (ASRM) development. The primary emphasis of this program has been to investigate regions of the ASRM nozzle which have potential thermal or surface erosion problems. This study has been performed with state of the art analysis tools developed by Aerotherm Corporation with specific application to solid rocket motors. Some of the tools are computer codes which are used throughout the industry and have become standards. Other of the tools have recently been developed for NASA under the Solid Propulsion Integrity Program (SPIP). Several areas of the ASRM nozzle have received special attention during this study. These areas include:

1. The submerged region of the nozzle which contains the flex seal.
2. The nozzle entrance region which is subjected to a severe particle impact environment.
3. The material interface region in the nozzle exit cone. This is the region where the exit cone material transits from standard density to low density carbon phenolic.
4. The aft region of the nozzle exit cone which may be subjected to particle impacts.

Study of these nozzle regions has been performed for both the subscale MNASA test motor and the full scale ASRM motor. The approach which has been taken in this program is to perform calculations for the MNASA motor and compare results to measured data. These comparisons have been made to calibrate the calculations and understand the phenomena occurring in this motor. With models developed and calibrated, calculations were then performed to evaluate the ASRM nozzle, especially the critical regions mentioned above. This report contains results from these calculations and describes the assumptions and analysis procedures which have been used.

The report is organized into six sections; section 2 contains a description of the MNASA and ASRM motors, their propellant and chamber operating conditions, Section 3 describes the flowfield calculations which have been performed for both of the nozzles, Section 4 describes the thermal and erosion calculations which have been performed, Section 5 presents conclusions, and Section 6 presents recommendations for aspects of the ASRM nozzle which need additional attention.

2.0 MOTOR DESCRIPTIONS

Figure 1 presents the motor and nozzle configuration used for the MNASA ASRM 48-5 test which is described in reference 1. A more detailed schematic of the nozzle is presented in Figure 2. This test motor has a short aft dome section which separates the motor chamber from the nozzle. The nozzle is a subscale test item with many features designed to simulate the full scale ASRM nozzle. The throat diameter of this nozzle is approximately 10 inches.

The ASRM 48-5 test was designed to evaluate a large variety of carbon phenolic materials. The materials of greatest interest for the present study are MX4996 standard density carbon phenolic and FM5939 low density carbon phenolic. This nozzle also contained a flexseal insulation specimen which consisted of polyisoprene shimmed with FM5055 carbon phenolic. This specimen was nonfunctional but was placed in the submerged region of the nozzle to simulate the expected environment for the full scale ASRM.

Figures 3 and 4 are similar presentations for the ASRM motor and nozzle. The major differences in the two configurations (i.e., MNASA vs. ASRM) are:

1. the position of the propellant grain relative to the nozzle
2. the location of the flex seal, and
3. the size of the two nozzles, the ASRM has a 54.488 inch throat diameter.

There are also many other less significant differences. The ASRM utilizes only two carbon phenolic materials, the standard density MX4996 and the low density FM5939.

The propellant formulation presented in Table 1 is used by both of these motors. This is an 88/19 (%solids/%aluminum) HTPB propellant. Figures 5 and 6 present the pressure traces for each of these motors. Figure 5 is the measured pressure for the ASRM 48-5 firing and Figure 6 is the estimated chamber pressure for the ASRM motor.

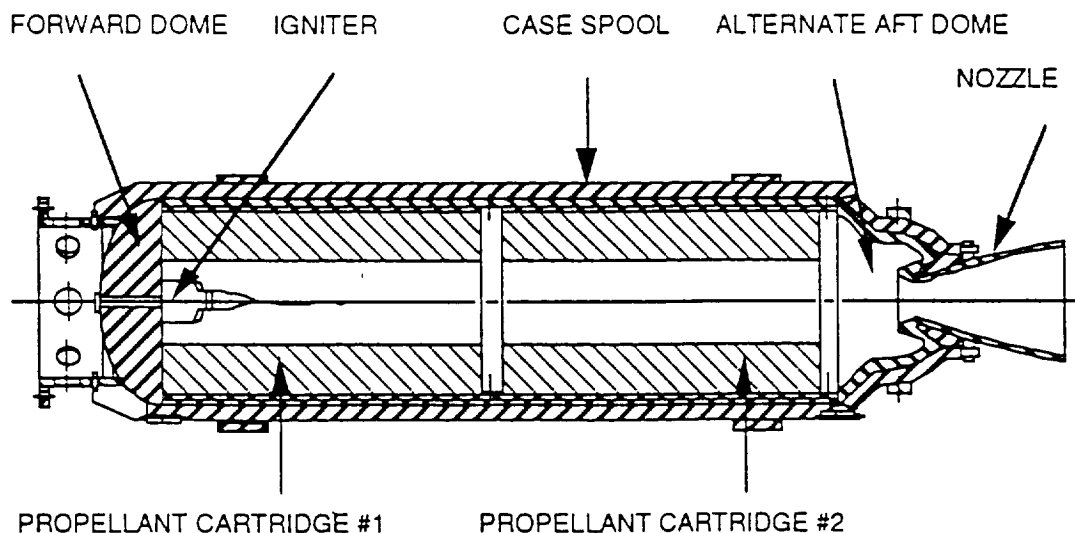


Figure 1. MNASA Motor Configuration

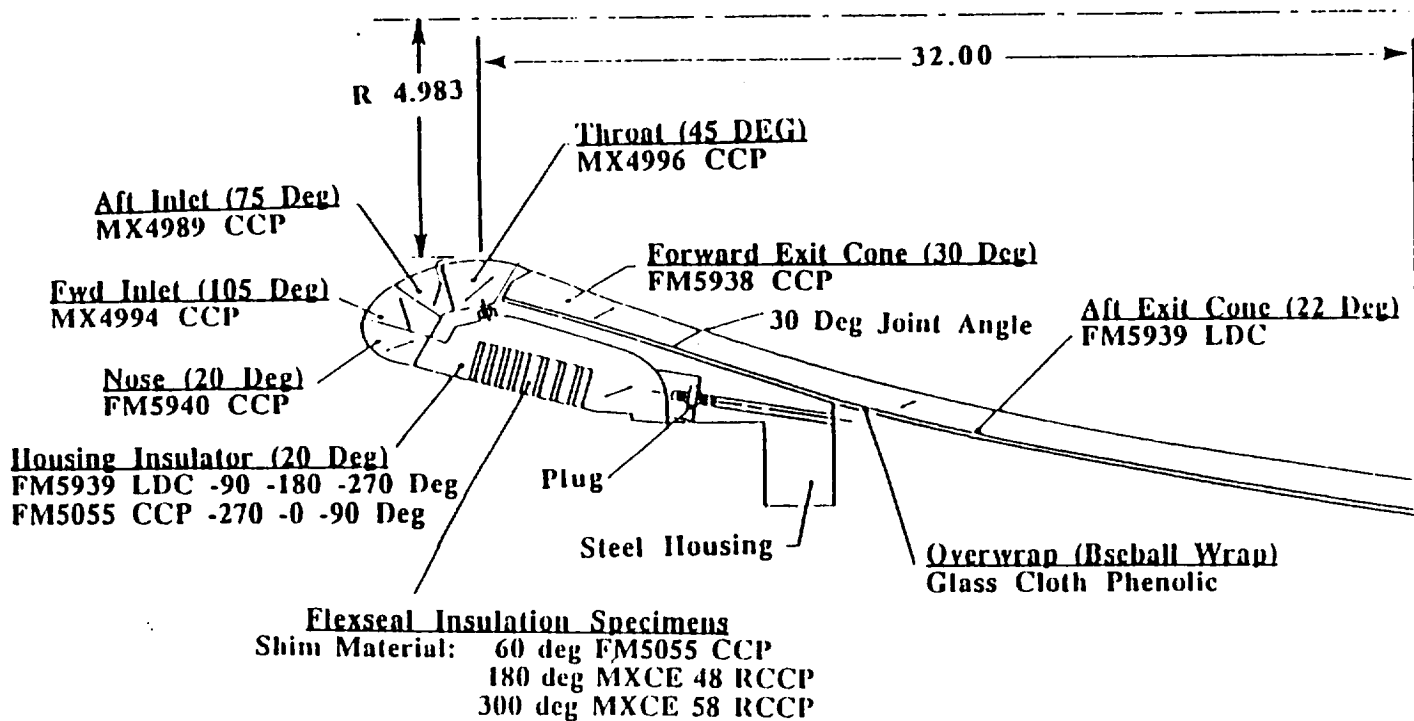


Figure 2. MNASA Nozzle Configuration

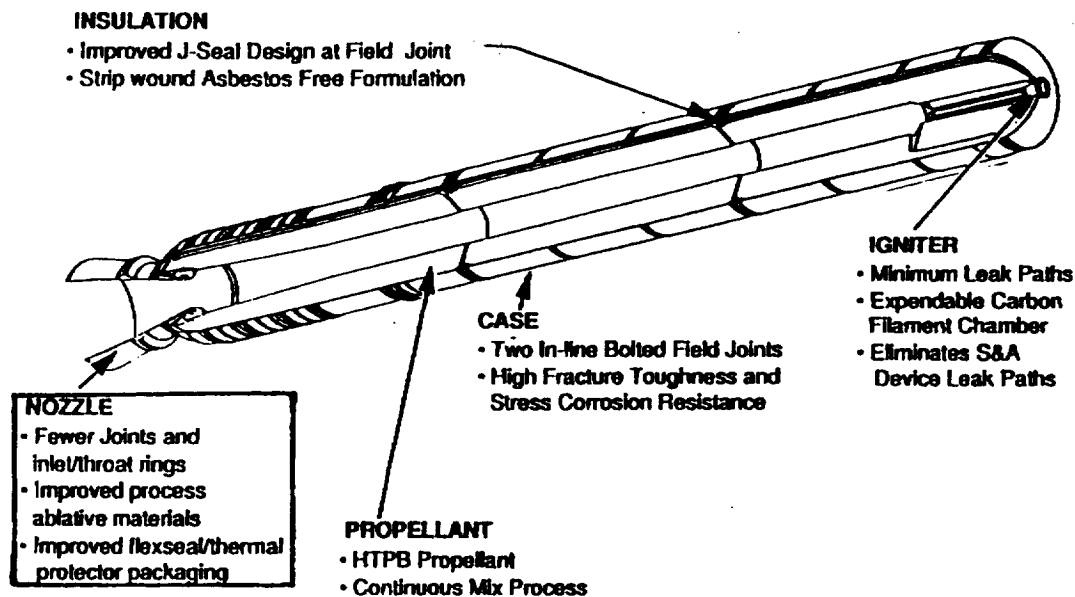


Figure 3. ASRM Motor Configuration

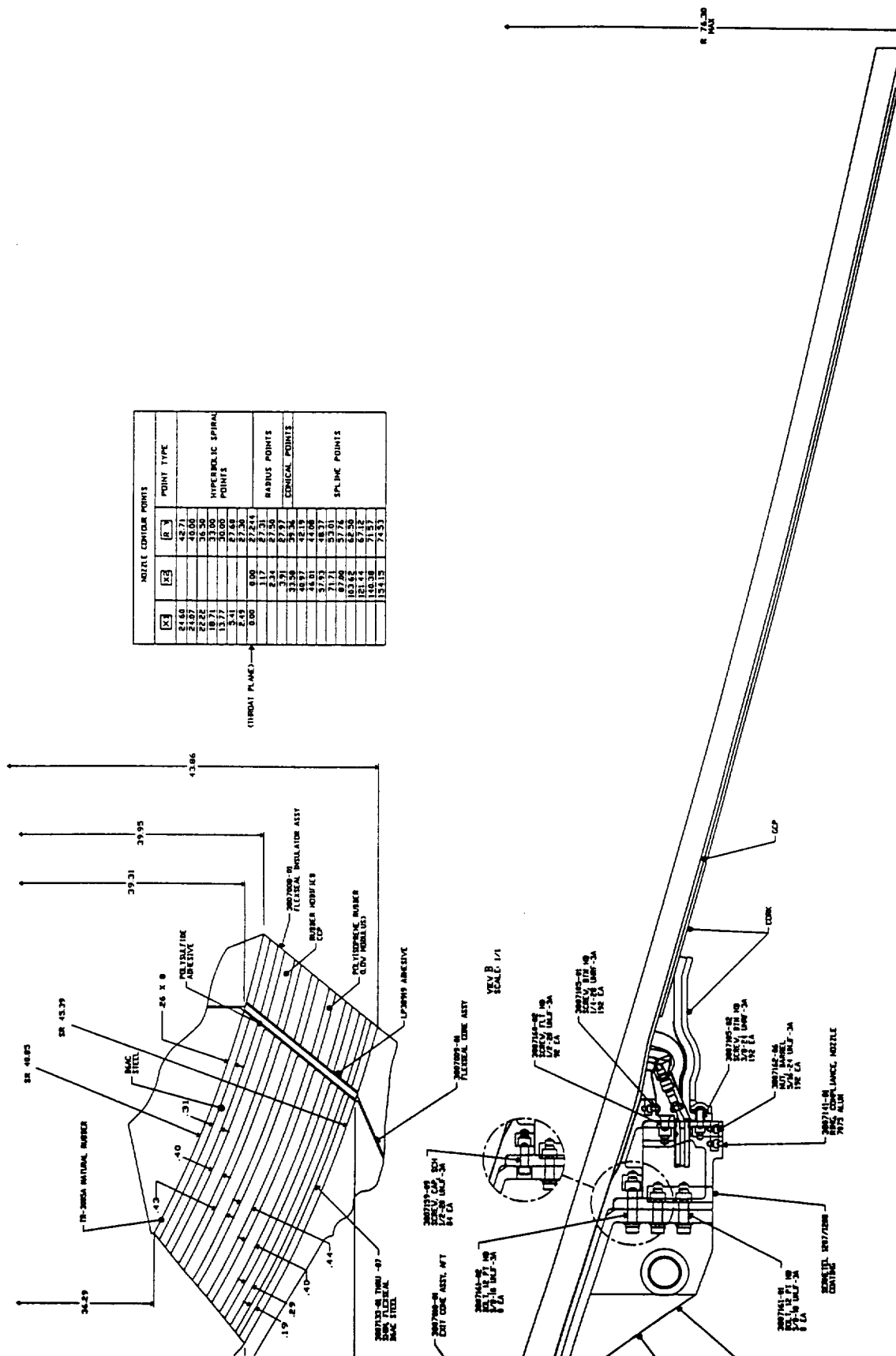


Figure 4. ASRM Nozzle Configuration (cont.)

Table 1. Propellant Formulation

Constituent		Weight Percentage
Ammonium Perchlorate	Content	68.93%
	Particle Size Distribution	180 μ 70% 20 μ 30%
Aluminum	Content	19%
	Particle Size	13 μ
	Particle Shape	Non-Spherical
HTPB Binder		12%
Iron Oxide		0.07%

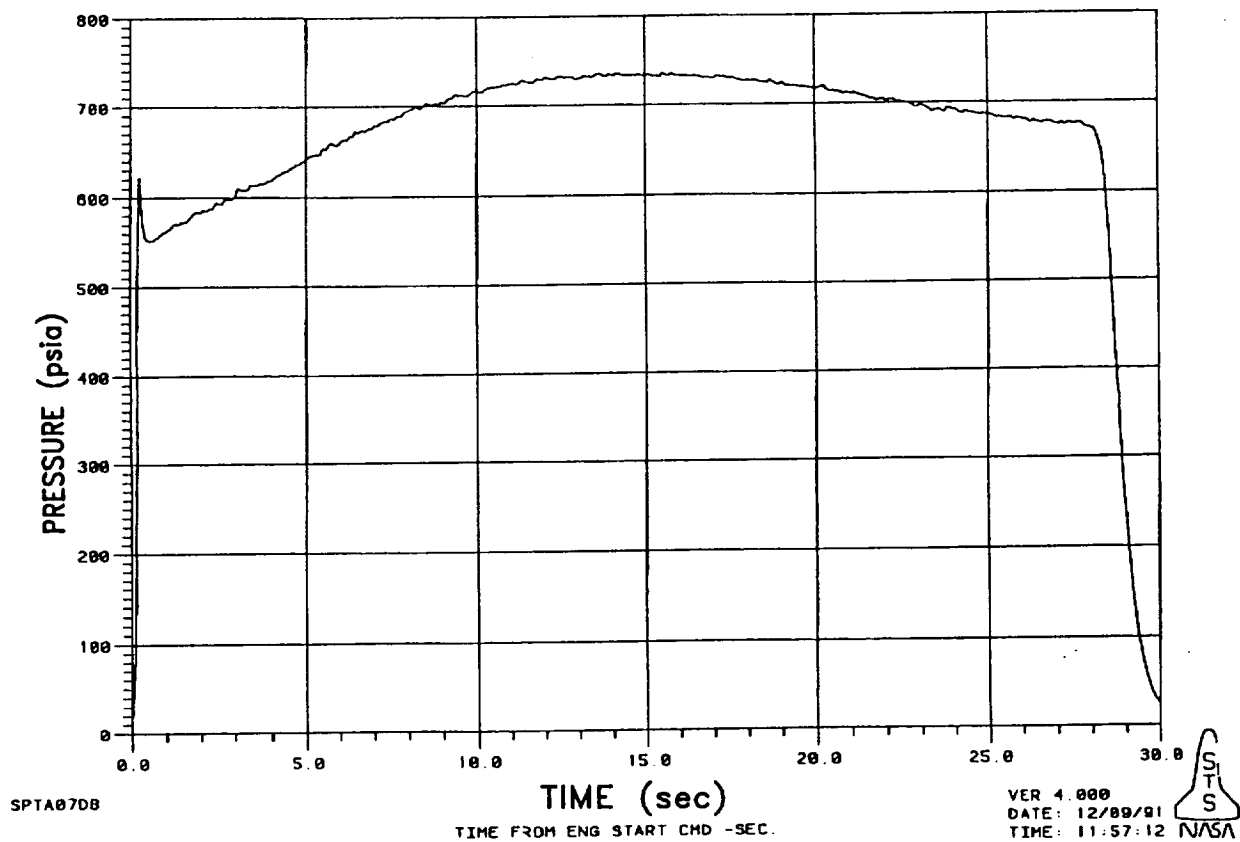


Figure 5. Chamber Pressure for MNASA 48-5 Motor Firing

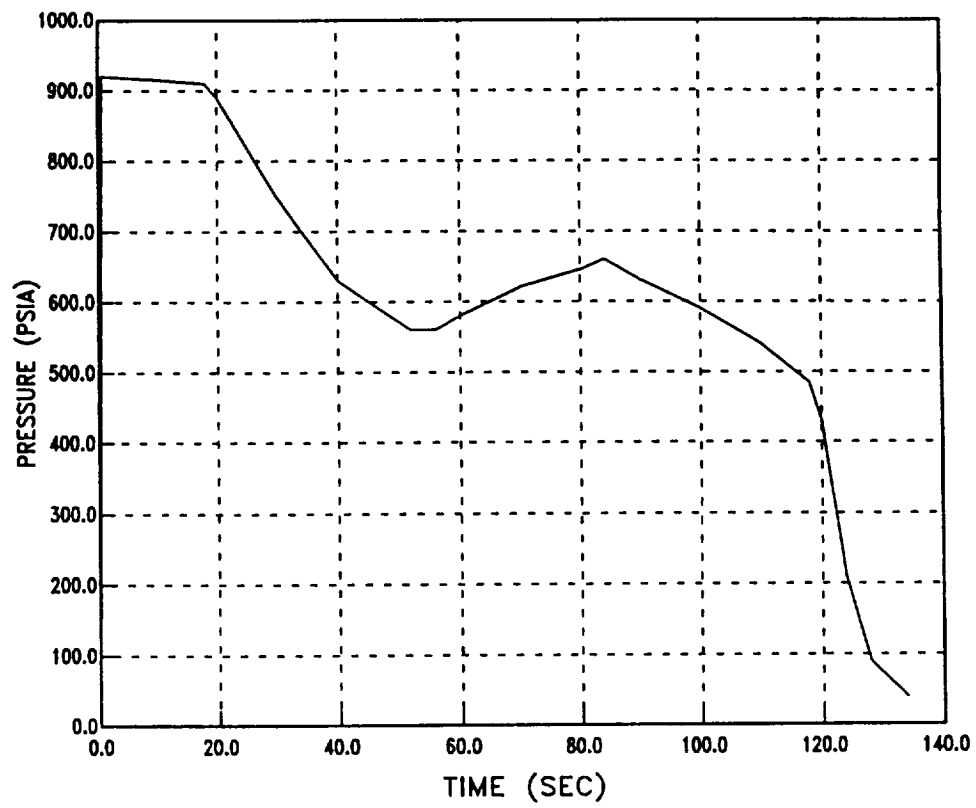


Figure 6. Estimated Chamber Pressure for ASRM

3.0 NOZZLE FLOWFIELD ANALYSIS

This section describes the flowfield analyses which have been conducted for both of the motors. This includes nozzle heating rate and particle flow analysis. This section will present the results from these calculations as well as describe the procedures which have been used. Calculations for the MNASA motor will be presented first followed by those for ASRM. Unless otherwise stated the analysis procedures for the two are identical.

3.1 MNASA Nozzle Flowfield and Heating Rate Calculations

Nozzle flowfield, heating rate, and surface thermochemistry calculations have been performed with the SPIP developed Nozzle AeroThermochemistry (NAT, Reference 2) computer code. This code is a coupled version of several other computer codes. The ACE module of the code is used to perform one dimensional isentropic flow solutions, surface thermochemistry solutions and provide inputs to the Navier Stokes solutions. The Navier Stokes solutions were performed with the KIVA module. These calculations all used the "Mollier" option in the code. With this option the code treats the propellant gas as a single species which has real gas properties which are determined by the ACE module. These properties are those for the gas in chemical equilibrium. This option was used because it greatly increases the efficiency of the KIVA calculations. This chemical equilibrium assumption has been found to yield acceptable heating rate results for solid rocket motors, i.e., chemical kinetic effects are insignificant. Table 2 presents the elemental composition used for the propellant gases. Some of the trace elements, e.g., iron have been ignored. This table also presents the average chamber pressure for the MNASA motor and the corresponding chamber temperature.

Table 2. Propellant Gas Composition

Element	Mole Fraction (%)
Hydrogen	41.58
Carbon	9.55
Nitrogen	6.82
Oxygen	27.27
Aluminum	8.06
Chlorine	6.71
$P_c = 45.4 \text{ atm}$	
$T_c = 6418^\circ \text{ R}$	

Figure 7 presents the analysis grid which was used to perform the flowfield calculation for the MNASA nozzle. This flow solution includes the aft dome as well as the nozzle submerged region. The analysis grid has been refined in regions where largest flow gradients are expected to occur. Results from the one dimensional isentropic flow solutions (ACE) were used as initial conditions and inflow conditions for the KIVA Navier Stokes calculation. The inflow conditions, temperature, density and velocity were applied

to the left hand side of the analysis grid. An ambient pressure of 1 atmosphere was applied as the outflow condition at the right hand side of the grid.

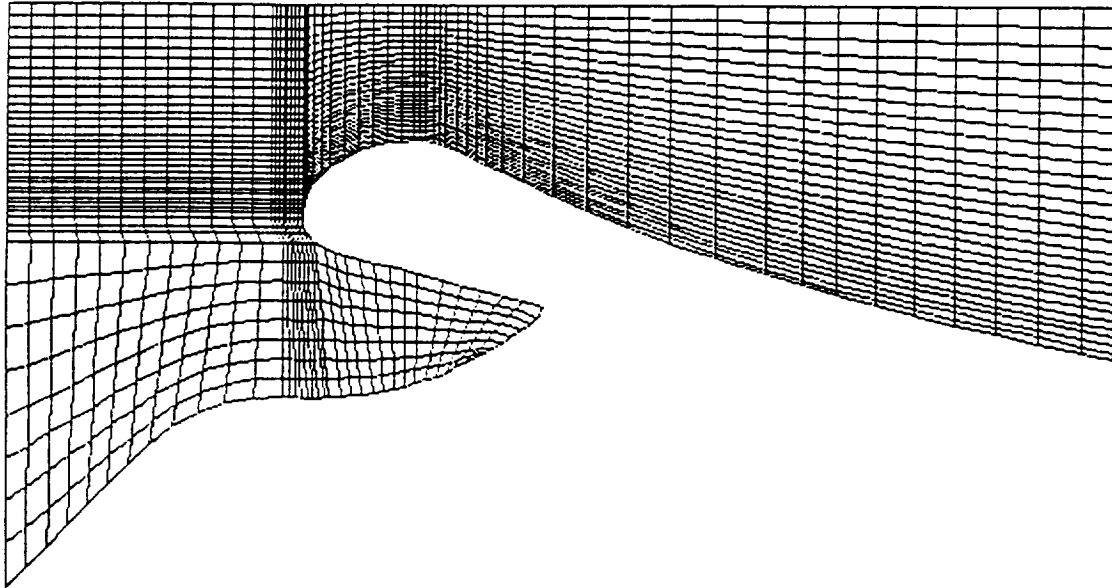


Figure 7. MNASA Nozzle Flow Analysis Grid

Results from the flow calculations are shown in Figures 8 through 11. Figure 8 presents flow velocities calculated for the nozzle. Figures 9 through 11 present pressure, temperature and Mach contours, respectively. Each figure identifies the values of the maximum and minimum contours as well as the increment, Δ , between each contour. The two dimensional nature of the flow is greatest just down stream of the nozzle throat.

These flow calculations for the MNASA nozzle required 2100 cycles. Each cycle is a small incremental step in time. These steps in time are necessary because the KIVA module is a time accurate Navier Stokes solver. A calculation will require a greater number of cycles to reach steady state depending on how far the initial conditions are from the steady state solution. For this computation, the flow in the submerged region did not completely reach steady state conditions. This was due in part to the various convergence criteria used in the calculation (The flow in the submerged region is very low velocity and tends to oscillate due to small variations in pressure. The pressure convergence criteria used for these calculations was $1.0E-04$. A smaller criteria is probably needed to totally eliminate the observed flow oscillations. However, the magnitude of these oscillations is small enough that the calculated heating conditions should bound the actual heating environments.)

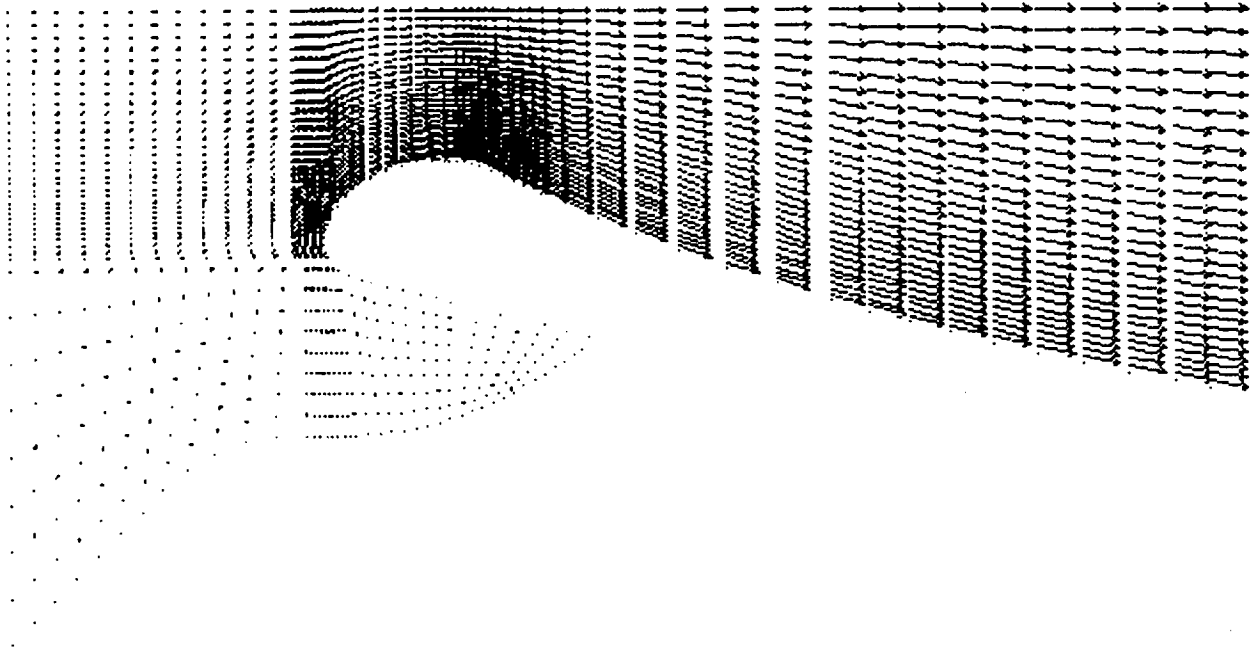


Figure 8. MNASA Nozzle Flow Velocities

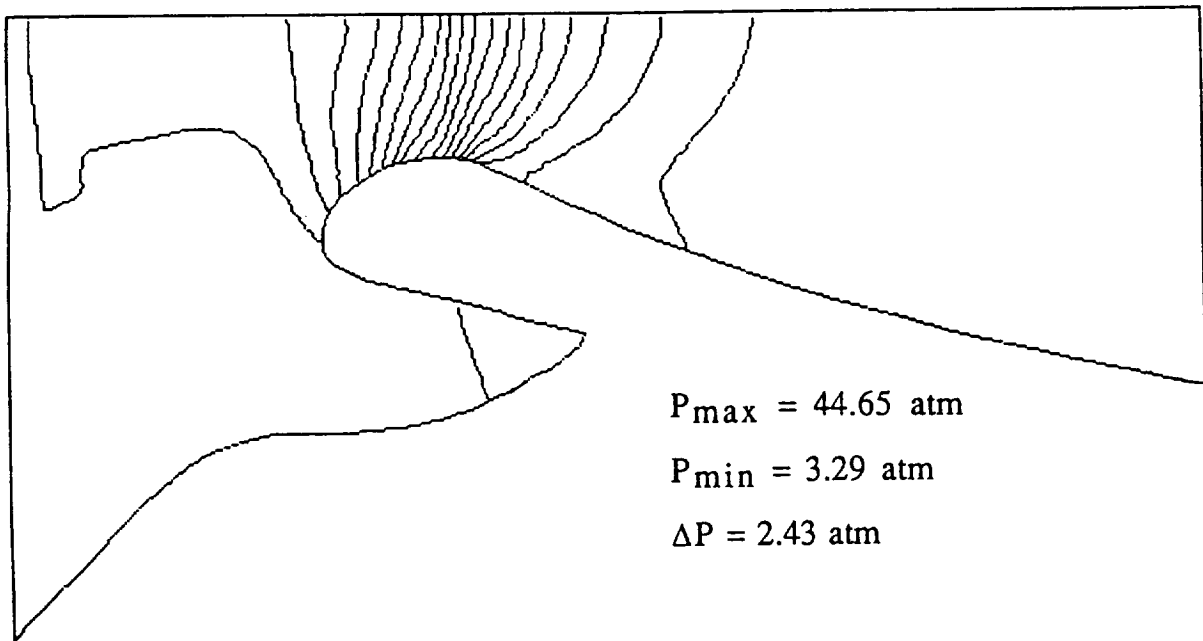


Figure 9. MNASA Nozzle Pressure Contours

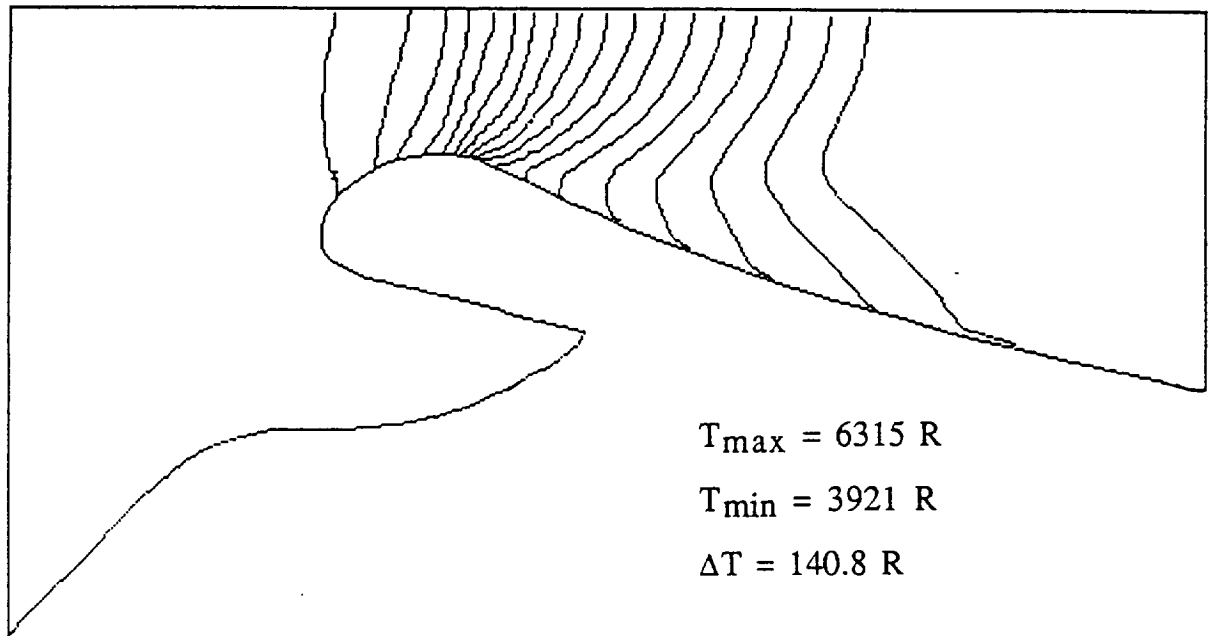


Figure 10. MNASA Nozzle Temperature Contours

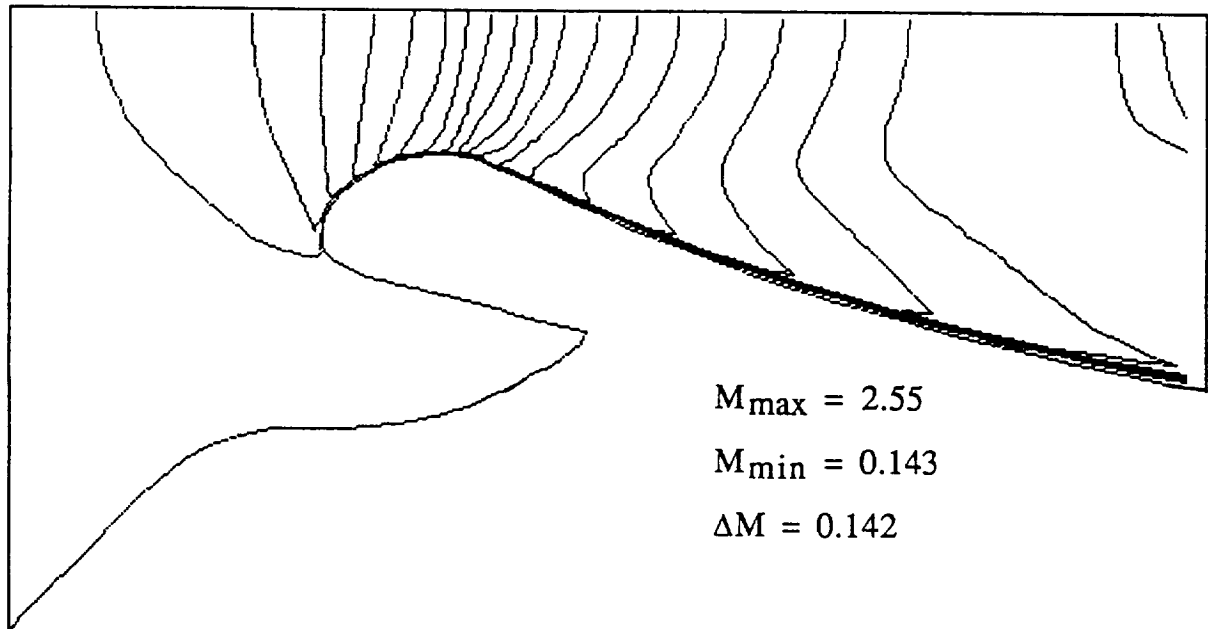


Figure 11. MNASA Nozzle Mach Contours

The results from the Navier Stokes solution were used as boundary layer edge conditions and the convective heating rates were then determined with the MEIT module in the code. This module uses law of the wall assumptions and a momentum energy integral technique (MEIT) to determine convective transfer rates. The boundary layer edge conditions are taken as the flow conditions calculated for the cell adjacent to the wall. The boundary layer starting point is specified by the NAT user and for these calculations was taken as the point deepest into the submerged region. The edge conditions calculated with the KIVA module are shown in Figures 12 through 14. These figures present the edge velocity, pressure and temperature as a function of streamlength measured from the boundary layer starting point. A summary of these results is also presented in Table 3. This table presents edge conditions as a function of station, axial position and streamlength. The nozzle stations will be identified later in Figure 20.

A second analysis grid was developed to more accurately calculate the flowfield in the submerged region of the nozzle as well as the throat entrance regions. This grid, which is shown in Figure 15, is referred to as the "cutoff" grid since it is terminated immediately aft of the nozzle throat. This grid is significantly refined compared to the grid presented in Figure 7. Calculations were performed with this grid for 3000 cycles. Even still, the fluctuating flows in the submerged region were not completely eliminated. Nevertheless, the flow did "steady out" significantly so that the flow conditions in this region could at least be bounded. Figure 16 presents velocities calculated in the submerged region of the nozzle for two points in time. The velocities in the submerged portion of the nozzle are on the order of 50 to 100 ft/sec.

Table 3. MNASA Boundary Layer Edge Conditions

Station	Axial Position (in)	Streamlength (in)	Ve (ft/sec)	Te (deg-R)	Pe (atm)
4	3.550	1.81	31.52	6401.3	44.90
5	2.477	2.91	65.99	6404.2	45.00
6	1.393	4.03	72.81	6398.2	44.70
7	0.365	5.09	89.03	6394.2	44.60
8	-0.701	6.19	107.2	6390.3	44.40
9	-1.923	7.44	182.0	6402.6	45.00
10	-2.863	8.42	272.5	6409.4	45.30
11	-3.815	9.48	459.4	6415.8	45.70
12	-4.232	10.50	1400.0	6373.9	45.70
13	-3.974	11.10	1305.0	6339.2	40.90
14	-3.520	11.80	2069.0	6271.0	37.50
15	-2.361	13.30	3112.6	6140.1	36.60
16	-1.681	14.00	3981.9	5990.2	29.70
17	-1.171	14.55	4369.0	5902.4	26.28
18	0.0	15.65	5313.0	5689.8	19.80
19	0.981	16.70	6381.2	5143.9	12.06
20	2.064	18.15	6714.9	4857.4	7.281
21	2.972	19.17	7098.1	4721.9	6.208
22	3.882	20.17	7389.8	4592.1	5.507
23	4.802	21.18	7582.6	4538.9	4.923
24	5.504	21.96	7706.7	4488.4	4.458
25	6.172	22.66	7810.8	4444.2	4.191
26	6.888	23.43	7917.4	4398.2	3.890
27	7.354	23.93	7979.5	4371.2	3.890
28	7.782	24.39	8033.2	4342.6	3.439
29	8.292	24.93	8097.3	4319.6	3.439
30	9.223	25.92	8199.6	4271.2	3.439
31	10.182	26.94	8298.8	4222.5	3.056
32	11.148	27.95	8358.8	4182.8	2.732
33	12.088	28.94	8417.3	4146.7	2.732
34	14.966	32.00	8651.5	4028.0	2.297
35	17.875	34.95	8942.1	3919.1	1.965
36	20.789	38.00	9017.3	3821.3	1.711
37	23.756	41.00	9123.0	3751.5	1.550
38	26.706	44.00	9226.7	3698.2	1.471
39	29.675	47.00	9307.7	3645.8	1.370
40	31.005	48.33	9346.7	3621.9	1.347

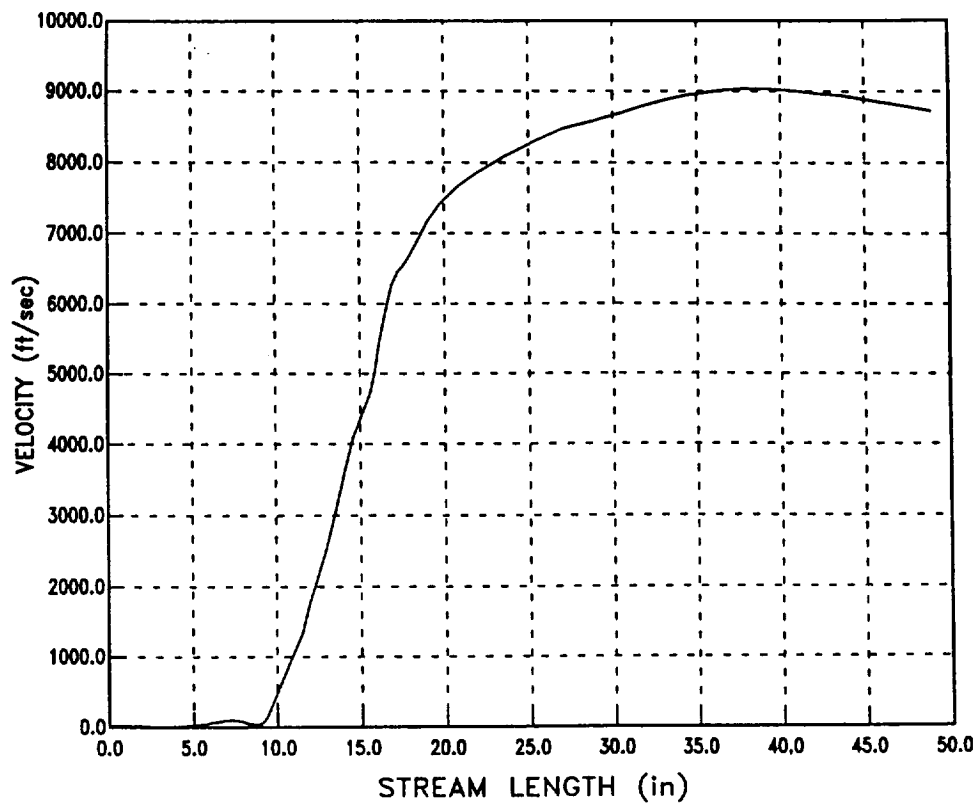


Figure 12. MNASA Nozzle Boundary Layer Edge Velocity

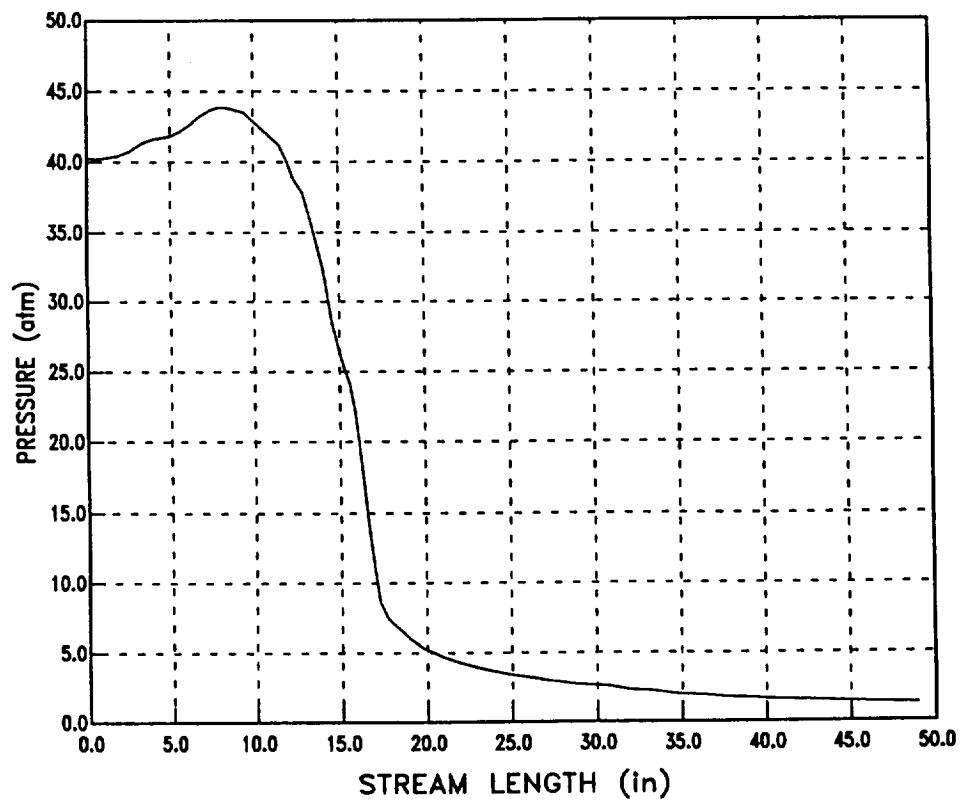


Figure 13. MNASA Nozzle Boundary Layer Edge Pressure

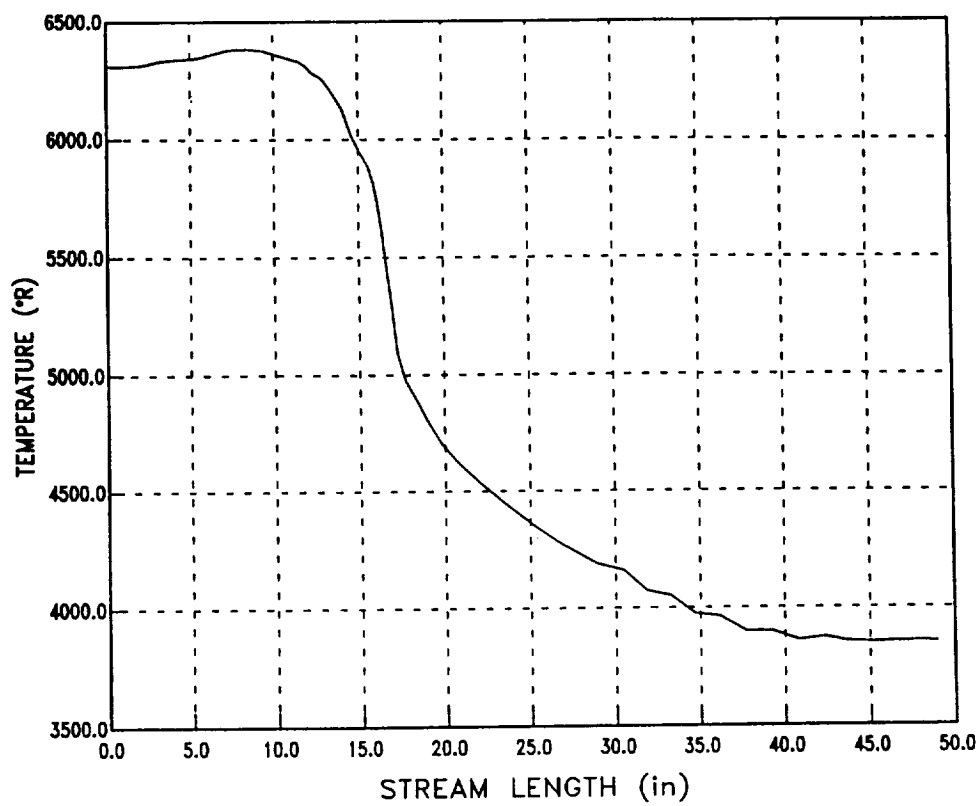


Figure 14. MNASA Nozzle Boundary Layer Edge Temperature

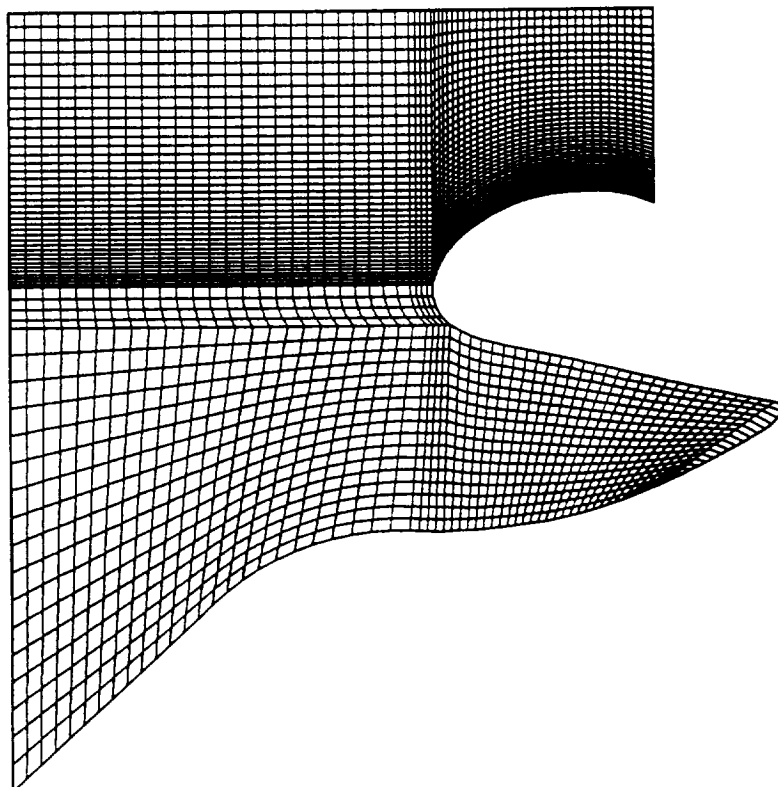


Figure 15. MNASA Nozzle Cutoff Analysis Grid

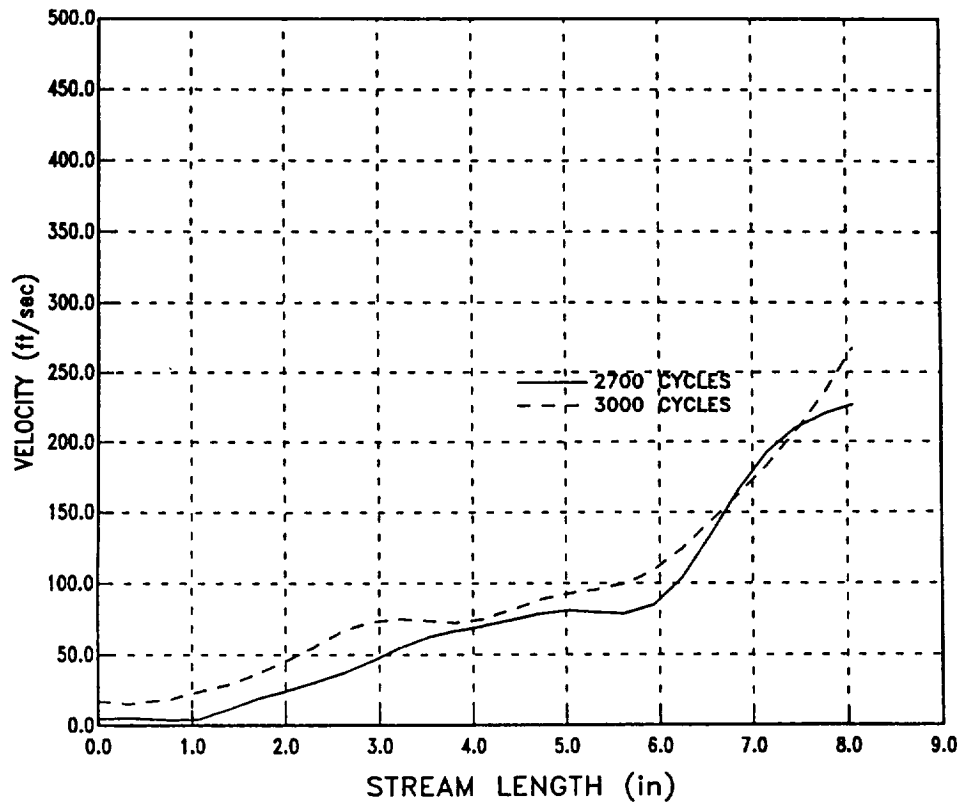


Figure 16. Boundary Layer Edge Velocities for the Submerged Region

Results from two grids were combined in defining the heating conditions throughout the nozzle. As stated above, the MEIT module was used to calculate the convective heating conditions. Results from these calculations are presented in Figure 17. This figure presents the convective transfer coefficient as a function of streamlength. It appears in this figure that the results from the cutoff grid are shifted slightly to the left. This is due to a slight difference in the streamlength which is calculated for the two grids. Figure 18 presents results as a function of axial position in the nozzle. The zero axial position is taken as the nozzle throat. The results are presented beginning at the nose of the nozzle (i.e., the point located furthest into the motor). The shift is no longer evident in this figure. Results aft of the throat agree precisely for the two grids. However, the cutoff grid calculates slightly lower heating rates in the throat region. Also, from Figure 17, the cutoff grid yielded higher heating rates in the submerged region of the nozzle, (i.e., streamlengths less than 9 inches).

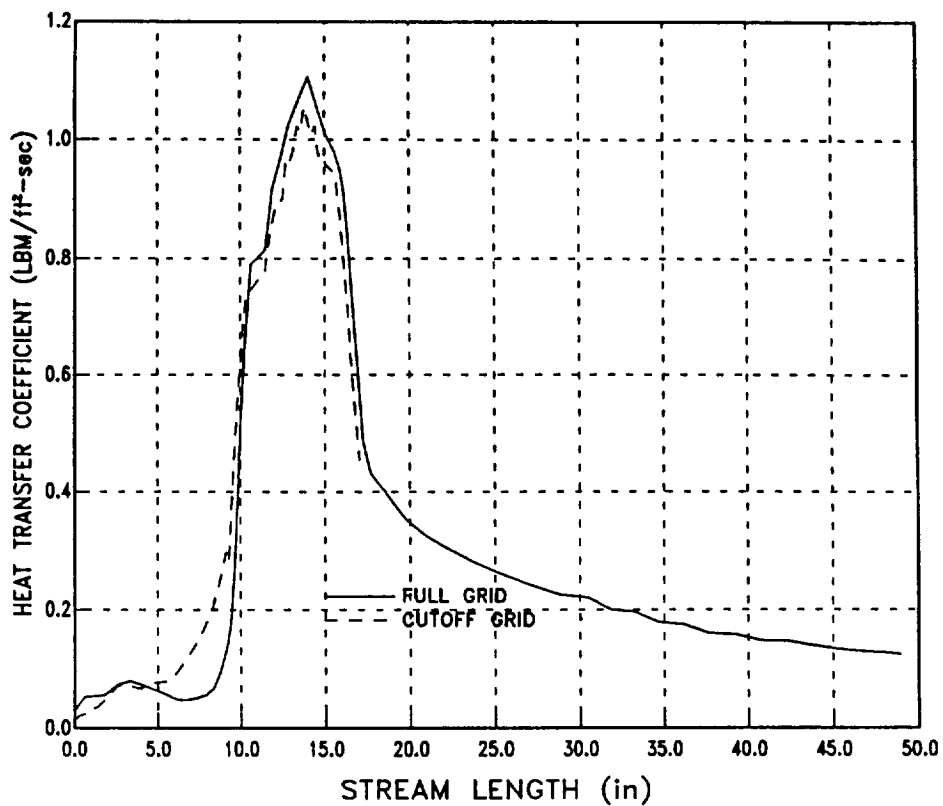


Figure 17. MNASA Nozzle Convective Heating Conditions

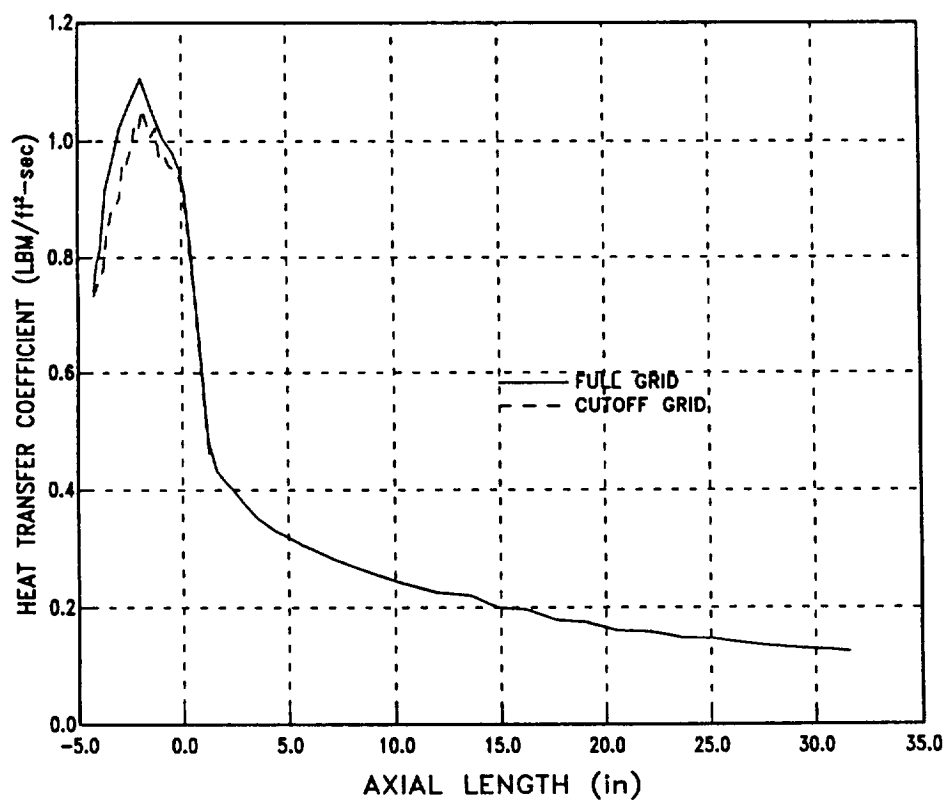


Figure 18. MNASA Nozzle Convective Heating Conditions as a Function of Axial Position

The sensitivity of the convective heating conditions, in the submerged region of the nozzle, to the fluctuating flow were also investigated. Results for this comparison are shown in Figure 19. This figure shows the convective transfer rate as a function of cycle. These results are taken from the calculation with the cutoff grid. The difference in the calculated rates is very small. Therefore it was decided to use the results from the 3000 cycle solution as the steady state solution. A summary of the nozzle heating conditions is contained in Table 4. This table presents the radiant heat flux, Q_{rad} , the radiation view factor, F , the recovery enthalpy, H_r , the convective transfer coefficient h/C_p , and the edge pressure, P_e , as a function of nozzle station. The location of each of these stations is shown in Figure 20. Nozzle erosion measurements have been performed at each of these stations. Erosion calculations (see Section 4) were also performed at these same positions. The radiant heat flux and the radiation view factors given in the table were determined using empirical techniques available in the NAT code. It should be mentioned that this table also includes interface heating effects which are described in the upcoming section.

The particle radiation is calculated with NAT assuming a parallel plate model. This model applies to aluminized propellants and assumes that the particle-laden stream of combustion products is optically thick and exchanges radiant energy with the surface as if the stream and wall were parallel plates. In this way, multiple reflections between wall and stream are considered. In addition, both the stream and wall were assumed to behave as gray bodies which emit and reflect radiant energy diffusely. Based on the above assumptions, the net radiant heat flux is given as:

$$\dot{q}_{net\ rad} = \epsilon_{eff}\sigma(T_s^4 - T_w^4) \quad (1)$$

where,

$$\begin{aligned} \epsilon_{eff} &= \text{effective emissivity} = \frac{1}{1/\epsilon_w + 1/\epsilon_s - 1} \\ \epsilon_s &= \text{particle-laden stream emissivity} = 1 - \exp\left(-C \frac{n}{16} \rho D\right) \\ \epsilon_w &= \text{wall emissivity} \\ \sigma &= \text{Stefan-Boltzmann constant} \\ T_s &= \text{freestream (edge) temperature} \\ T_w &= \text{wall temperature} \\ C &= \text{empirical constant} = 0.808 \\ n &= \text{percentage of aluminum loading} \\ \rho &= \text{local density of propellant combustion species (lb/ft}^3\text{)} \\ D &= \text{local beam length, usually taken as the diameter (inch)} \end{aligned}$$

Table 3 presents quantities Q_{RAD} and F which are input into the CMA thermal analysis code. These quantities are given by:

$$Q_{\text{RAD}} = \sigma \frac{\epsilon_{\text{eff}}}{\epsilon_w} T_s^4$$

$$F = \frac{\epsilon_{\text{eff}}}{\epsilon_w}$$

The convective transfer coefficients presented in the figures and table were determined based on the average chamber pressure for the 48-5 firing. Convective transfer rates for a given point in time, t , were determined with the following expression:

$$\frac{(h/Cp)_t}{(h/Cp)_{\text{avg}}} = \left(\frac{P_t}{P_{\text{avg}}} \right)^{0.8} \quad (2)$$

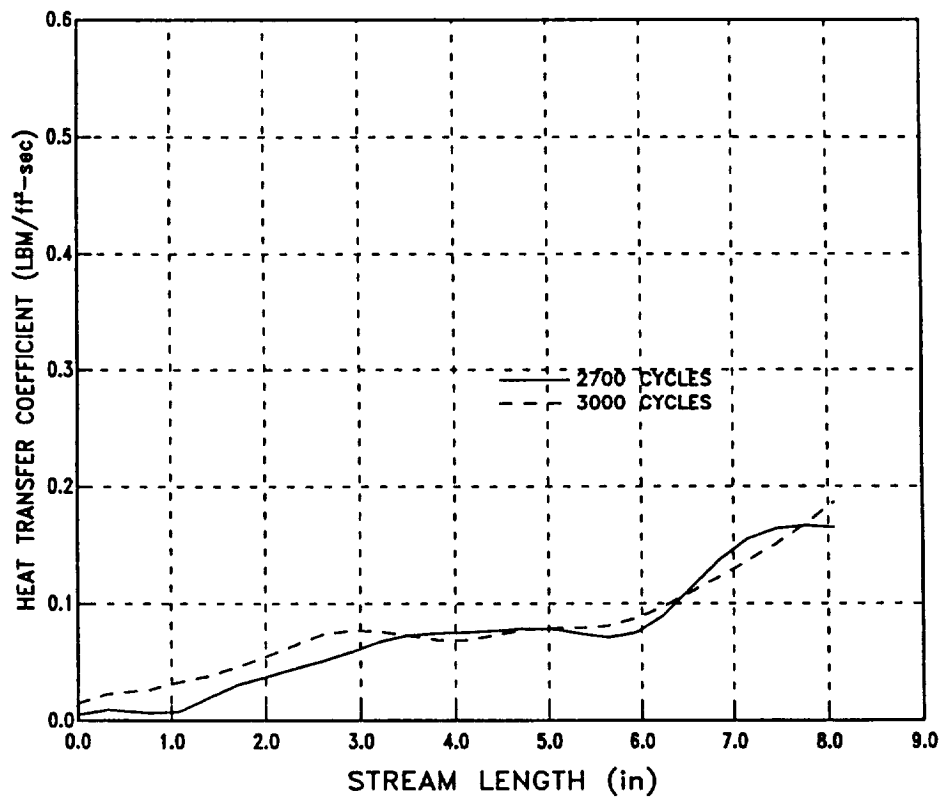


Figure 19. Submerged Region Convective Heating Conditions, Cutoff Grid

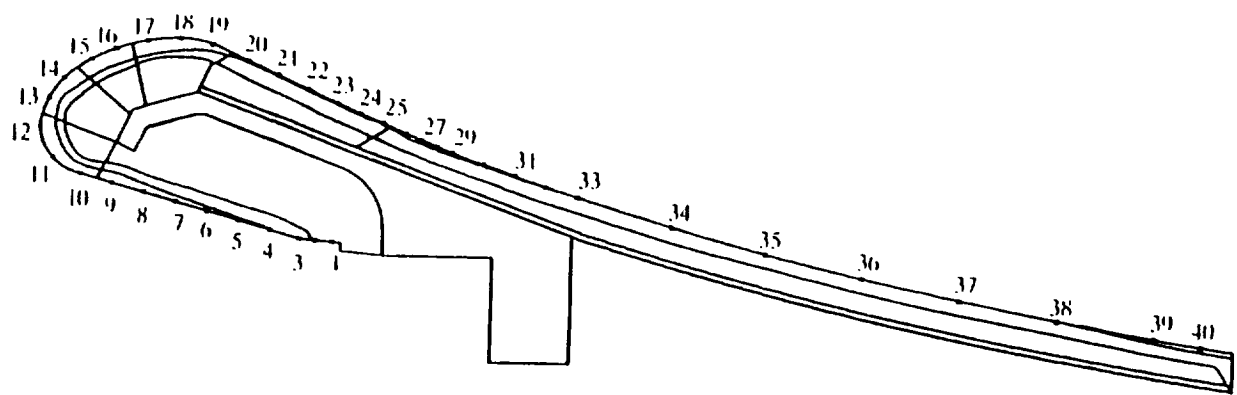


Figure 20. MNASA Nozzle Thermal Analysis Locations

Table 4: MNASA Nozzle Heating Conditions

Station	Q_{RAD} (BTU/ft ² -sec)	F	H_R (BTU/lbm)	h/C_p (lbm/ft ² -sec)	Pe(atm)
4	798.92	1.000	1160.00	0.041	44.900
5	798.92	1.000	1160.00	0.065	45.000
6	797.57	1.000	1160.00	0.069	44.700
7	796.27	1.000	1160.00	0.078	44.600
8	794.08	1.000	1150.00	0.087	44.400
9	800.31	1.000	1160.00	0.136	45.000
10	803.52	1.000	1170.00	0.186	45.300
11	806.68	1.000	1180.00	0.299	45.700
12	795.13	1.000	1180.00	0.436	45.700
13	730.62	0.960	1140.00	0.707	40.900
14	677.90	0.935	1120.00	0.883	37.500
15	657.60	0.920	1120.00	0.903	36.600
16	555.44	0.870	1110.00	1.050	29.700
17	468.98	0.835	1065.60	0.975	26.280
18	433.77	0.831	1070.00	0.936	19.800
19	293.71	0.754	1020.00	0.695	12.060
20	190.12	0.657	878.80	0.416	7.281
21	157.57	0.603	886.76	0.381	6.208
22	135.90	0.563	882.14	0.353	5.507
23	116.89	0.521	878.96	0.328	4.923
24	101.98	0.486	874.54	0.309	4.458
25	93.80	0.466	872.51	0.297	4.191
26	84.79	0.444	870.51	0.500	3.890
27	84.79	0.444	870.51	0.460	3.890
28	72.07	0.412	865.24	0.417	3.439
29	72.07	0.412	865.24	0.409	3.439
30	72.07	0.412	865.24	0.372	3.439
31	61.71	0.384	860.50	0.343	3.056
32	53.29	0.366	845.45	0.319	2.732
33	53.29	0.366	845.45	0.301	2.732
34	43.25	0.332	841.47	0.266	2.297
35	36.05	0.310	839.64	0.228	1.965
36	30.56	0.290	836.46	0.199	1.711
37	27.42	0.275	830.37	0.180	1.550
38	25.98	0.265	825.20	0.167	1.471
39	24.65	0.253	810.23	0.151	1.370
40	24.38	0.250	804.47	0.145	1.347

asrm

3.1.1 Material Interface Heating

It is commonly known that relatively small surface discontinuities can modify flowfields and augment convective transfer rates. A surface discontinuity is known to occur in the nozzle exit cone at the juncture of the standard and low density carbon phenolic materials. This surface discontinuity is the result of differential ablation rates for the two materials. The low density material ablates at a faster rate than the standard density material and thus a rearward facing step is formed. This step results in separated flow and boundary layer reattachment just aft of the material interface. Initial attempts were made to model this flow with the KIVA module of NAT in order to determine augmented heating rates. These calculations used the post test nozzle shape, i.e., eroded surface contour, but never yielded satisfactory results. Therefore, it was decided to address this issue using simplified procedures.

A literature search was performed and yielded a number of applicable references, see References 3 through 6. After reviewing these documents it was decided to simply calculate the heating conditions in this region by assuming that the boundary layer reattached just downstream of the material interface. This calculation was performed by using the flow results for the uneroded nozzle contour (described in Section 3.1) and assigning the boundary layer starting point as the material interface location. Results from this calculation are shown in Figure 21. This figure compares the convective transfer coefficients for the unperturbed and augmented heating conditions. The streamlength in this case is measured from the material interface location. The figure presents results beginning at this location and continuing to the exit plane of the nozzle. Starting the boundary layer at the interface position drastically increases the convective transfer rates, (approximately 75% nearest the interface). However, this augmentation rapidly falls off and there is only a slight augmentation effect at the exit plane location. How these results are used in subsequent thermochemical erosion calculations will be further described in Section 4.

3.1.2 Particle Flow Calculations

Two phase flow calculations were performed for the MNASA motor with the KIVA module of NAT. These calculations assumed that all of the aluminum in the propellant reacted to form liquid Al_2O_3 . Several initial calculations were performed for the nozzle considering 8 and 10 μm diameter particles. These calculations were found to be very time consuming and additionally no particle impacts were calculated to occur with the nozzle surface. Based on these initial experiences a less refined grid was developed to decrease computation time. This grid is shown in Figure 22. To perform these computations particles are modeled in groups called parcels. These parcels are continuously injected into the flow as indicated in the figure. Prior to injecting the particles, a steady state 2-D gas flow solution was obtained. First obtaining this steady state gas flow solution is not explicitly required for the particle flow calculation, but was simply the method selected for this study. This method was selected because the KIVA

module is a time accurate Navier Stokes solver. Because of this, it was desired not to include the transient effects in going from the initial flow conditions to the converged gas flow conditions.

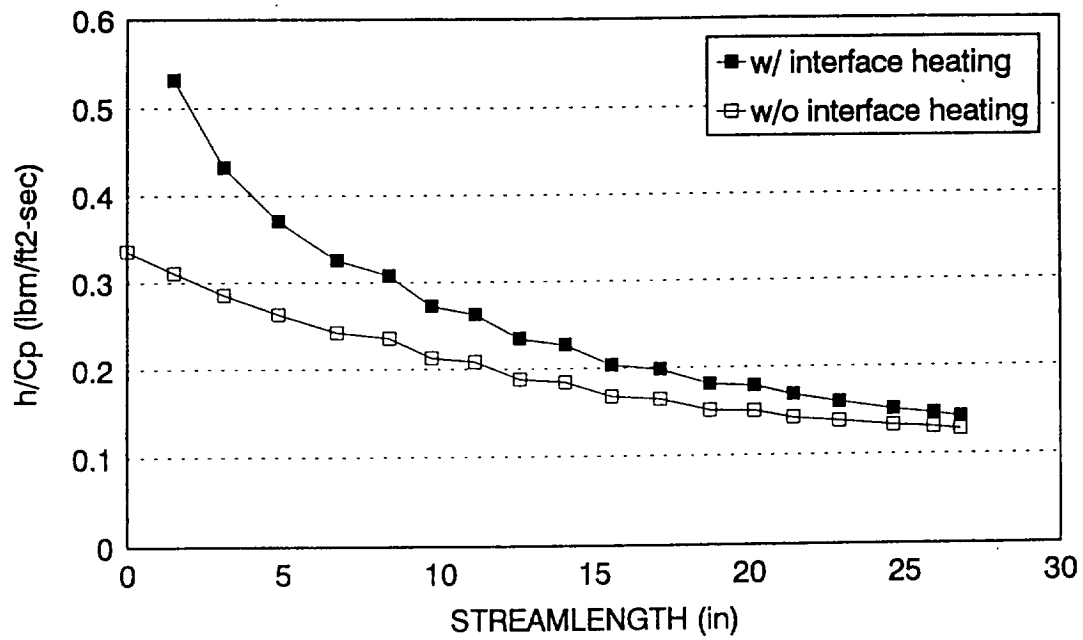


Figure 21. Augmented Heating Rates at the Exit Cone Material Interface

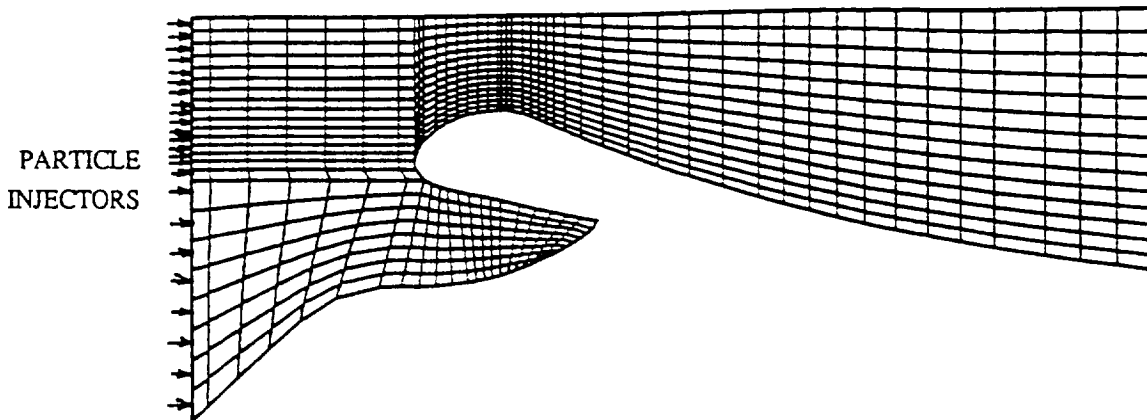


Figure 22. MNASA Particle Flow Grid

Based on data of Salita (Reference 7) a calculation was performed for a $120\text{ }\mu\text{m}$ particle diameter. Salita performed experiments which showed that in a motor chamber a significant amount of particles with diameters greater than $100\text{ }\mu\text{m}$ are formed. Particle size data from Salita is shown in Figure 23. This figure shows the mass fraction of particles smaller than a given size. Both the data and Salita's curve fit are presented. Notice that about 65% of the particle mass consists of particles with diameters less than $10\text{ }\mu\text{m}$. Nearly all of the remaining particle mass, i.e., 35%, is contained in particles with diameters greater than $100\text{ }\mu\text{m}$. This data is taken from an experiment with a 500 psi chamber pressure. The significant quantity of large particle diameters may be inconsistent with particle sizes which are traditionally considered in solid rocket motor nozzle analysis. However, this data is consistent with other studies (References 8) which show that large particles can exist in the motor chamber but will breakup in the exit cone and exit the nozzle much smaller in size.

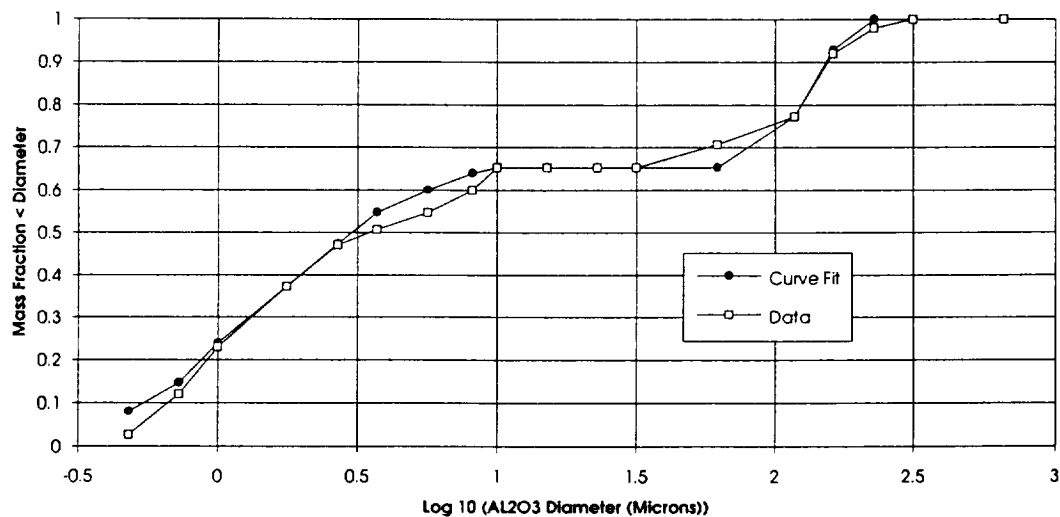


Figure 23. Particle Size Distributions from Reference 7

Results from the 120 μm particle flow computation are presented in Figures 24 through 28. The total particulate mass flow rate for the motor is determined from one dimensional isentropic flow solutions. The total number of parcels used for the computation is then selected. After determining the mass of each particle it is then possible to determine the number of particles per parcel and the required injection rate. For this calculation each parcel represents 18,729 particles and parcels are injected into the flow at a rate of 748,000 parcels/second (this rate is for a 0.5 degree sector of the motor). The injection was performed in such a fashion that a uniform particle mass flux was entering the flow domain. Because of this, a higher parcel injection rate is required at the larger radial positions (because of the larger area in these regions). These figures present parcel velocity plots as a function of time. Results are presented for only selected parcel numbers; 1-100, 400-500, 900-1000, 1900-2000, and 2900-3000. Following are comments relative to these results:

1. In the entrance region of the nozzle, particle velocities are greater at locations away from the nozzle centerline.
2. Particle impacts are calculated to occur for both the aft closure and submerged portions of the nozzle.
3. Particles are accelerated radially inward in the converging portion of the nozzle and tend to remain very tightly grouped near the nozzle centerline through the exit cone.

Figure 29 presents parcel velocities plotted for every fifth parcel. This plot helps to show the trajectory of each parcel since they tend to follow one after another. Also identified in this figure is the region within the nozzle for which particle impacts are calculated. Since parcels are injected at discrete locations, impacts also occur at discrete locations. However, in reality these impacts cover an area just as the particle inflow, although modeled with discrete injection points, covers an area. The impact conditions at location 1 (identified in the figure) are a velocity of 140 ft/sec and an impact angle of 46 degrees. The conditions at location 2 are 154 ft/sec and an impact angle of 71 degrees.

The mass flux of the particles was determined for the two locations by summing the total number of parcel impacts over time and knowing the mass of each parcel. Additionally, the area of impact was taken as shown in the figure. With this approach, the total particle mass fluxes were found to be 12.4 (lbm/ft²-sec) and 15.7 (lbm/ft²-sec) at locations 1 and 2, respectively. Of course, this assumes that all particles are 120 μm as used in this analysis. The data from Salita⁷ suggests that the 120 μm diameter particles is probably representative of 35% of the particle mass. Based on this, it was assumed that only 35% of the mass flux actually was impacting the nozzle (previous calculations for 10 μm particles had shown no impacts). With this, the mass fluxes become 4.34 (lbm/ft²-sec) and 5.495 (lbm/ft²-sec) for the two locations. This method of applying particle size effects was used in lieu of attempting flow computations with particle size distributions.

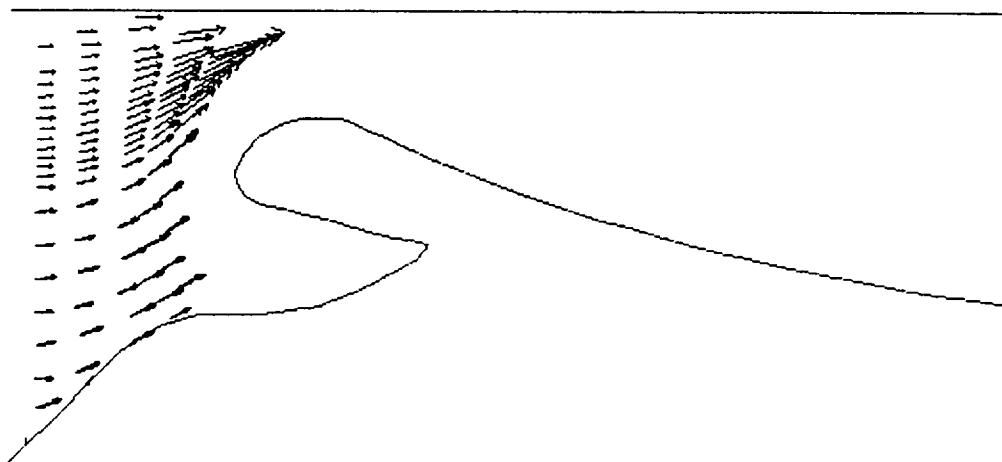


Figure 24. MNASA 120 μm Particle Flow Results, Time=0.0064 Seconds

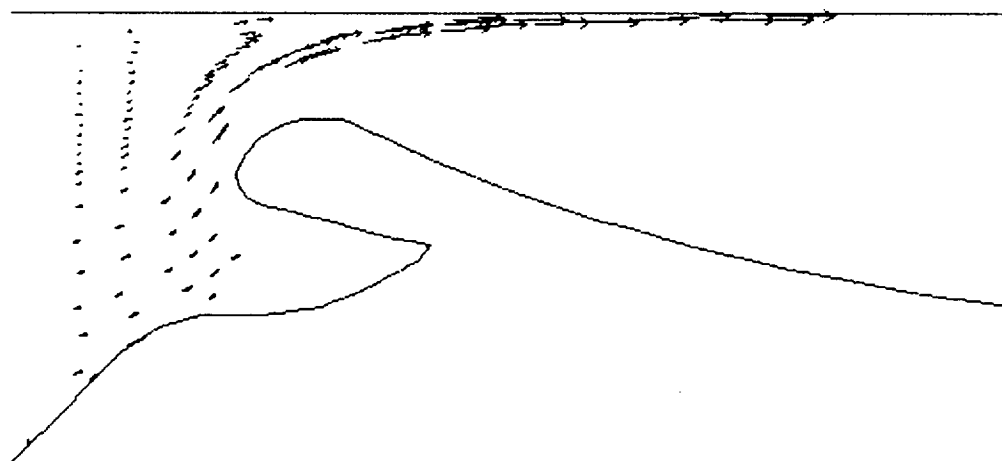


Figure 25. MNASA 120 μm Particle Flow Results, Time=0.00765 Seconds

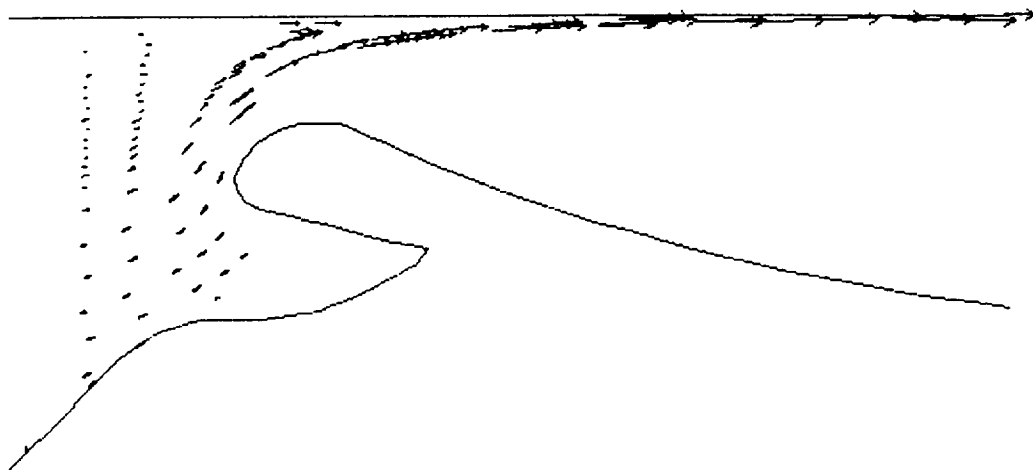


Figure 26. MNASA 120 μm Particle Flow Results, Time=0.0079 Seconds

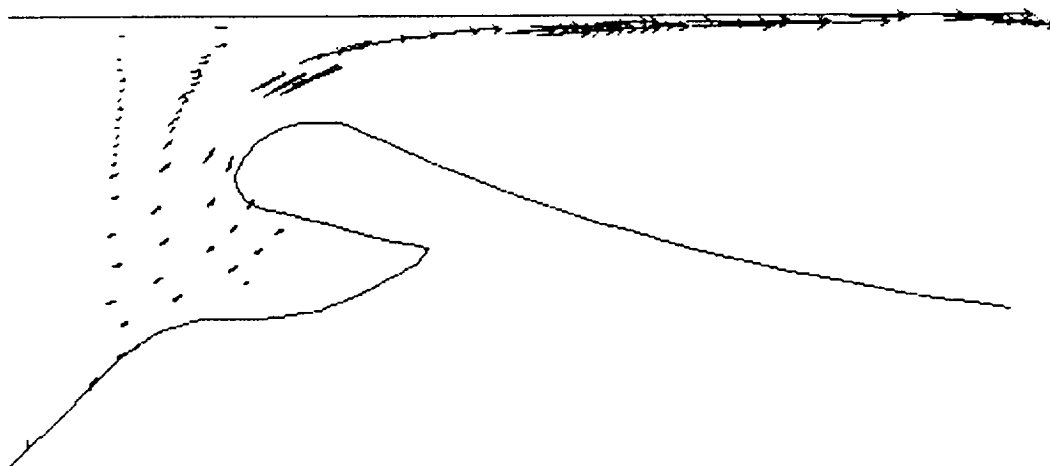


Figure 27. MNASA 120 μm Particle Flow Results, Time=0.00885 Seconds

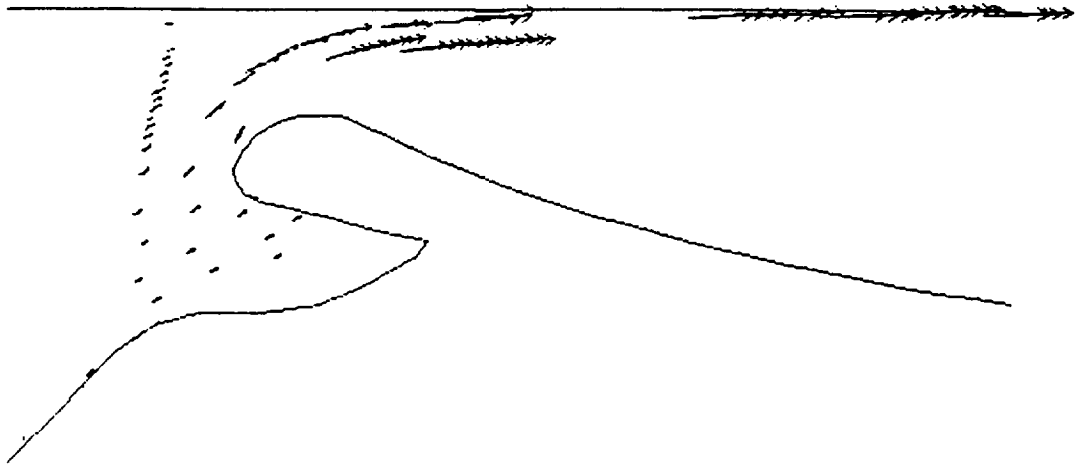


Figure 28. MNASA 120 μm Particle Flow Results, Time=0.0101 Seconds

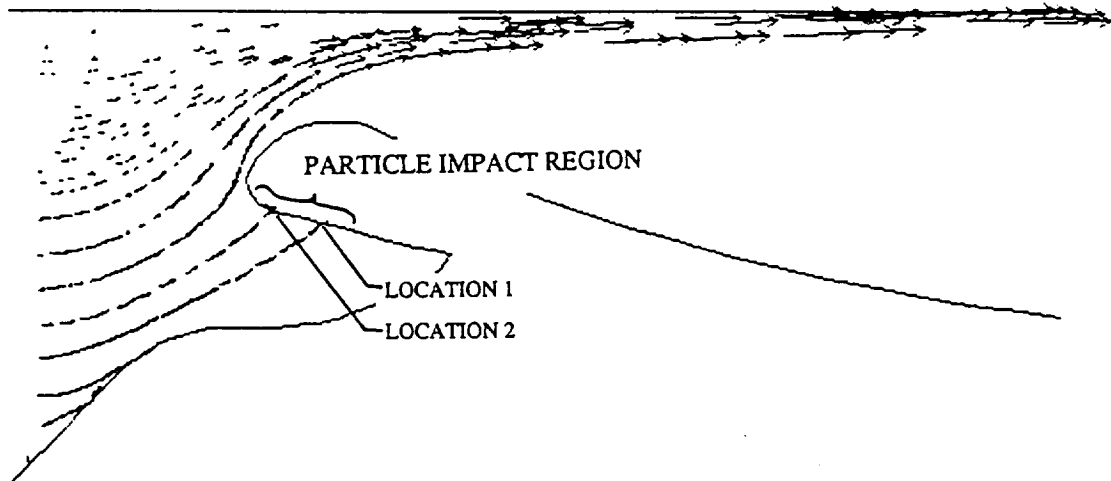


Figure 29. 120 μm MNASA Particle Flow Results, Time=0.0103 Seconds

The next task was the determination of impact angle and velocity for each of the nozzle measurement positions for which particle impact occurred. The curves in Figure 30 were used to determine this information. This figure presents particle velocity, particle direction and body angle as a function of axial position in the nozzle. The body angle is the angle between the local nozzle surface tangent and the nozzle centerline. The body angle plot is simply determined from the nozzle geometry. The velocity plot was constructed by using the velocities at the two impact locations and linearly extrapolating. The particle direction plot was constructed by using the two impacting trajectories and inferring the trajectories for the outer regions of the impacts. These trajectories were inferred based on both the impacting and non impacting particle trajectories. With this data, it was then possible to determine the particle impact conditions for each of the analysis positions. This information is summarized in Table 5 for measurement locations where particle impacts are calculated to occur. The impact information contained in Table 4 was used in subsequent material erosion calculations which are described in Section 4. It should be noted that the flexseal specimen used in these tests is located at axial positions between -0.7 inch and 3.55 inches. Obviously, this specimen is experiencing particle impact as well as convective and radiative heating.

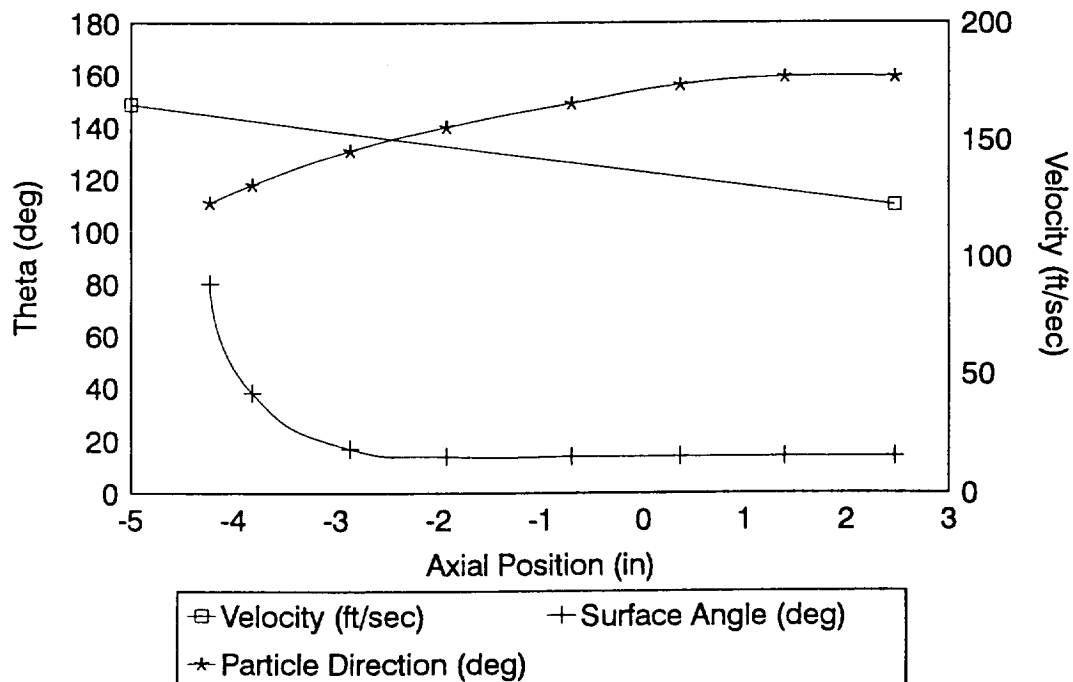


Figure 30. Particle Impact Conditions for the MNASA Nozzle

Table 5. MNASA Nozzle Particle Impact Conditions

Station	Axial Position (in.)	Radial Position (in)	Surface Angle (deg)	Particle Direction (deg)	Impact Angle (deg)	Velocity (ft/sec)	\dot{m} (lbm/ft ² - sec)
6	1.393	10.135	14	159	35	126	4.34
7	0.365	9.863	14	156	38	133	4.34
8	-0.701	9.590	14	149	47	139	4.34
9	-1.923	9.307	14	140	54	147	4.34
10	-2.863	9.044	17	131	66	152	5.495
11	-3.815	8.59	38	118	100	157	5.495
12	-4.232	7.694	80	111	149	161	5.495

3.2 ASRM NOZZLE FLOWFIELD AND HEATING RATE CALCULATIONS

Nozzle flowfield, heating rate, and surface thermochemistry calculations have been performed for the ASRM nozzle using the NAT computer code and the same procedures employed for the MNASA nozzle. This motor uses the same propellant as utilized in the MNASA motor and therefore the propellant gas formulation given in Table 2 was again used. Figures 31 and 32 present two different analysis grids used to calculate the flow within the ASRM nozzle. Figure 31 is the analysis grid for time zero, i.e., with the propellant grain in its initial configuration. This figure also identifies the propellant grain boundary. The inflow conditions were again applied at the left hand side of the analysis grid. Figure 32 presents the analysis grid used for the nozzle at the final point in time and will be referred to as the end of burn (EOB) grain. It should be pointed out that the motor actually attains this configuration at about 112 seconds into the burn. The aft motor section is burned out at this point but the forward section has propellant remaining and continues to burn. The gridding of these two configurations is similar to the MNASA motor in that grid refinement is greatest in regions where the largest gradients are expected. The average chamber pressure of 616 psi was used for both geometries.

Because of the differences in the motor grain geometries, the inflow velocities for the two configurations are drastically different. The initial grain configuration has an inflow velocity of about 1050 ft/sec whereas the EOB grain has an inflow velocity of only 290 ft/sec. It was expected that this difference in inflow conditions could potentially cause significant differences in the nozzle flowfields and heating conditions, especially in the submerged and the throat entrance regions of the nozzle.

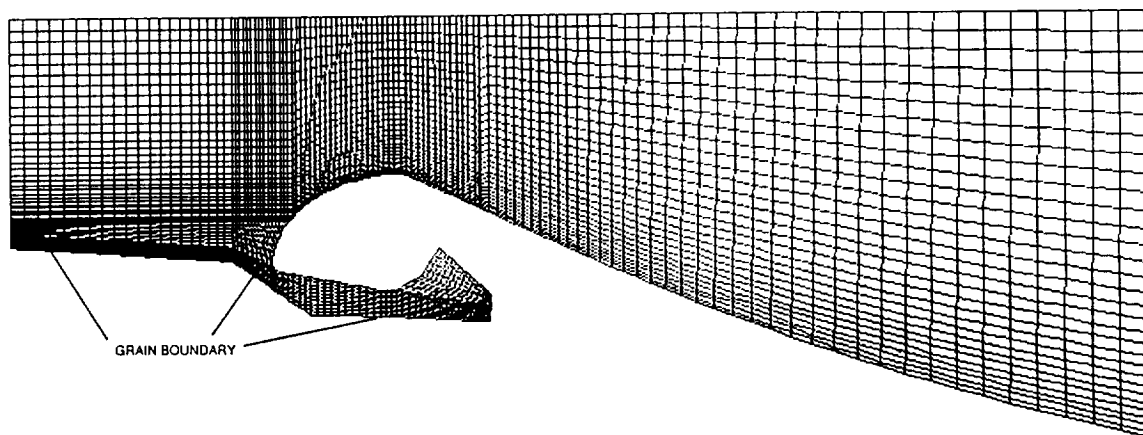


Figure 31. ASRM Nozzle Analysis Grid, Initial Grain Geometry

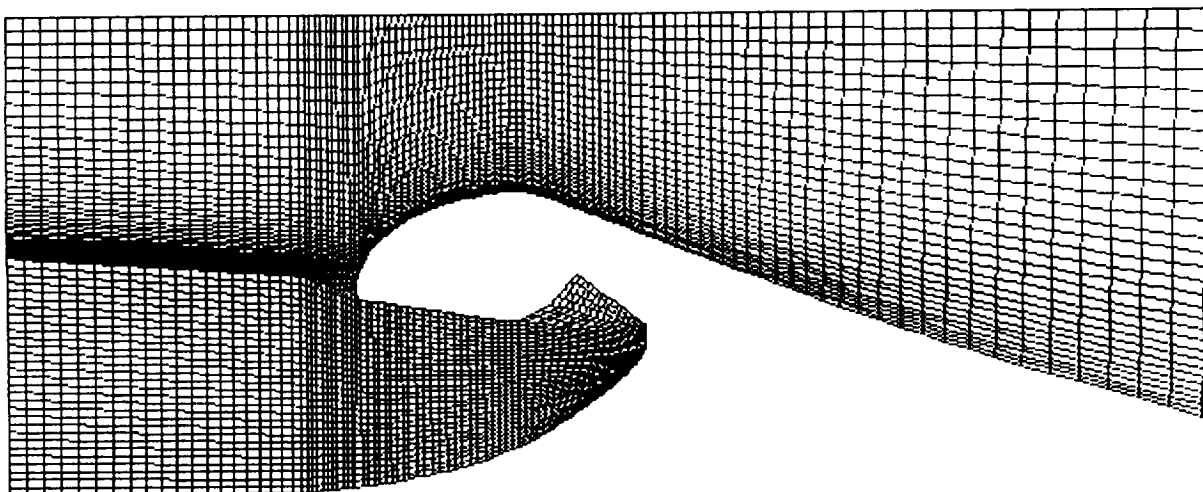


Figure 32. ASRM Nozzle Analysis Grid, EOB Grain Geometry

Flow results for the initial grain geometry are presented in Figures 33 through 36. These are the steady state flow results obtained after a 2800 cycle calculation. Figure 33 presents flow velocity vectors. Figures 34 through 36 present pressure, temperature, and Mach contours. The most significant feature of these results is the very large gradients which exist just downstream of the nozzle throat.

Flow results for the EOB grain geometry are presented in Figures 37 through 40. These results required 2000 cycles to reach steady state conditions. Besides the obvious differences in the entrance and submerged regions of the nozzle, there are only very small differences in the flow results compared to the initial grain geometry. A precise comparison is not easily made because of the slight differences in the value of the contour lines. However, the features and shape of the contours are very similar. This is most evident in the forward exit cone region. The slight differences in the maximum and minimum temperatures and pressures are most likely just a result of the degree of convergence in the solution.

Boundary layer solutions were performed for the nozzle using the same procedures described in Section 3.1. Figure 41 shows the location within the nozzle chosen as the boundary layer starting point. This location was selected based on the flow direction calculated for this area, i.e., this appeared to be the initial point where the flow followed the nozzle surface continuously until exiting the nozzle. The heating rates in the converging/diverging portions of the nozzle were found to be insensitive to this starting point.

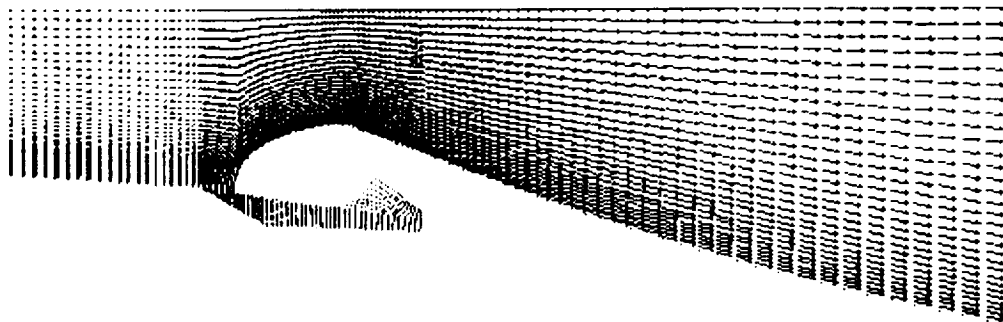


Figure 33. ASRM Nozzle Velocity Vectors, Initial Grain

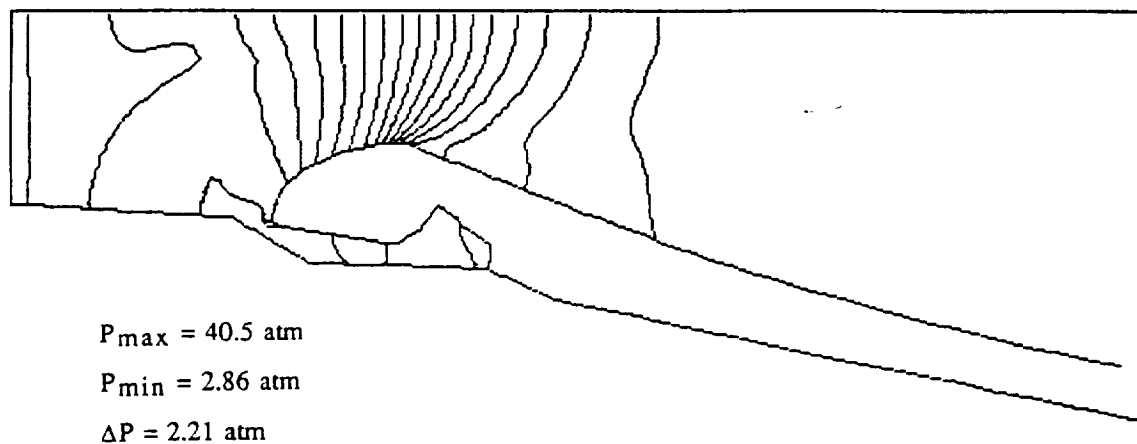


Figure 34. ASRM Nozzle Pressure Contours, Initial Grain

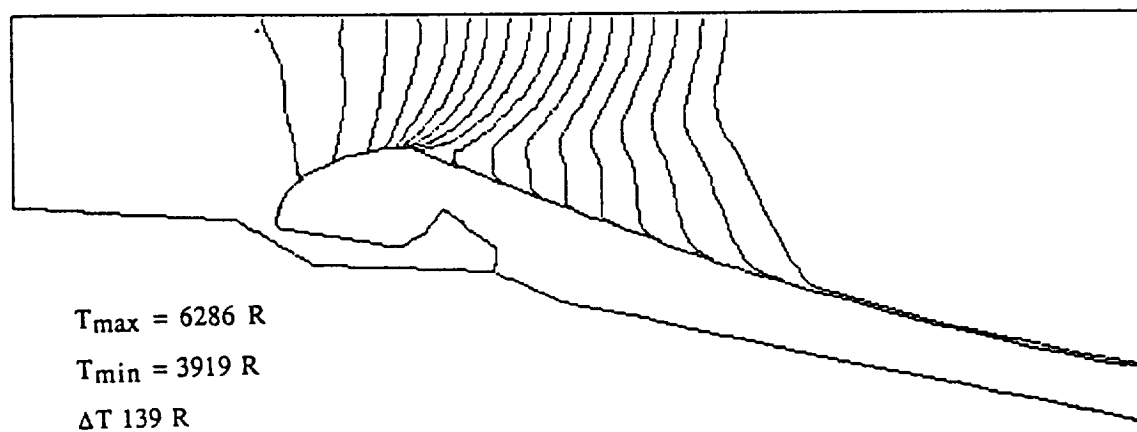


Figure 35. ASRM Nozzle Temperature Contours, Initial Grain

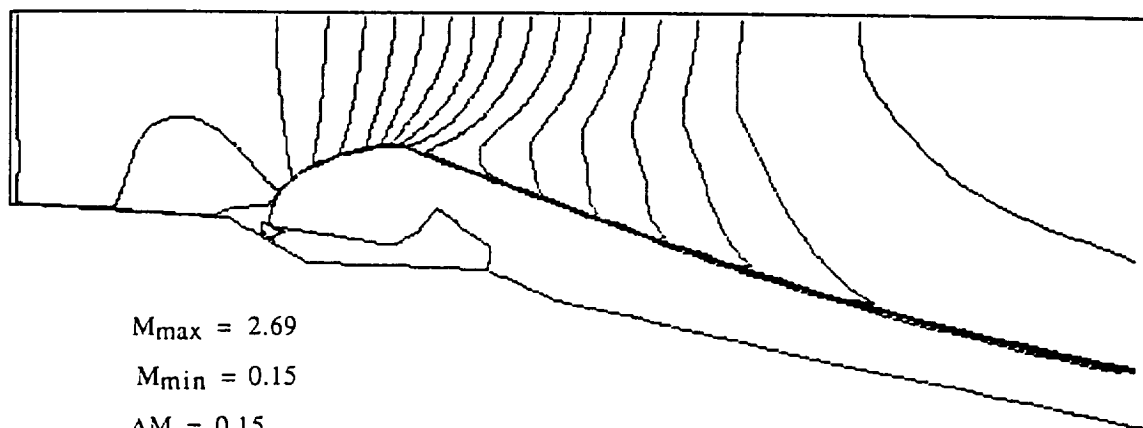


Figure 36. ASRM Nozzle Mach Contours, Initial Grain

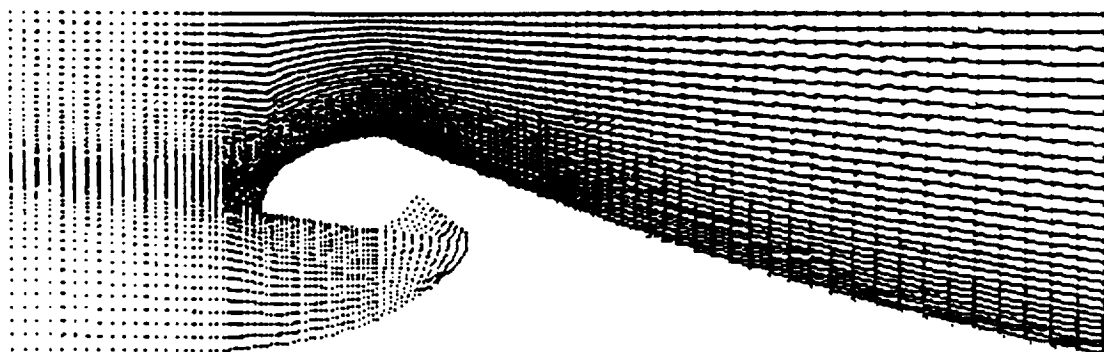


Figure 37. ASRM Nozzle Velocity Vectors, EOB Grain

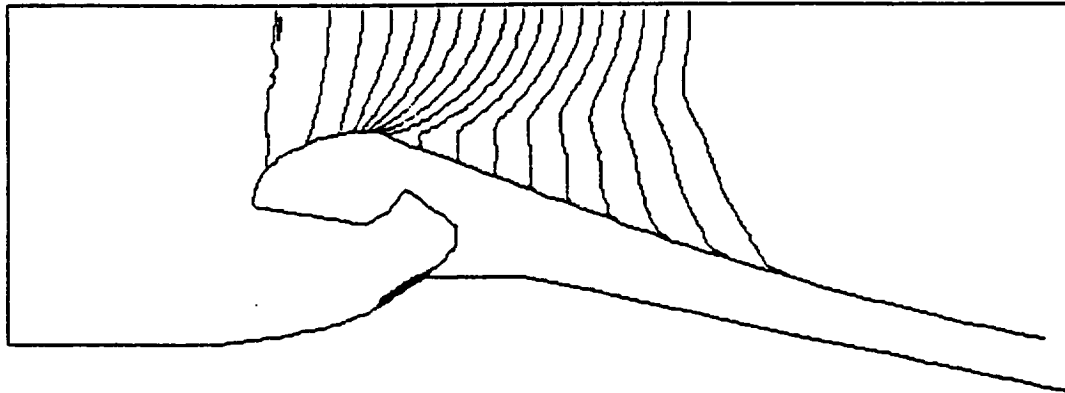


Figure 38. ASRM Nozzle Pressure Contours, EOB Grain

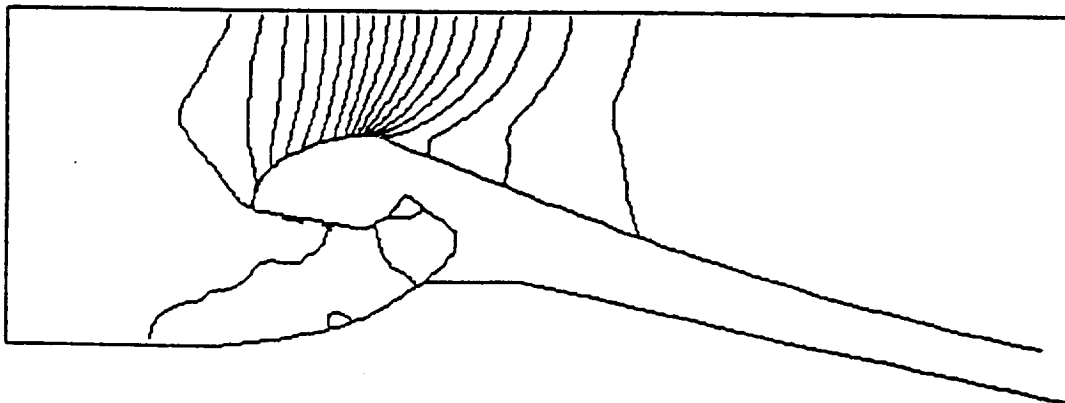
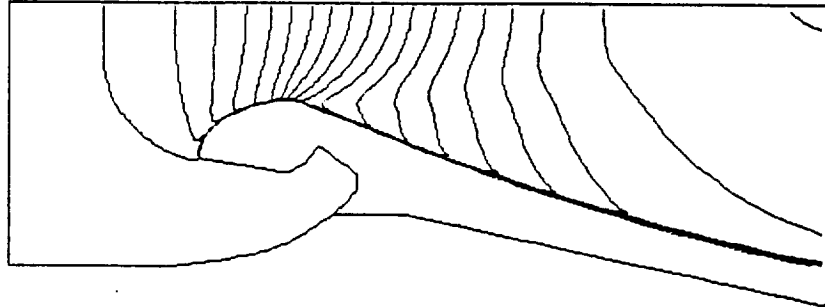


Figure 39. ASRM Nozzle Temperature Contours, EOB Grain



$$M_{\max} = 2.74$$

$$M_{\min} = 0.152$$

$$\Delta M = 0.152$$

Figure 40. ASRM Nozzle Mach Contours, EOB Grain

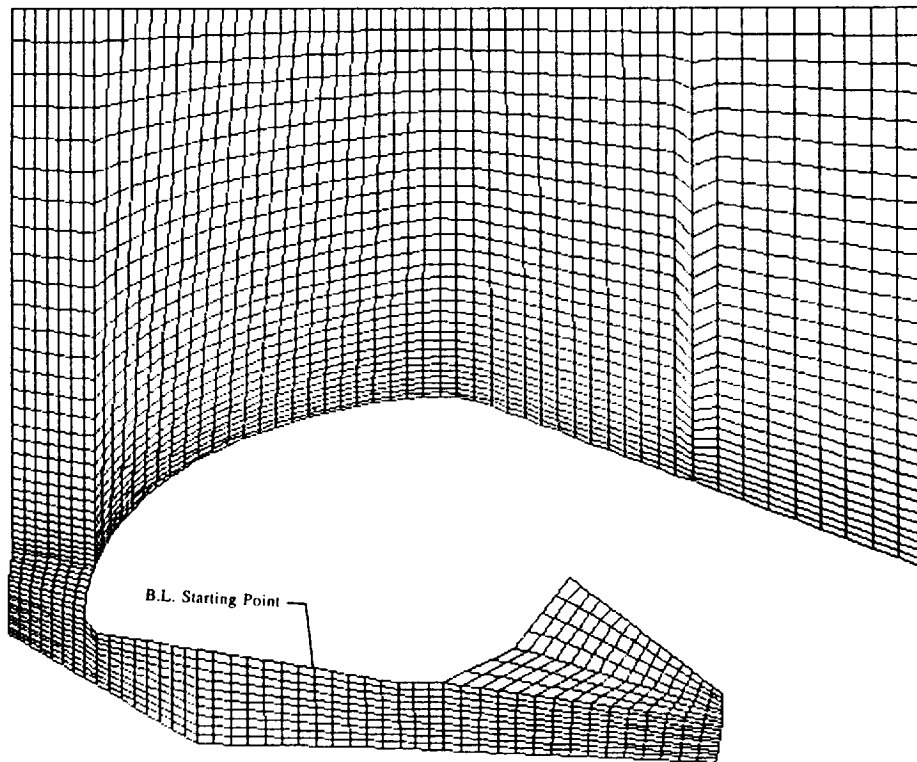


Figure 41. Boundary Layer Starting Point for ASRM Nozzle

The boundary layer edge conditions and heat transfer coefficients for the nozzle are presented in Figures 42 through 49. Results are presented in two groups. The first group, Figures 42 through 45, covers positions within the nozzle beginning at the nose of the nozzle and continuing downstream through the exit cone. The second group, Figures 46 through 49, begins at the nose and runs into the submerged region of the nozzle. These figures present velocity, pressure, temperature and convective heat transfer coefficient as a function of axial position within the nozzle. These axial positions are taken from the drawing for the nozzle. The zero point is located at the head end of the motor. The nose of the nozzle is located at an axial position of 421.8 inches. The nozzle throat is located at 446.6 inches. Following are comments relative to these results:

1. There is a sudden expansion of the flow just aft of the nozzle throat. This can be seen in Figures 42 through 44 but is most pronounced in Figure 45, the heat transfer coefficient. In this figure, the heat transfer coefficient reaches a maximum just upstream of the throat and then drops off very suddenly.
2. Temperatures and pressures in the submerged region are nearly constant.
3. Flow velocities in the submerged region of the nozzle are about 100-150 ft/sec in the aft regions (nearest the nose) but drop off to about 50 ft/sec in the forward region. The heat transfer coefficient follows the same trend. It has a value of about 0.1 (lbm/ft²-sec) and then drops off to about 0.025 (lbm/ft²-sec).

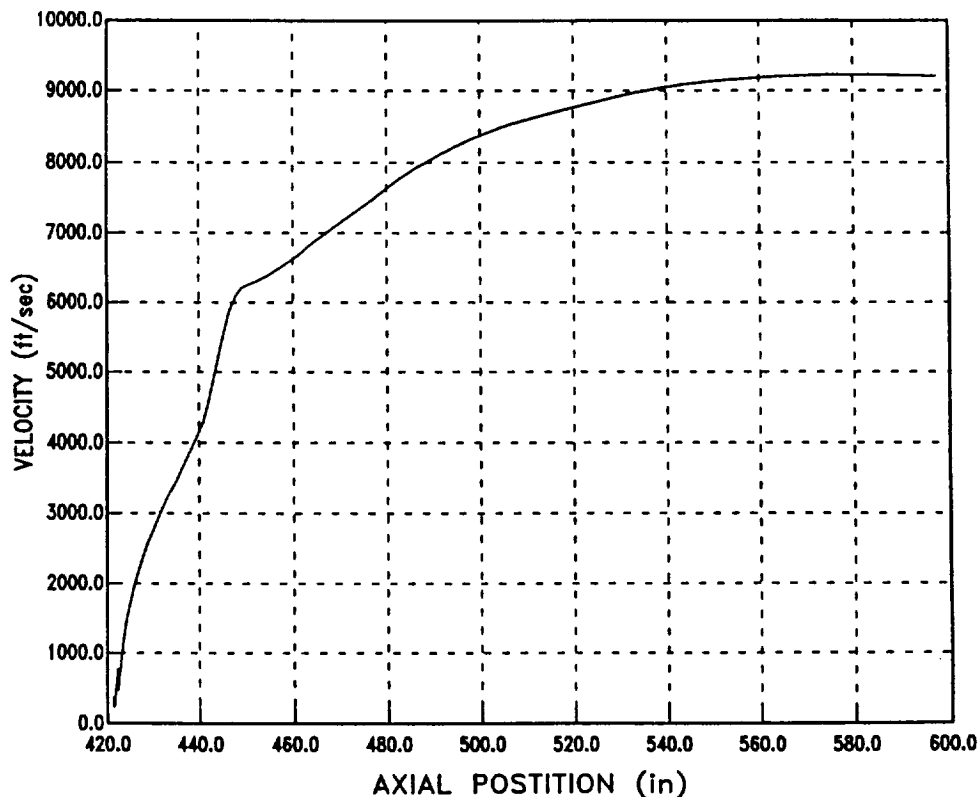


Figure 42. ASRM Nozzle Edge Velocity

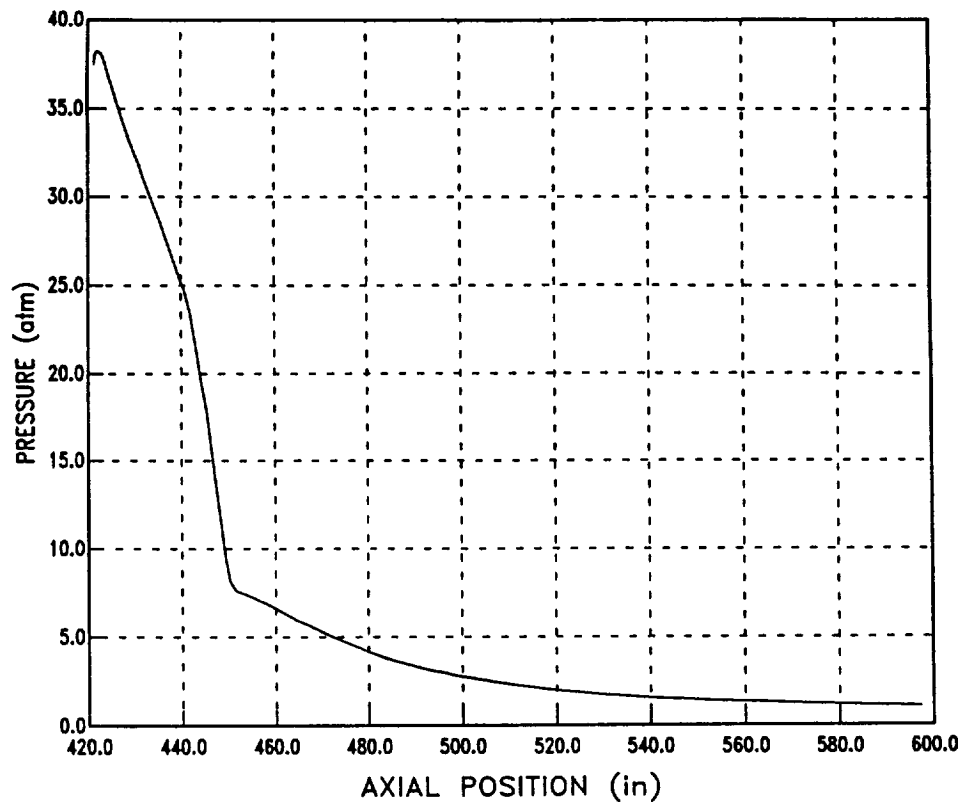


Figure 43. ASRM Nozzle Edge Pressure

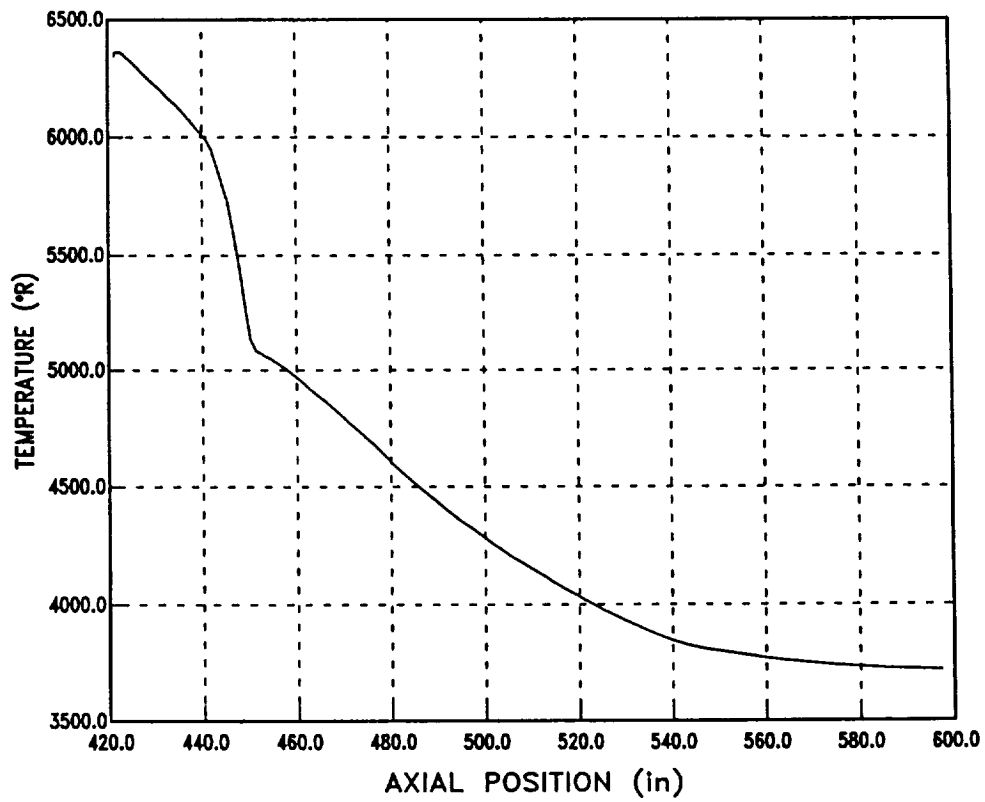


Figure 44. ASRM Nozzle Edge Temperature

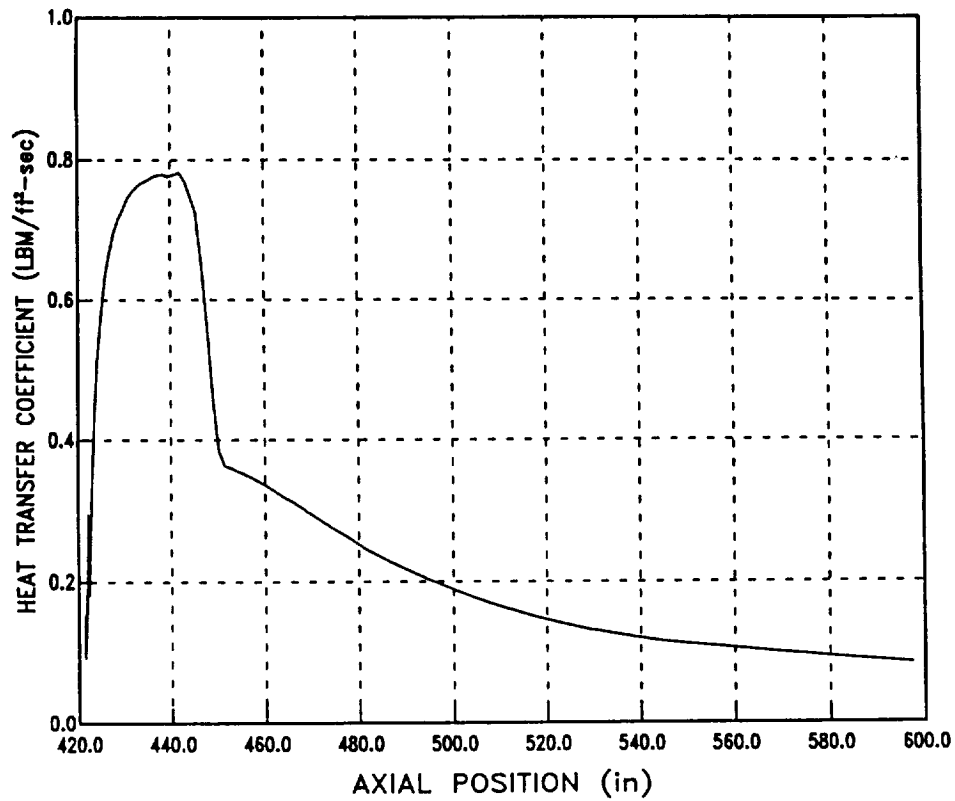


Figure 45. ASRM Nozzle Heat Transfer Coefficients

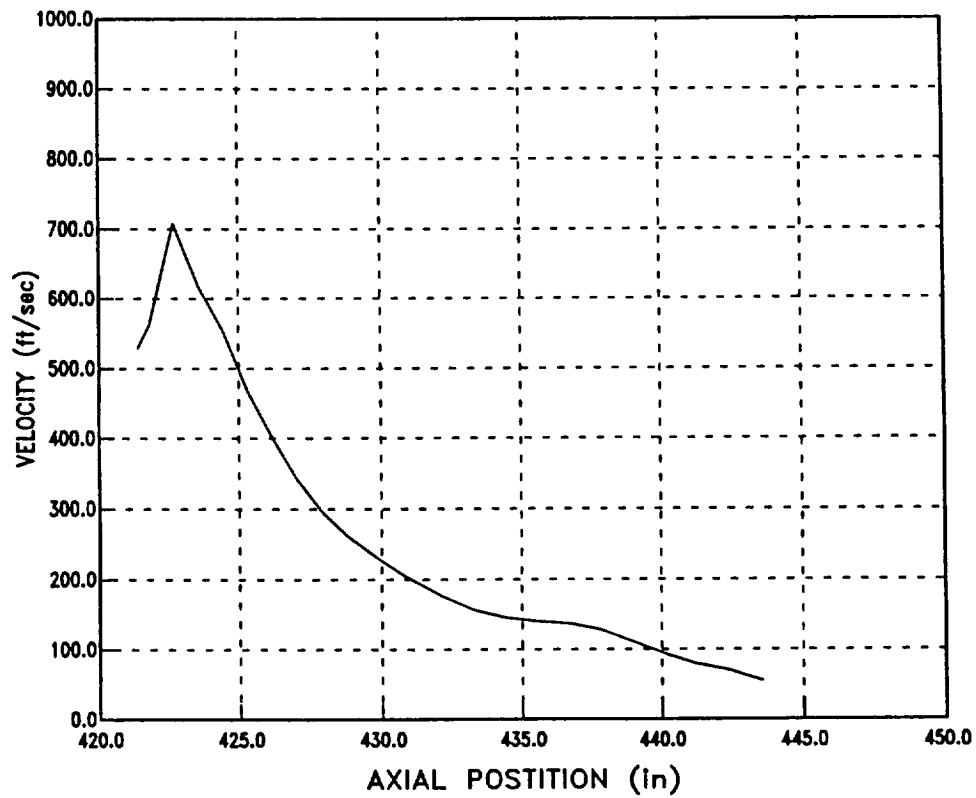


Figure 46. ASRM Nozzle Edge Velocity, Submerged Region

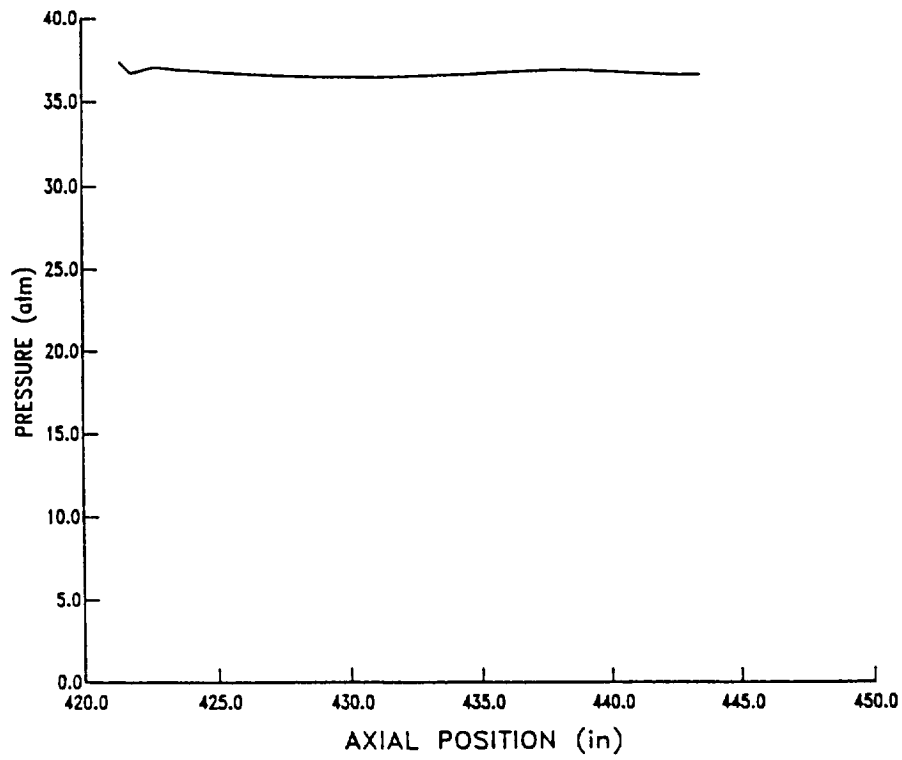


Figure 47. ASRM Nozzle Edge Pressure, Submerged Region

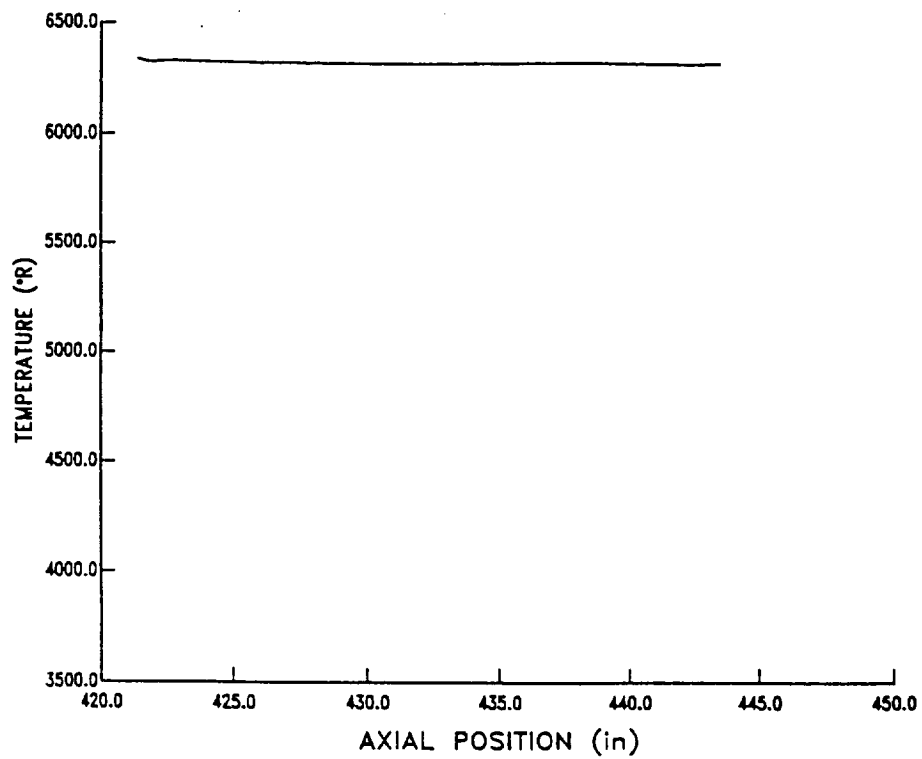


Figure 48. ASRM Nozzle Edge Temperature, Submerged Region

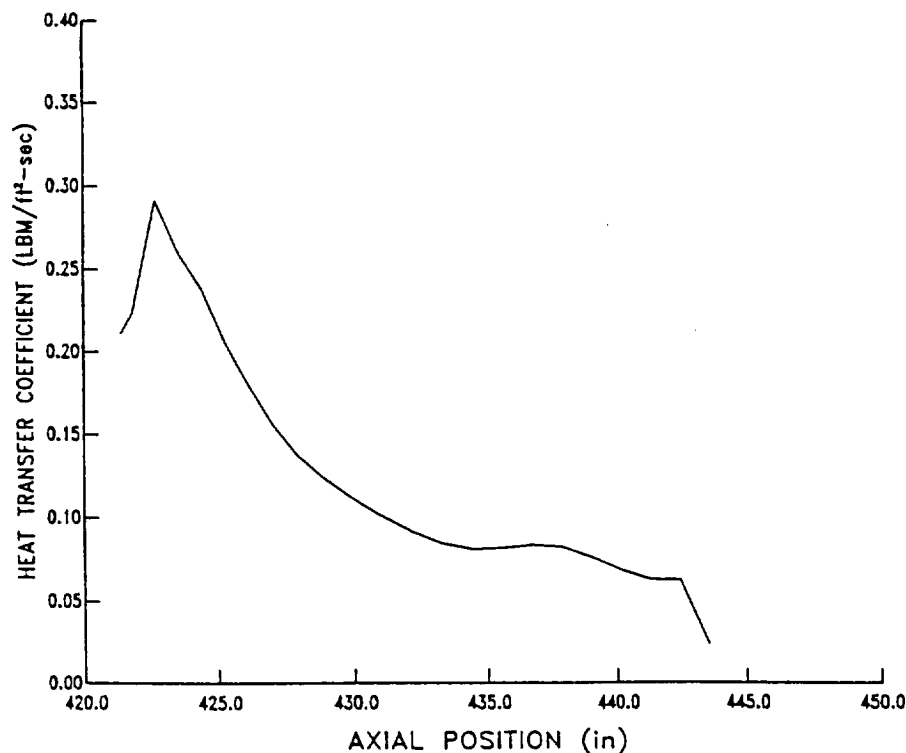


Figure 49. ASRM Nozzle Edge Heat Transfer Coefficients, Submerged Region

Results which have been presented thus far are for the initial grain configuration. As previously mentioned, the flow results for the EOB configuration were relatively similar. Just how similar can be seen in Figures 50 and 51. Figure 50 shows the heat transfer coefficients calculated for the nozzle downstream of the nose. This figure compares the results for the initial and end of burn grain geometries. The initial grain geometry appears to have slightly higher convective heating rates in the nozzle entrance region but otherwise the heating rates are nearly identical. Similar results are presented in Figure 51 for the submerged portion of the nozzle. Not too surprisingly, the heating conditions are somewhat different. The EOB configuration tends to experience lower heating conditions near the nose of the nozzle (i.e., axial positions around 425).

Several locations within the ASRM nozzle were selected for subsequent thermal and erosion calculations. These locations are identified in Figures 52 and 53. Figure 52 shows the analysis locations in the entrance region of the nozzle and Figure 53 identifies the positions in the exit cone region. Table 6 presents the heating conditions calculated for each of these analysis positions. All of the heating conditions presented are for the initial grain configuration. Only for the submerged region, station 1, were time effects included in the erosion calculations. This table also includes interface heating conditions (beginning at Station 11) which will be discussed in the following section.

One area of the nozzle receiving special attention was the flex seal. Tests conducted with the MNASA motor had shown the flex seal specimen to experience a significant amount of erosion. Therefore, accurately defining the heating conditions for the ASRM flex seal was of increased importance. Table 7 presents a summary of the results calculated for the flex seal region. Somewhat surprisingly, the conditions are expected not to change very much during the burn. Gas velocities adjacent to the flex seal range from about 30 ft/sec to slightly over 100 ft/sec. The convective heating rate on the

flex seal is about $0.06 \text{ lbm/ft}^2\text{-sec}$. This is only about 25% less than the conditions calculated for the MNASA motor.

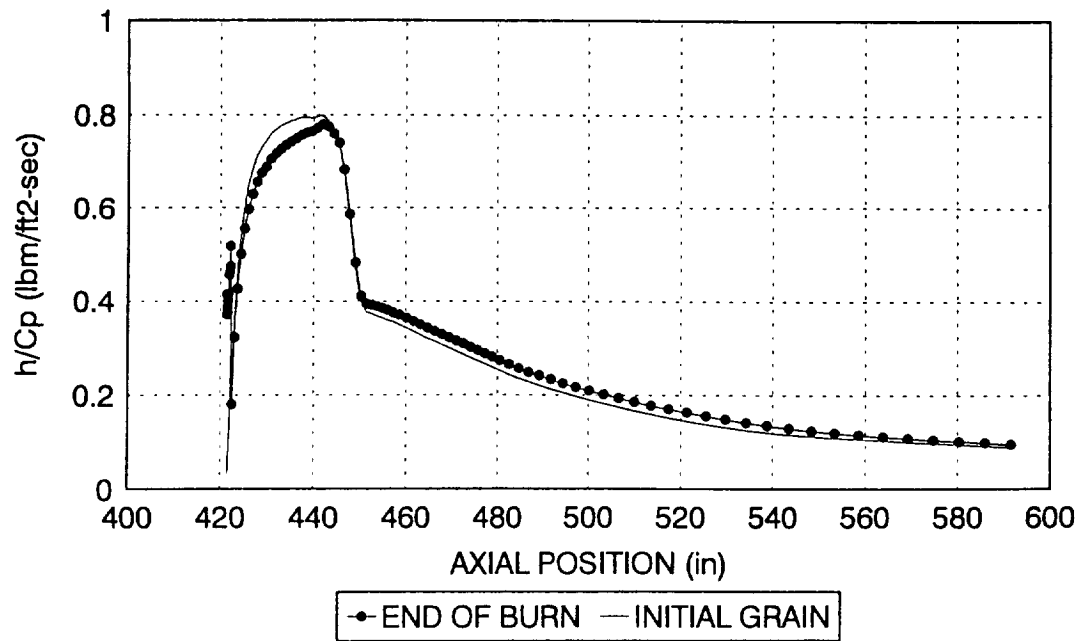


Figure 50. Comparison of Heat Transfer Coefficients for Initial Grain and EOB Geometries

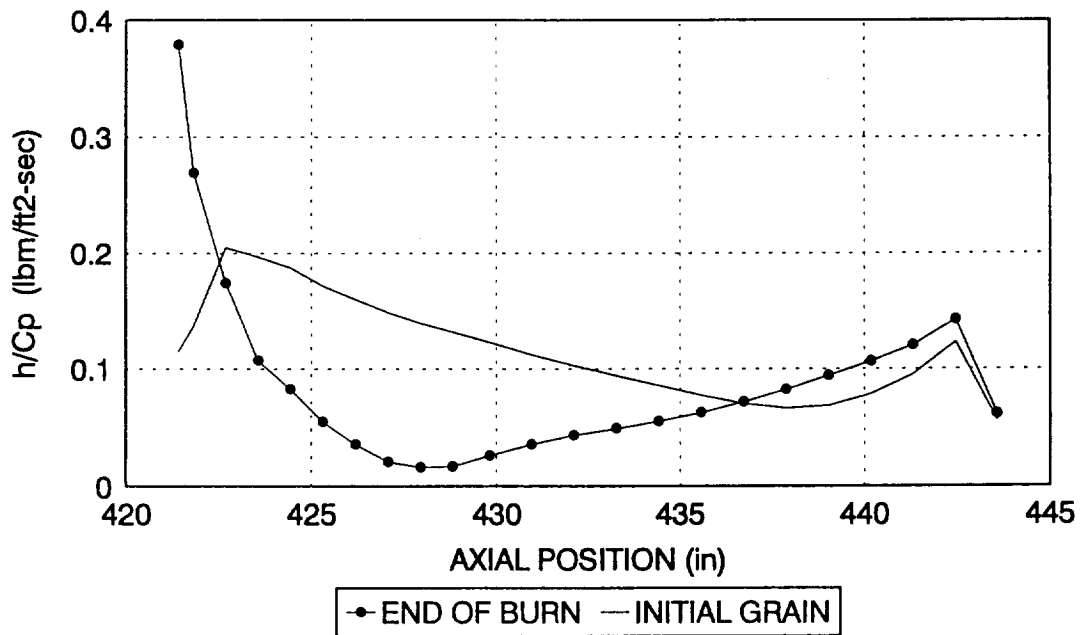


Figure 51. Comparison of Heat Transfer Coefficients for Initial Grain and EOB Geometries, Submerged Region



Table 6. ASRM Nozzle Heating Conditions

Station	Q_{RAD} (BTU/ft ² -sec)	F	H_R (BTU/lbm)	h/C_p (lbm/ft ² -sec)	Pe (atm)
1	752.81	1.0	1122.2	0.131	35.9
2	792.64	1.0	1186.4	0.071	39.4
3	794.68	1.0	1199.6	0.332	39.6
4	751.00	1.0	1191.2	0.685	35.6
5	700.60	1.0	1177.4	0.769	31.4
6	653.94	1.0	1172.5	0.794	27.7
7	519.34	1.0	1175.7	0.740	18.1
8	322.21	0.998	882.3	0.376	7.81
9	282.70	0.989	865.6	0.335	6.45
10	213.24	0.964	854.0	0.260	4.37
11	176.08	0.942	851.0	0.370	3.44
12	127.22	0.898	842.9	0.221	2.36
13	87.36	0.841	803.9	0.148	1.58
14	83.73	0.833	800.4	0.145	1.50
15	72.83	0.792	800.5	0.122	1.27
16	71.22	0.783	800.5	0.116	1.23
17	68.81	0.769	798.3	0.109	1.15

fs:asrm1ab

Table 7. ASRM Flex Seal Heating Conditions

Pressure (atm)	HR (BTU/lbm)	H/Cp (lbm/ft ² -sec)	F	Q _{RAD} (BTU/ft ² -sec)
40.7	1188	0.0687 (IG) 0.0608 (EOB)	1.0	752

The ASRM Motor experiences a relatively large variation in pressure during the course of the motor burn, see Figure 6. Because of this, the approximation given in equation 1 to account for chamber pressure variations was compared to accurate boundary layer solutions for another pressure condition. Table 8 presents results from this comparison. This table presents the heat transfer coefficient calculated by NAT for two different chamber pressures, 616 psi and 910 psi. Both of these calculations were performed for the initial grain geometry. Results are presented at five locations within the nozzle. The pressure of 910 psi was selected because it is the maximum pressure the ASRM motor will experience. The heat transfer coefficient calculated with equation 1 is shown for comparison and the percent difference is also given. Equation 1 does an excellent job of predicting heating conditions near the nozzle throat but then slightly underpredicts heating in the exit cone. The differences, however, were considered small enough that equation 1 was used for locations throughout the nozzle.

Table 8. Comparison of Calculated and Approximated Heat Transfer Coefficients

Location	Axial Position (ins)	(h/cp) ₆₁₆ (lbm/ft ² -sec)	(h/cp) ₉₁₀ (lbm/ft ² -sec)	(PRAT) ⁸ (h/cp) ₆₁₆ (lbm/ft ² -sec)	difference (%)
Throat Entrance	425.1	0.5820	0.7928	0.7948	.25
Throat Entrance	442.0	0.7818	1.067	1.0677	.07
Throat	446.6	0.6590	0.9147	0.9000	-1.61
FWD Exit Cone	454.9	0.3543	0.4993	0.4839	-3.08
AFT Exit Cone	489.2	0.2194	0.3043	0.2996	-1.54

fs:7186cht.doc

3.2.1 Material Interface Heating

A material interface heating calculation was performed for the ASRM nozzle using the same procedures as described in Section 3.1.1 for the MNASA nozzle. This calculation was performed for the location in the nozzle where the material changes from

standard density MX4996 carbon phenolic to low density FM5939 carbon phenolic. The "interface heating" condition was determined by simply using the flow results for the initial grain geometry and starting the boundary layer solution at the material interface location. Results from this calculation are presented in Figure 54. This figure compares the augmented heating results (i.e., starting the boundary layer solution at the material interface) to the unperturbed solution. The results are presented as a function of streamlength beginning at the interface and continuing to the exit plane of the nozzle. Heating conditions nearest the interface are increased by nearly 100%. However, this effect falls off down the exit cone until the augmentation is only about 10% at the exit plane of the nozzle.

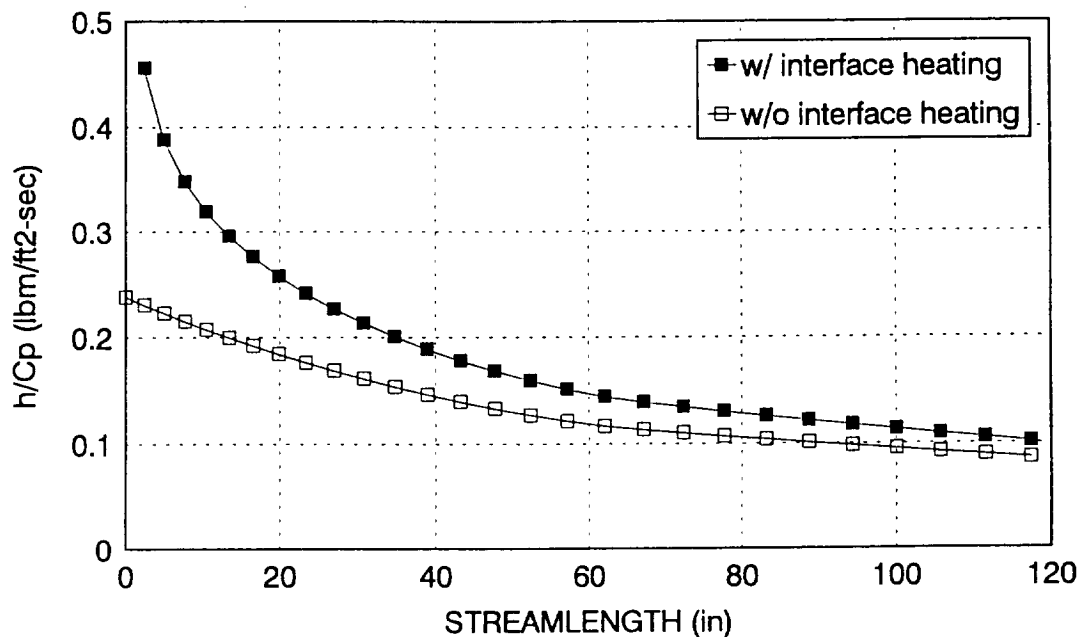


Figure 54. Augmented Heating Rates at the Exit Cone Material Interface

3.2.2. Particle Flow Calculations

Particle flow calculations were performed for the ASRM nozzle using the same procedures as for the MNASA nozzle. These calculations incorporated lessons learned from the MNASA calculations to improve upon accuracy and efficiency. The calculations were performed to determine the location and severity of particles impacting on the nozzle surface. To perform these calculations, three particle flow grids were generated. These grids, shown in Figures 55 through 57, are somewhat more coarse than the grids used for the flow solutions. Some degree of grid refinement was maintained in the regions of the nozzle adjacent to the nose. This was done so that particle impacts in this region could be accurately calculated. The three grids represent three separate points during the motor burn. The first grid is for the initial grain configuration. The second grid is for an intermediate point in time, 24 seconds into the firing. The third grid is the EOB

configuration and represents the motor geometry 112 seconds into the firing. Four different particle diameters (1, 3.5, 10, and 120 μm) were considered in these calculations. Table 9 presents a summary of the various particle flow calculations which were performed.

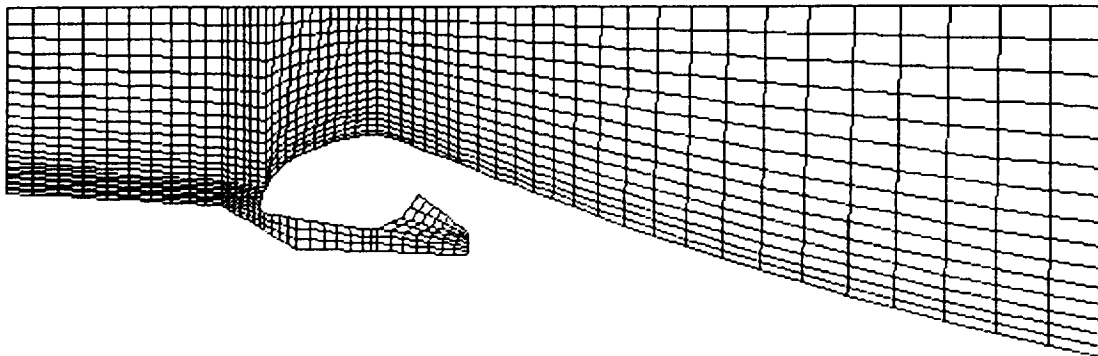


Figure 55. ASRM Nozzle Particle Flow Grid, Initial Grain Configuration

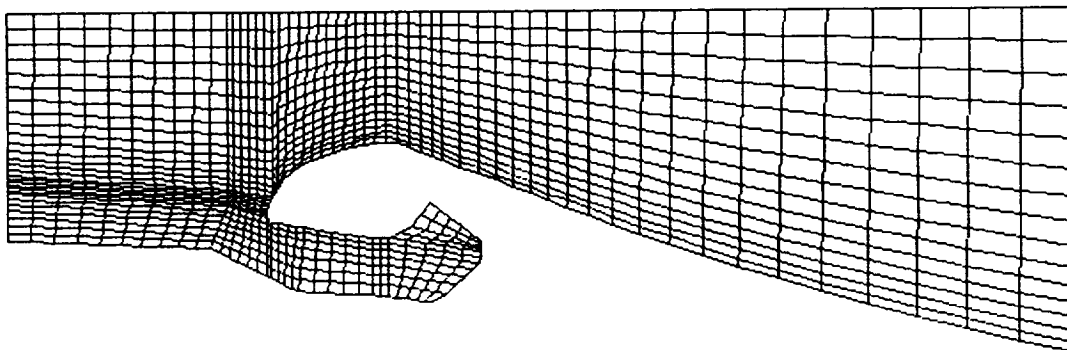


Figure 56. ASRM Nozzle Particle Flow Grid, Intermediate Grain Configuration

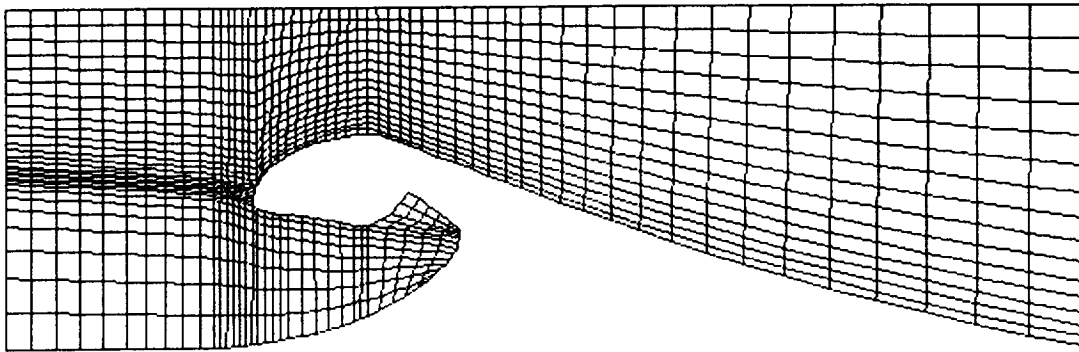


Figure 57. ASRM Nozzle Particle Flow Grid, EOB Grain Configuration

Table 9. ASRM Nozzle Particle Analysis Cases

Grid	Particle Diameter (μm)			
	1.0	3.5	10.0	120
Initial	X	X	X	X
Intermediate				X
EOB	X		X	X

Figures 58 through 66 present parcel velocity results for the initial grain configuration. Results are presented for particle sizes of 1, 10 and 120 μm . Three figures are presented for each particle size. Each figure represents a slice in time and shows velocities for selected parcels. The sequence of figures shows how the particle flow develops. Notice that it takes less than 0.02 second for the particle flow fields to fully develop. Figures 67 through 69 present similar results for all three particle sizes with the EOB configuration. For this configuration, about 0.04 second is required for a fully developed particle flowfield. This is primarily because of the much lower inflow velocities for this configuration. These figures present results for a single point in time and show the fully developed particle flow. Following are comments relative to the figures:

1. The 1 and 10 μm particles tend to follow the flow stream lines. They both come very close to impacting the nozzle in the throat entrance region but turn prior to impacting.
2. The 120 μm particles do not follow the flow stream lines as closely and impact the nozzle surface in the throat entrance region early in time and in the submerged region late in time (i.e., at end of burn).
3. The smaller particles (i.e., the 1 and 10 μm diameters) follow the flow stream lines and expand to near the surface in the nozzle exit cone. There is very little difference between the initial and EOB configurations.
4. The 120 μm particles tend to form more of a core in the exit cone and do not even come close to the exit cone surface. This core becomes tighter later in time, i.e., is located nearer the centerline.

Based on the diversity of the impact results for the initial and EOB configurations, it was determined that it would be necessary to run particle flow calculations for at least one additional point in time. This was necessary so that particle impact conditions could be defined as a function of time for the erosion calculations. The grain configuration shown in Figure 56, corresponding to 24 seconds after motor ignition, was selected as the intermediate point. Calculations were performed for only the 120 μm particle size. Results for this calculation are presented in Figure 70. It appears that this calculation does a good job of bridging the impact conditions from the initial and EOB grain configurations. Impacts are calculated to occur in both the throat entrance and submerged regions of the nozzle.

One final particle flow calculation was performed for the nozzle. This calculation was performed explicitly to try to produce impacts in the exit cone. This calculation was performed for the initial grain geometry and a 3.5 μm particle diameter. This particle diameter was selected based on information from Eric Wernimont of Aerojet¹⁰. Results from this calculation are given in Figure 71. Particle trajectories are calculated to come slightly closer to the exit cone than for either the 1 or 10 μm particles, but still no impacts are calculated to occur.

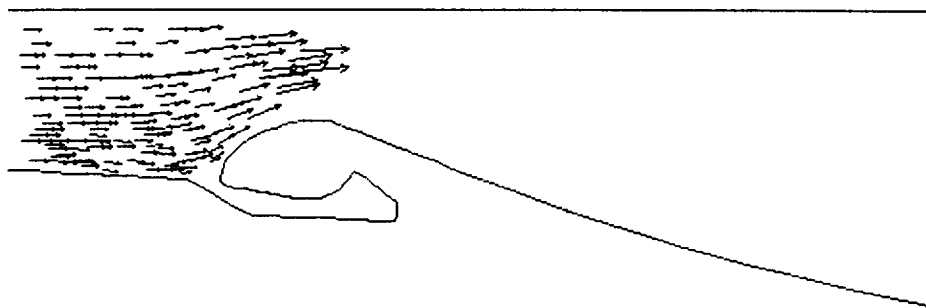


Figure 58. ASRM Particle Flow Results, Initial Grain 1 μm Particles,
Time = 0.0090 second

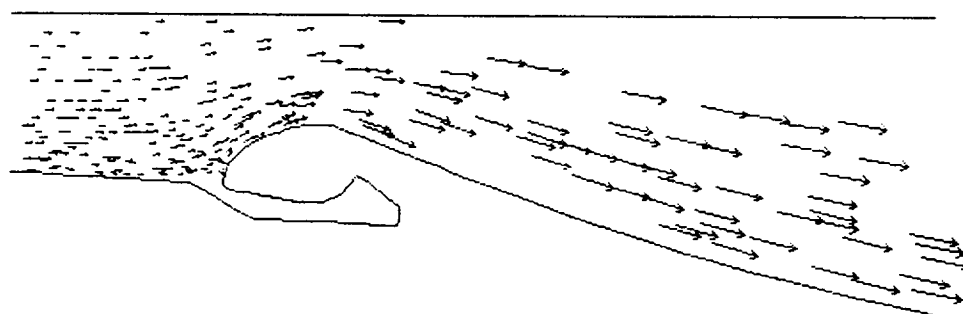


Figure 59. ASRM Particle Flow Results, Initial Grain 1 μm Particles,
Time = 0.0116 second

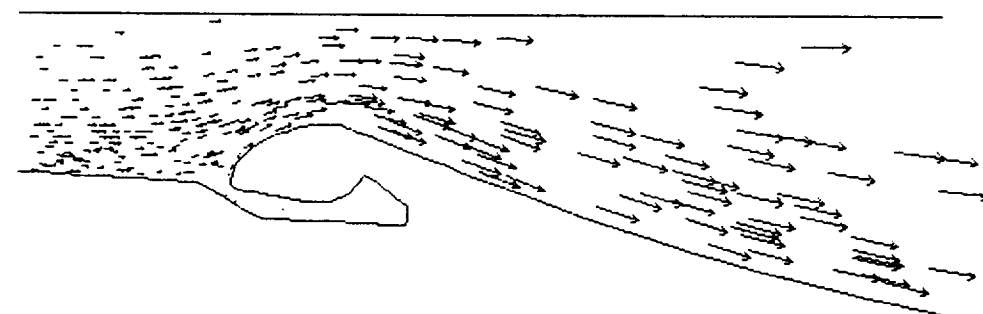


Figure 60. ASRM Particle Flow Results, Initial Grain 1 μm Particles,
Time = 0.0343 second

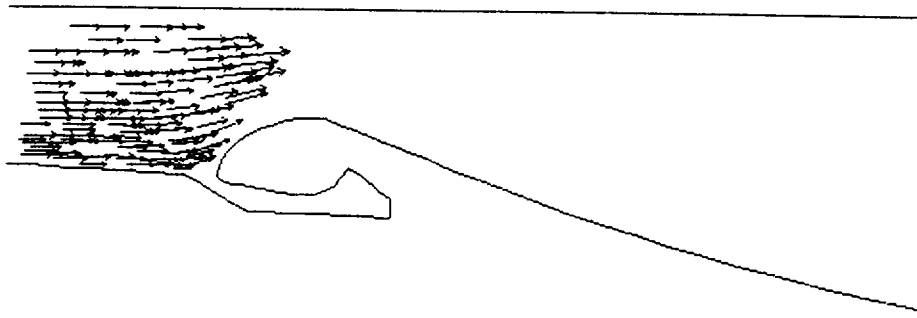


Figure 61. ASRM Particle Flow Results, Initial Grain 10 μm Particles,
Time = 0.0086 second

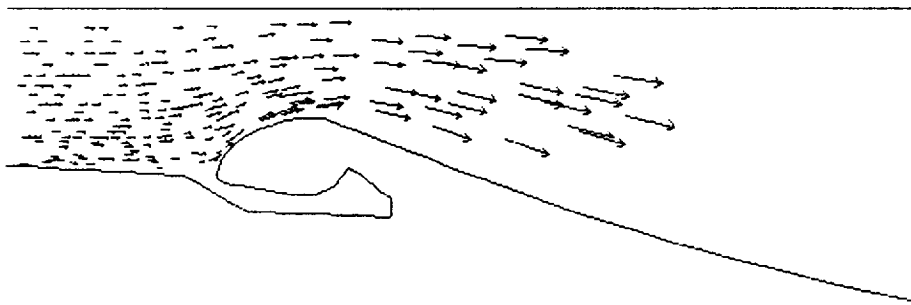


Figure 62. ASRM Particle Flow Results, Initial Grain 10 μm Particles,
Time = 0.0104 second

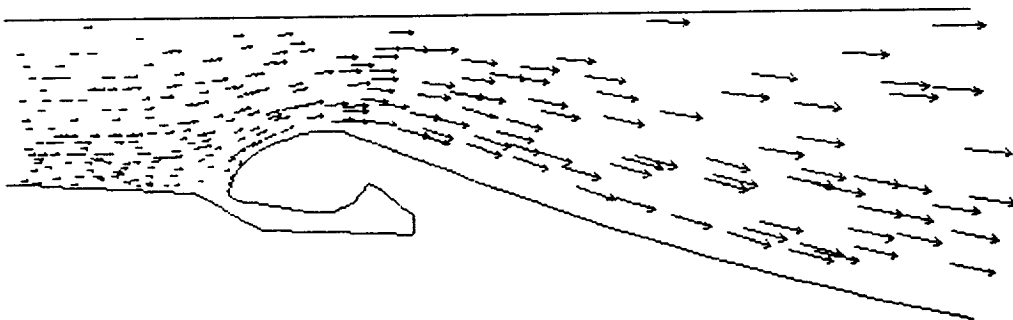


Figure 63. ASRM Particle Flow Results, Initial Grain 10 μm Particles,
Time = 0.0195 second

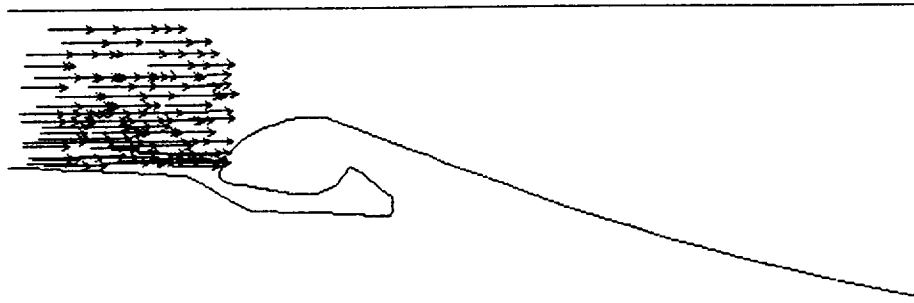


Figure 64. ASRM Particle Flow Results, Initial Grain 120 μm Particles,
Time = 0.0082 second

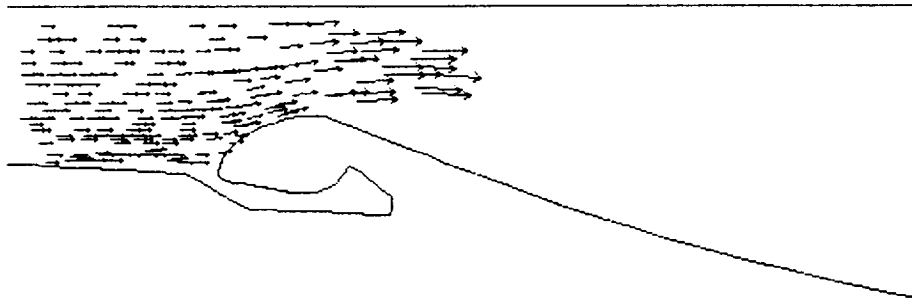


Figure 65. ASRM Particle Flow Results, Initial Grain 120 μm Particles,
Time = 0.0110 second

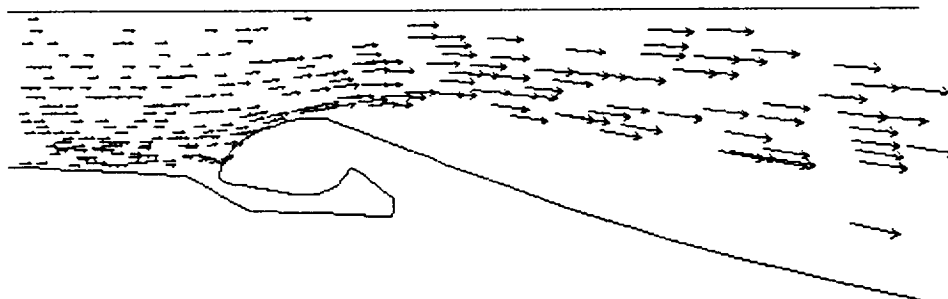


Figure 66. ASRM Particle Flow Results, Initial Grain 120 μm Particles,
Time = 0.0163 second

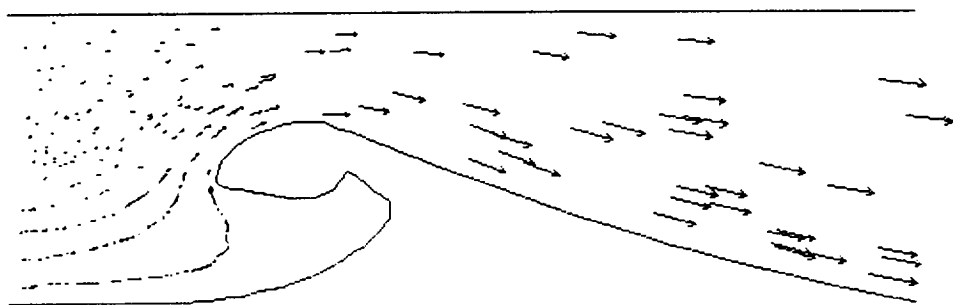


Figure 67. ASRM Particle Flow Results, End of Burn 1 μm Particles

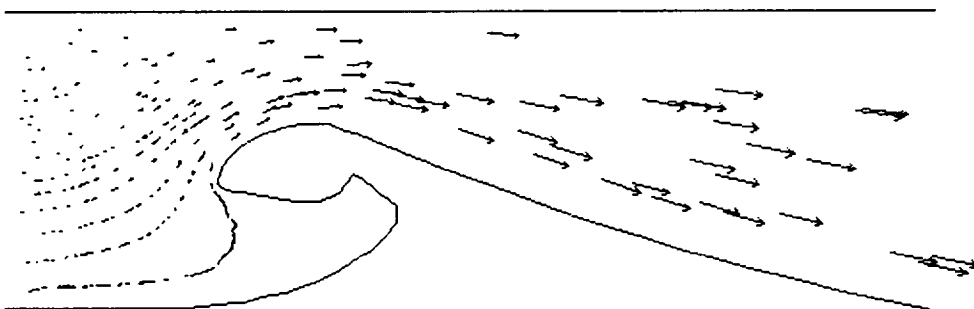


Figure 68. ASRM Particle Flow Results, End of Burn 10 μm Particles

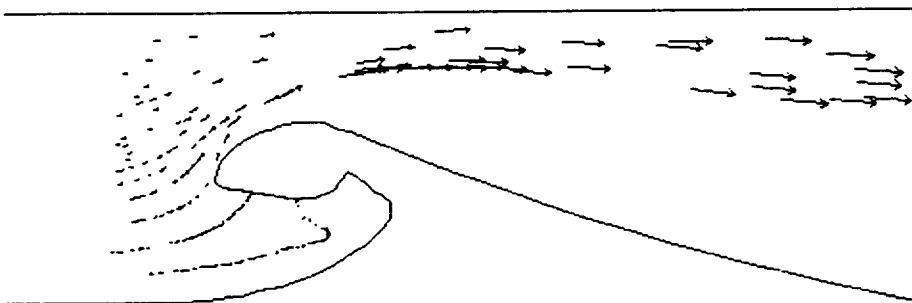


Figure 69. ASRM Particle Flow Results, End of Burn 120 μm Particles

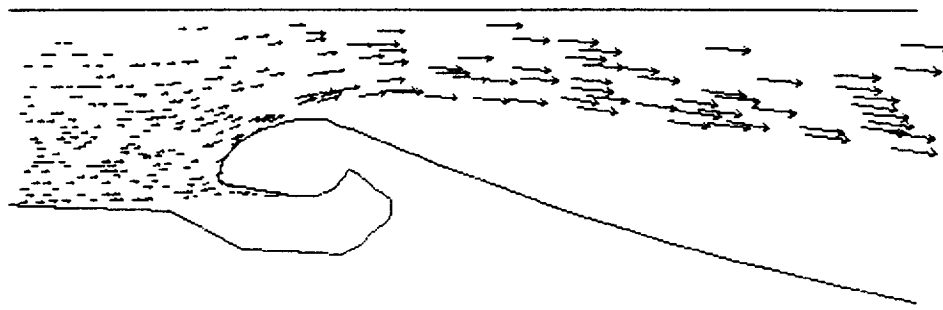


Figure 70. ASRM Particle Flow Results, Intermediate Grain 120 μm Particles

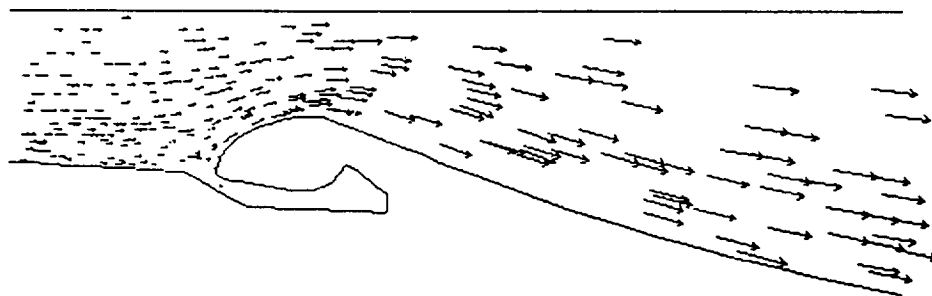


Figure 71. ASRM Particle Flow Results, Initial Grain, 3.5 μm Particles

Particle mass fluxes were determined for the ASRM nozzle using the same procedures as for the MNASA nozzle. The total number of parcel impacts was determined for a period of time and then the particle mass flux per unit area was determined. The Salita⁷ data was again used to account for particle size distributions. Based on Figure 23 the impacting mass flux was taken as 35% of the calculated amount for the 120 μm particles.. These mass flux results are presented in Figure 72. This figure shows the calculated mass fluxes as a function of radial position in the nozzle. Results are presented for three points in time, initial (INIT), intermediate (INT), and end of burn (EOB). For reference, the throat radius is 27.2 inches and the nose radius is 40.07 inches. The corresponding impact angle and impact velocity results are presented in Figures 73 and 74. Following are comments relative to these figures.

1. The greatest mass fluxes occur early in time and are approximately five times greater than those generated in the MNASA motor.
2. The impacting mass fluxes drop off significantly with time and for the EOB configuration are actually less than the MNASA levels.

3. For the initial grain, the impact angles are relatively low near the nozzle throat and approach 70 degrees near the nose. The same is true for the intermediate grain.
4. Impact angles for the submerged region are very small for the intermediate time and approach 90 degrees for the EOB configuration.
5. Impact velocities are highest early in time and drop off to around 100 ft/sec at the end of burn. The higher velocities are a result of the high inflow velocities which are caused by the relatively small difference between the throat area and grain bore area early in time. These inflow velocities drop off significantly as the grain recedes. Impact velocities drop off a corresponding amount.

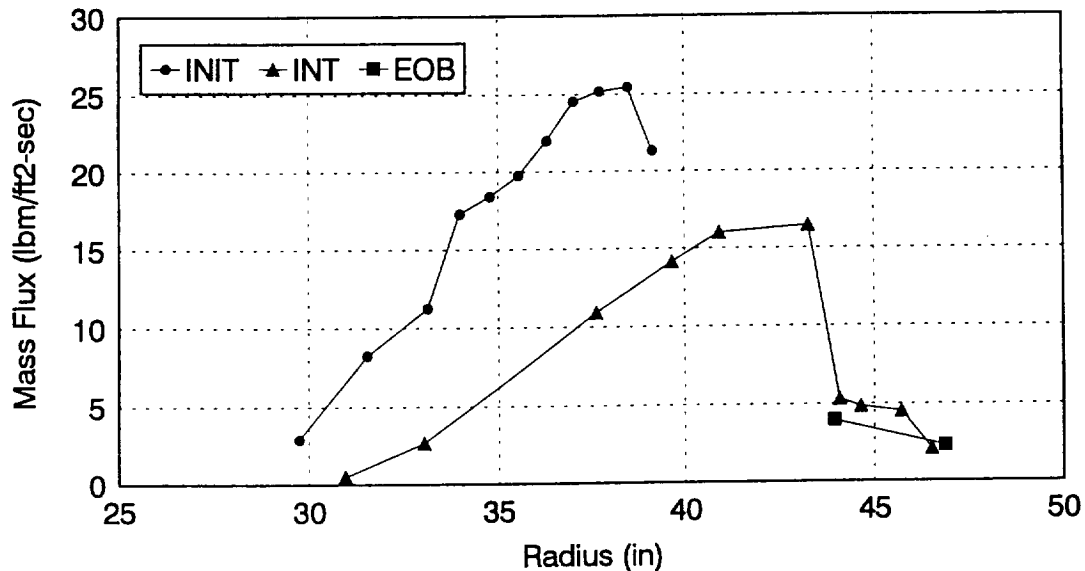


Figure 72. ASRM Particle Mass Fluxes

The data in Figures 72 through 74 was used to determine particle impact conditions at each of the affected ASRM nozzle analysis locations. The calculations showed impacts to occur only at analysis locations 1 through 5. These conditions are presented in Figures 75 through 77. These figures present impacting mass flux, incidence angle and impact velocity as a function of time.

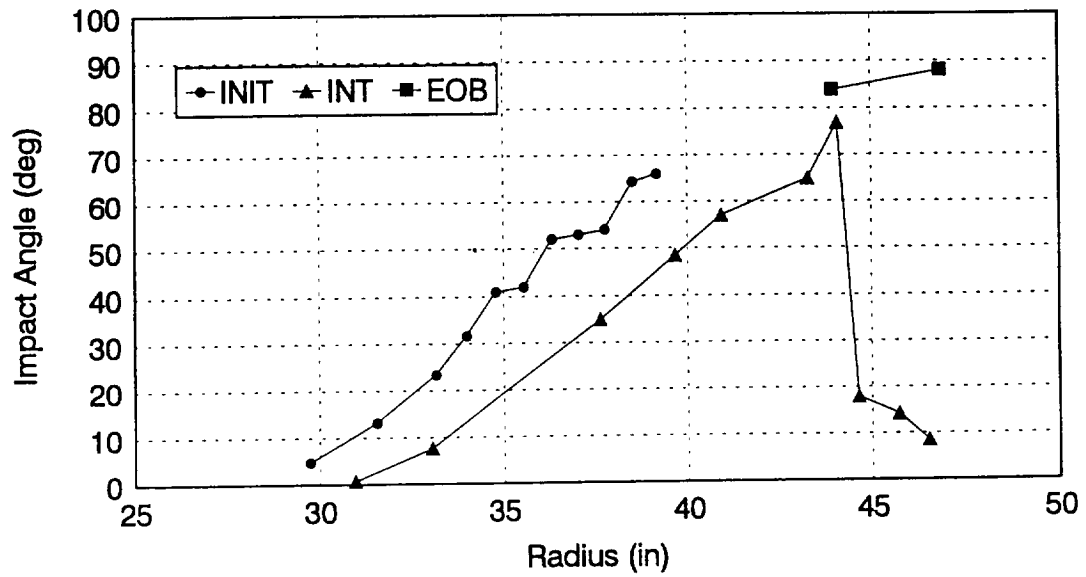


Figure 73. ASRM Particle Impact Angles

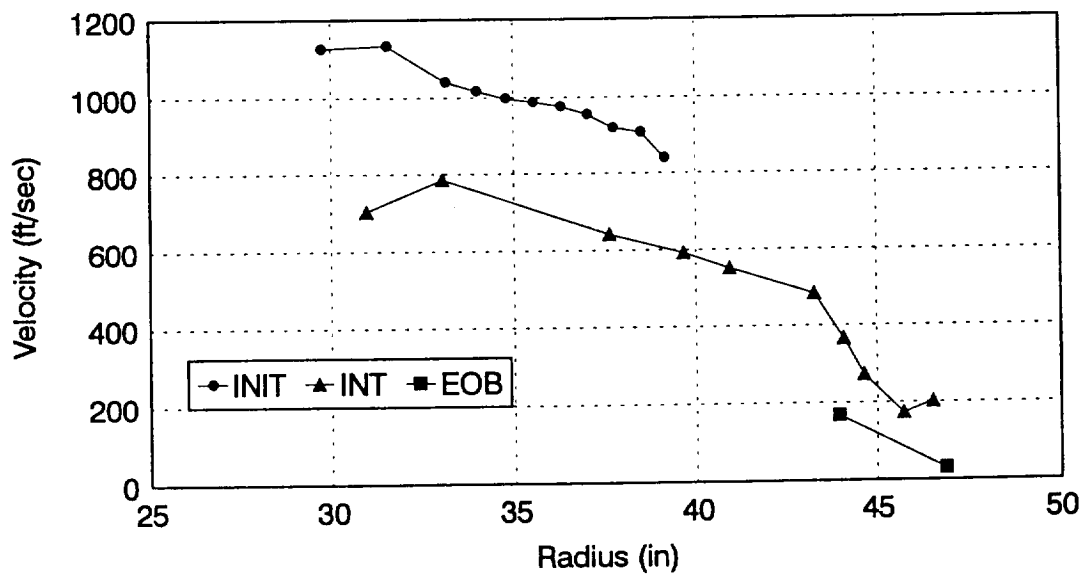


Figure 74. ASRM Particle Impact Velocities

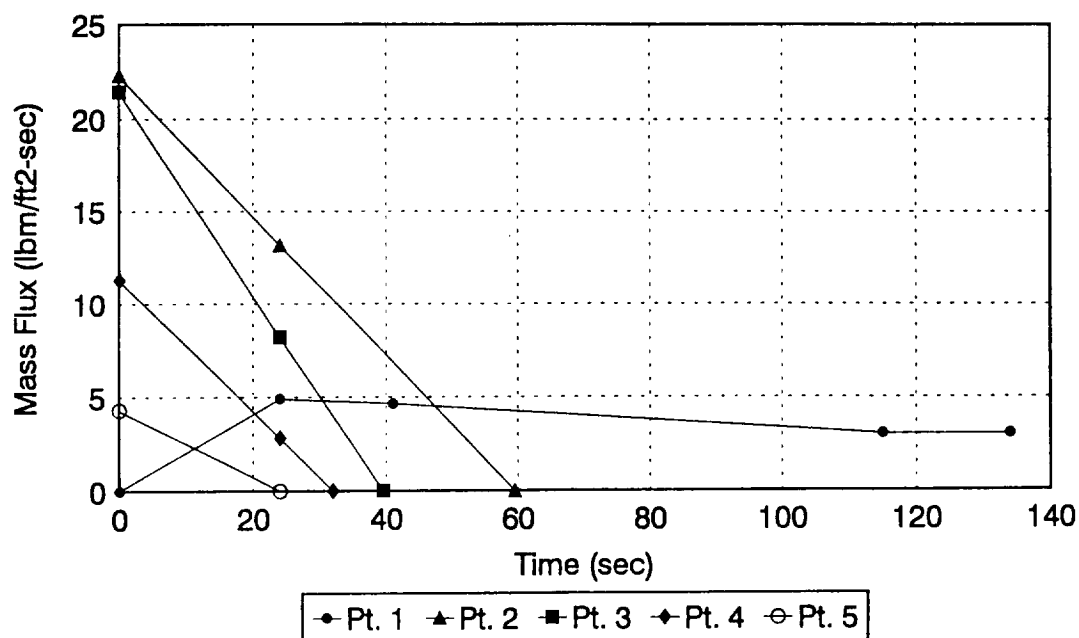


Figure 75. Particle Mass Fluxes at ASRM Analysis Locations

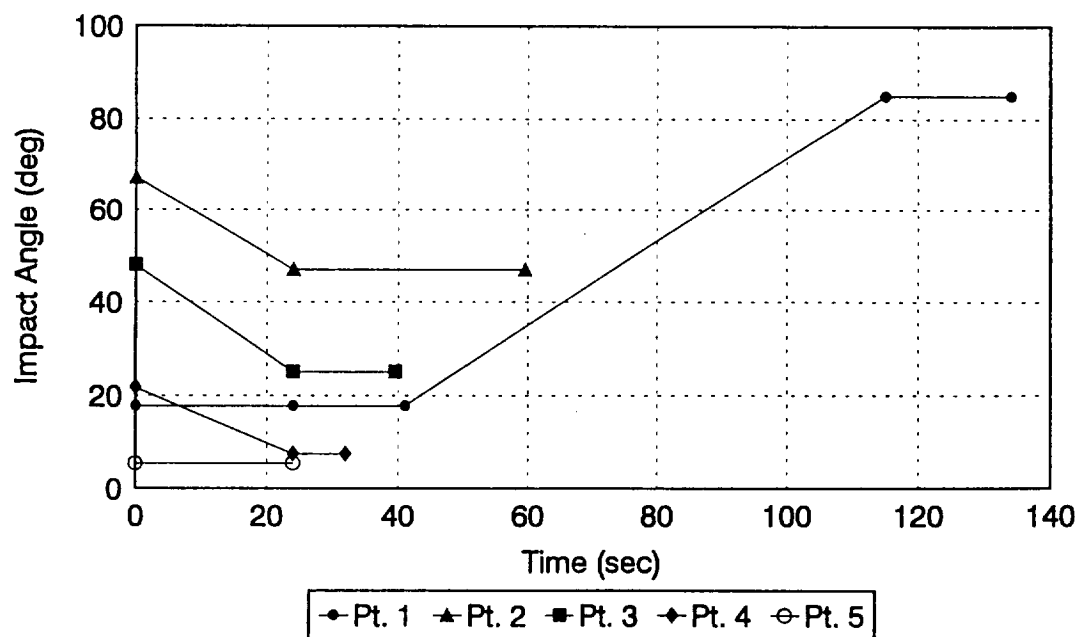


Figure 76. Particle Impact Angles at ASRM Analysis Locations

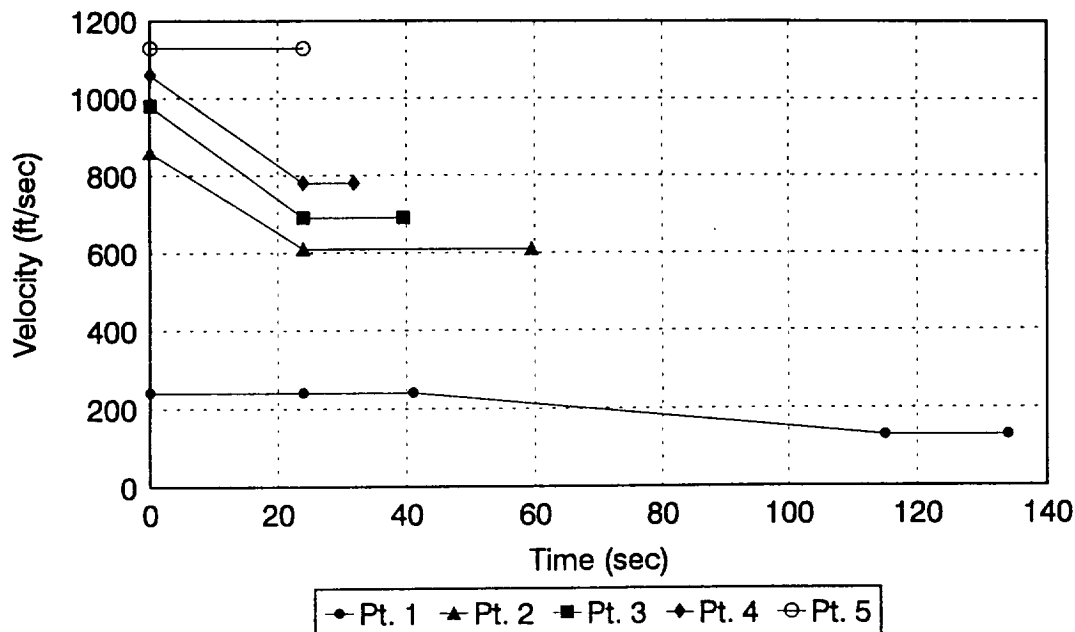


Figure 77. Particle Impact Velocities at ASRM Analysis Locations

3.3 SURFACE THERMOCHEMISTRY

Surface thermochemistry for each of the nozzles was calculated with the ACE module of NAT. These calculations were performed based on the assumption of chemical equilibrium between the pyrolysis gases, the charred surface material and the propellant combustion gases. The composition of the propellant combustion gases was based on an isentropic flow chemical equilibrium composition at the location of interest. The composition of the pyrolysis gases for each of the materials is given in Appendix A. Figures 78 through 80 present representative results for each of the materials considered. These results are presented only for the MNASA motor since the propellant compositions of the two motors are identical. Each figure presents nondimensional surface removal rates, B'_c , as a function of surface temperature. Results are presented for a range of nondimensional pyrolysis gas rates, B'_g . All of these results are typical of carbon phenolics. There is a diffusion limited plateau up to temperatures of about 5000 R at which point the B'_c values begin to increase rapidly with temperature. Larger values of B'_g tend to reduce the level of the plateau and therefore result in lower B'_c 's. This information along with corresponding surface energy fluxes is supplied to the thermal analysis codes and used in their surface energy balance calculations to determine thermochemical erosion rates.

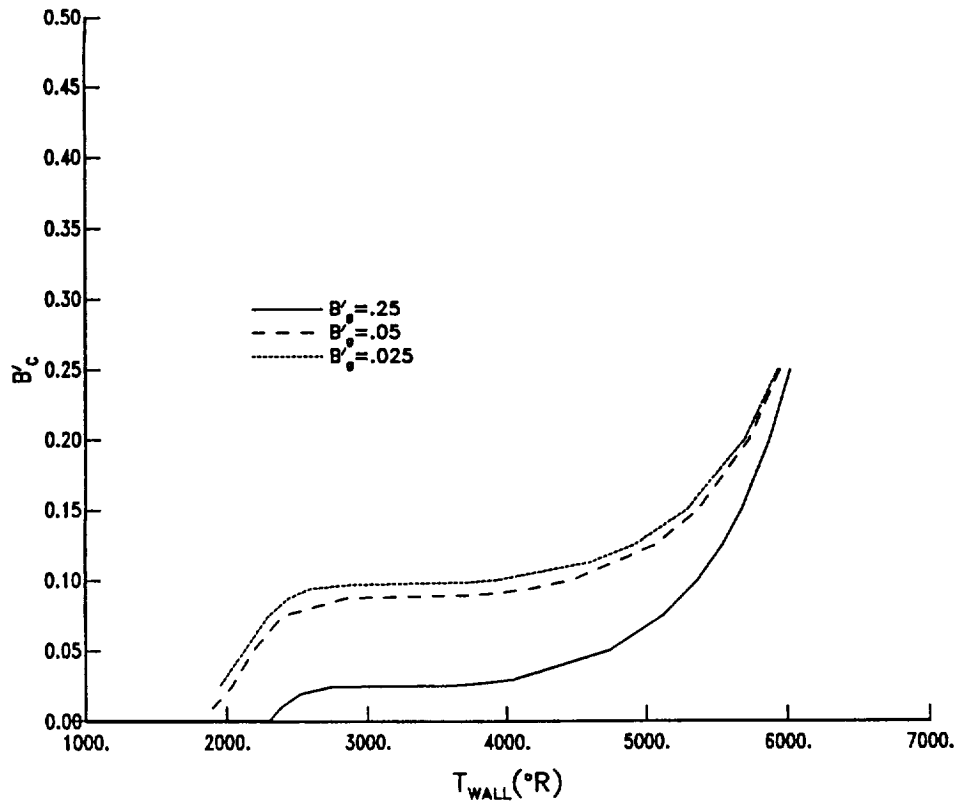


Figure 78. Non Dimensional Ablation Rates for FM5055 Carbon Phenolic

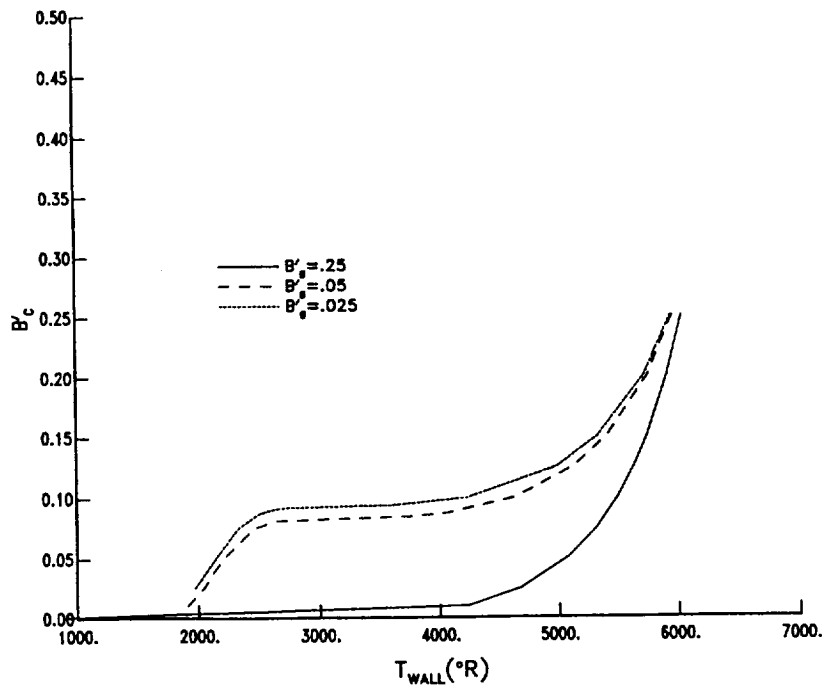


Figure 79. Non Dimensional Ablation Rates for MX4996 Carbon Phenolic

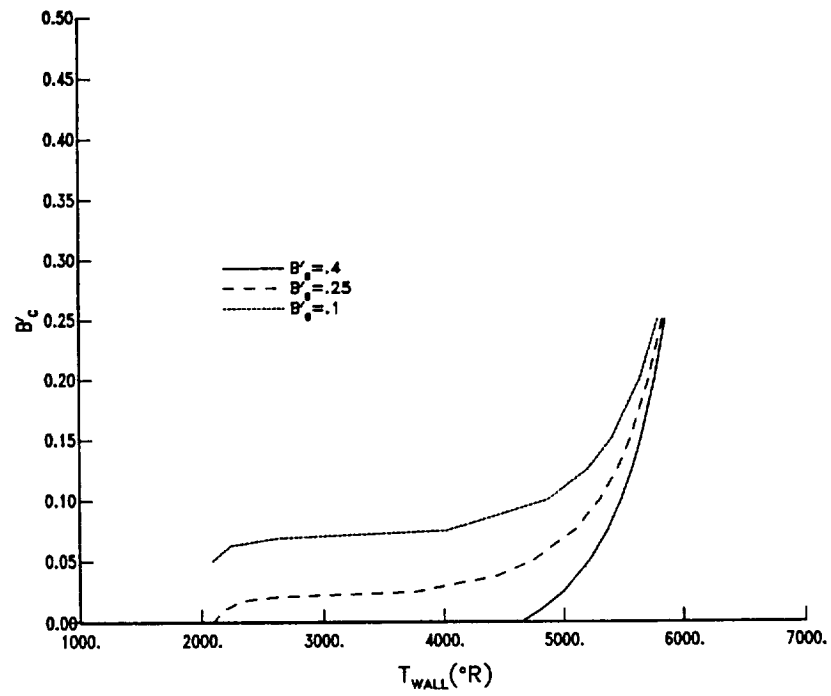


Figure 80. Non Dimensional Ablation Rates for FM5939 Carbon Phenolic

4.0 NOZZLE MATERIAL RESPONSE CALCULATIONS

This section presents results from material response calculations which have been performed for both the MNASA and ASRM nozzles. These calculations include surface erosion and in-depth heating of the nozzle materials. The procedures used in these analyses have been to predict erosion and char depths for the MNASA nozzle and compare to the measured data. This comparison was made to validate the analysis procedures and material models which had been used. Calculations were then performed for the ASRM nozzle to evaluate the adequacy of the design.

4.1 ANALYSIS PROCEDURES

Thermal and ablation calculations have been performed with the Charring Material Ablation computer code (CMA, reference 11) and the Aerotherm Axi-Symmetric Transient Heating and Material Ablation computer code (ASTHMA, reference 12). CMA was used in all nozzle positions where a one dimensional heat conduction response was considered a valid assumption. The ASTHMA code was used only to analyze the flex seal specimen in the MNASA motor tests (This analysis was performed in conjunction with the development of a polyisoprene model and is described in Appendix B). Surface boundary conditions and thermochemistry tables were generated with the NAT computer code and described in the previous section. The material models which were used in these analyses are described in Appendix A. It should be pointed out that the models used for the MX4996 and FM5939 carbon phenolics should be considered preliminary since they are based on laboratory data and inferred from other carbon phenolic materials. Additional testing in the Southern Research Analog Facility and the Aerotherm Arc Plasma Generator are needed to fully characterize the material and develop a model which can be used with a high level of confidence. This is especially true for the in-depth heating and decomposition calculations. The calculated surface erosion rates would not be expected to change significantly with a modified model.

To account for the augmented heating which occurs at the material interface in the exit cone the augmented heating rates presented in Figures 21 and 54 were applied when the differential recession was calculated to exceed the local boundary layer thickness. The differential recession was calculated based on unaugmented rates. For the MNASA nozzle, this condition (i.e., differential recession greater than boundary layer thickness) was calculated to occur at 8.8 seconds into the motor firing. The boundary layer thickness at the material interface location was calculated to be 0.010 inch. For the ASRM nozzle the augmented heating conditions were not applied until 48 seconds into the firing. This is because the boundary layer thickness for this nozzle is calculated to be 0.068 inch and therefore a much greater amount of time must elapse for the differential erosion to exceed the boundary layer thickness.

A model to predict the surface erosion of the polyisoprene was developed under this program. This model was developed to match the surface erosion rates of the polyisoprene sample in the MNASA motor. This model treats the material as a surface sublimator. A more detailed description of the model is contained in Appendix B. Again,

this model is based on a limited amount of data and any calculations for the polyisoprene should be considered preliminary.

An erosion model, described in Reference 9, was used to account for material removal due to particle impacts. This model was developed for graphite but was used for the carbon phenolic materials in the MNASA and ASRM nozzles. It was necessary to use this graphite material model since no particle erosion data exists for carbon phenolic. The procedure for modeling the erosion, described in Reference 9, treats material removal due to both chemical and mechanical effects of the particulates. Mechanical effects are modeled with an expression of the form:

$$G_{\text{mech}} = a D^b V^c (\sin \alpha)^d \quad (3)$$

where,

G	=	ratio of mass of target material removed to mass of incident particles
V	=	particle velocity
D	=	particle diameter
α	=	angle of impact relative to the surface
a,b,c,d	=	empirically determined constants

The study in Reference 9 developed the following expression for graphite mechanical erosion.

$$G_{\text{mech}} = 5.342 \times 10^{-7} D^{0.799} V^{1.24} (\sin \alpha)^{0.299} \quad (4)$$

The units for D and V are μm and ft/sec, respectively.

The Reference 9 study also found that material removal can occur due to chemical attack of either aluminum or alumina (Al_2O_3) particles. This attack was characterized with an expression of the form:

$$G_{\text{chem}} = a'(DV \sin \alpha)^{b'} \quad (5)$$

where a' and b' are different for aluminum and alumina. The correlation for aluminum particles was:

$$G_{\text{chem}} = 1.113 \times 10^{-5} (DV \sin \alpha)^{0.8} \quad (6)$$

and for alumina:

$$G_{\text{chem}} = 386.7(DV \sin \alpha)^{-1.13} \quad (7)$$

These same expressions were used to model the chemical erosion of carbon phenolic, and since they are based on relative mass rates (i.e., mass removed/mass incident), they are expected to do a reasonable job of predicting erosion for carbon phenolic. This is because

the relative mass rates effectively account for density differences between the graphite and charred carbon phenolic (i.e., this expression will predict greater material removal for carbon phenolic than for graphite). For this study, all particles within the two motors were assumed to be alumina. This may be realistic for the MNASA motor because of the large distance between the propellant and the nozzle (and therefore sufficient time for the aluminum to react with oxygen to form alumina). However, this may not be representative for the ASRM where the propellant is packed near the submerged nozzle region.

4.2 MNASA NOZZLE EROSION

The calculated thermochemical erosion depths for the MNASA nozzle are presented in Figure 81. These results are compared to the measured values at locations 4 through 40. Following are comments relative to these results:

1. The calculated and measured erosion depths compare very well at locations 4, and 13 through 33. The exceptions to the good comparison appear to be in regions of the nozzle where particle impacts are occurring.
2. The calculated and measured erosion in the throat region compare exceptionally well.
3. The calculated erosion levels do a very good job of matching the rapid drop in erosion just aft of the nozzle throat (location 18).
4. The method of accounting for the interface heating appears to do a very good job of calculating the increase in erosion at the material interface. It appears to be slightly conservative (or this could be partly due to the conductivity model for FM5939, see the discussion below) but it does seem to do a good job of matching the characteristic of the erosion aft of the interface, i.e., gradually falling off down the length of the exit cone.

Erosion results considering combined thermochemical and particle erosion are presented in Figure 82. The particle erosion effects only stations 5 through 12 and stations 34 through 40. Therefore, the remaining stations experience only thermochemical erosion and the results at those stations are identical to those presented in Figure 81. The calculated erosion at stations 5 through 12 compare very well with the measured values. Several features of this comparison are important:

1. The particle impacts are calculated to effect only stations 5 through 12 in the nozzle entrance region. This is completely consistent with the measure results.
2. The magnitude of the erosion compares very well with the measured values. This is especially true for stations 5 through 10. At stations 11 and 12 the comparison could possibly be much better if the NAT analysis grid had been further refined and the impacts at those locations more accurately calculated. The impact conditions were extrapolated from the results based on the "area effected method" described in section 3.
3. Based on the relatively good agreement with measured data no attempt was made to update or modify the G law correlations from Reference 9.

The matching of the particle erosion effects in the nozzle exit cone was based on backing out particle impact conditions. Recall from section 3 that no particle impacts were calculated to occur in the nozzle exit cone. Therefore, the impacting mass flux was backed out to match the erosion data. The impacting particle diameter was assumed to be 3.5 μm . Since this is such a small particle size the particle velocity was assumed to be equal to the local gas velocity. The impacting angle was assumed to be 5 degrees. Based on all of these assumptions, the impacting mass fluxes, shown in Figure 83, were determined. This figure shows the particle mass fluxes as a function of streamlength. The large values of 4-5.5 $\text{lbm/ft}^2\text{-sec}$ occur in the nozzle entrance region. Mass fluxes in the exit cone are calculated to be only about 0.2 $\text{lbm/ft}^2\text{-sec}$ and increase slightly nearest the exit plane of the nozzle.

Figure 84 presents the total affected depth (TAD) calculated for the MNASA nozzle and compares it to measured results. TAD is the sum of the erosion depth and the post test measured char depth. A summary of the measured and calculated erosion and TAD results is also presented in Table 10. TAD's are presented at the end of the motor burn and following two minutes of cool down. This two minute cool down allowed for heat to continue to soak into the material and additional charring to occur. The cool down environment was not known and therefore it is assumed that only a small amount of heat leaves the nozzle surface due to radiation. A radiation view factor of 0.05 was used at all stations within the nozzle.

The TAD predictions for stations 4 through 24 do a good job of bounding the data. This is the best that can be expected based on the unknown cool down environment. However, beginning at station 26 (this is the location where the FM5939 material begins) the predicted TAD's are below the measured values even with the cool down effects. This is probably due to the material model for FM5939. The conductivity model for the MX4996 was modified (i.e., the conductivities were increased from the laboratory measured values) to be similar to other standard density carbon phenolic material models. This was not done for the low density FM5939 carbon phenolic. Based on these results more data is needed to do a reasonable job of predicting the char depth for the FM5939. Based on the TAD results the thermal conductivity would be expected to be greater than the values used in the analysis. It is interesting to note that an increase in conductivity would result in reduced levels in the calculated thermochemical erosion. This would improve the agreement between measured and calculated erosion for the FM5939, see Figures 81 and 82.

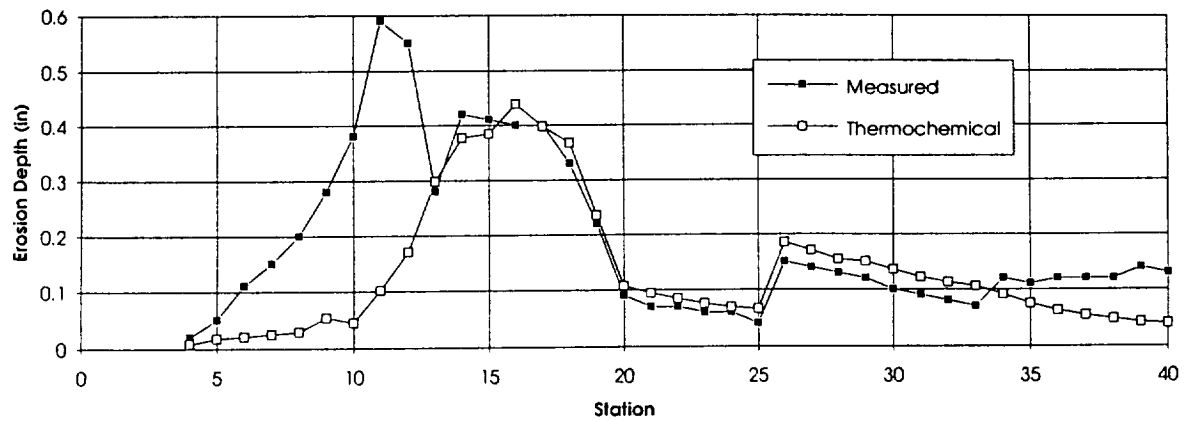


Figure 81. Calculated Thermochemical Erosion Depths for the MNASA Nozzle

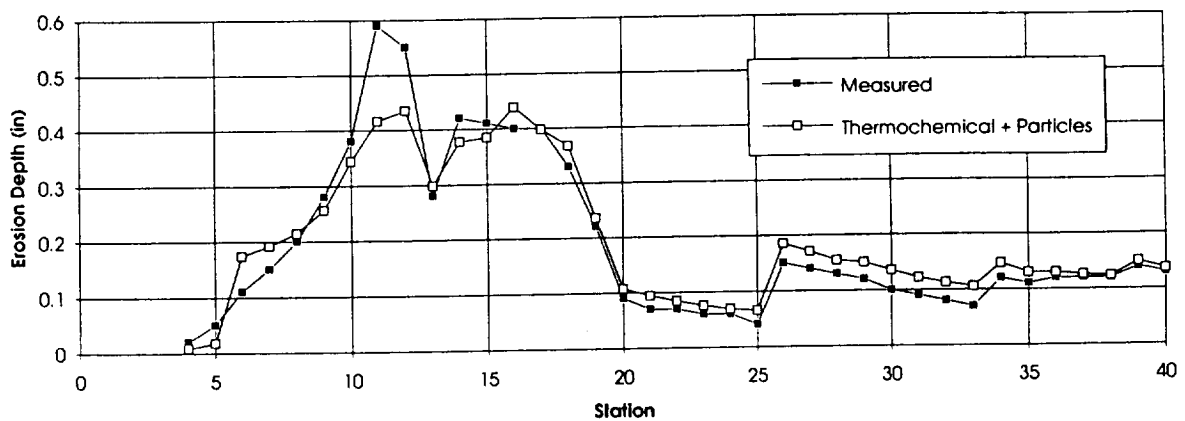


Figure 82. Combined Thermochemical and Particle Erosion Depths for the MNASA Nozzle

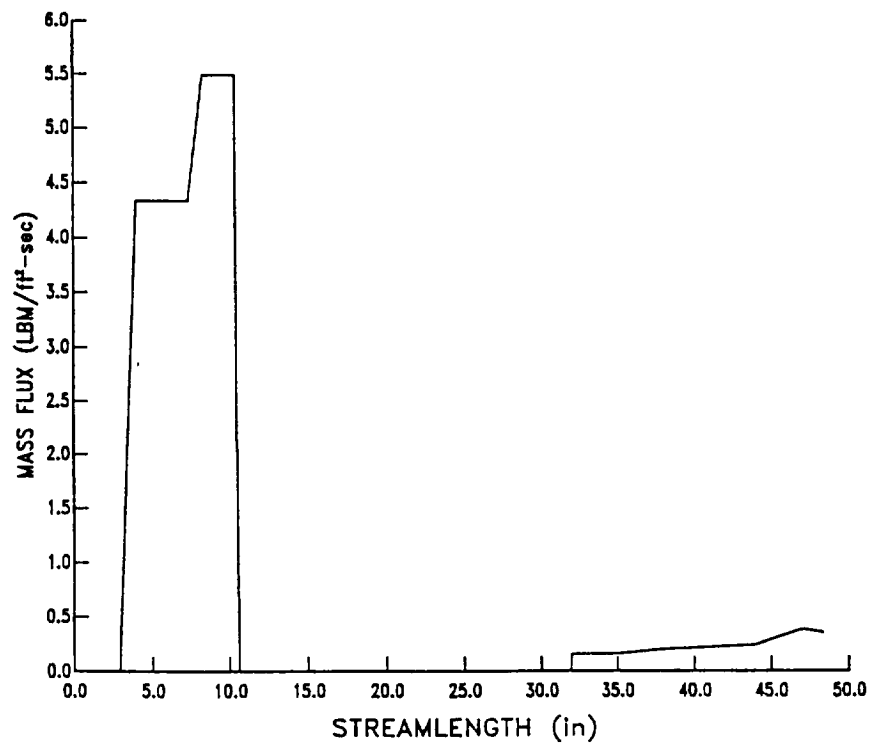


Figure 83. Impacting Particle Mass Fluxes for the MNASA Nozzle

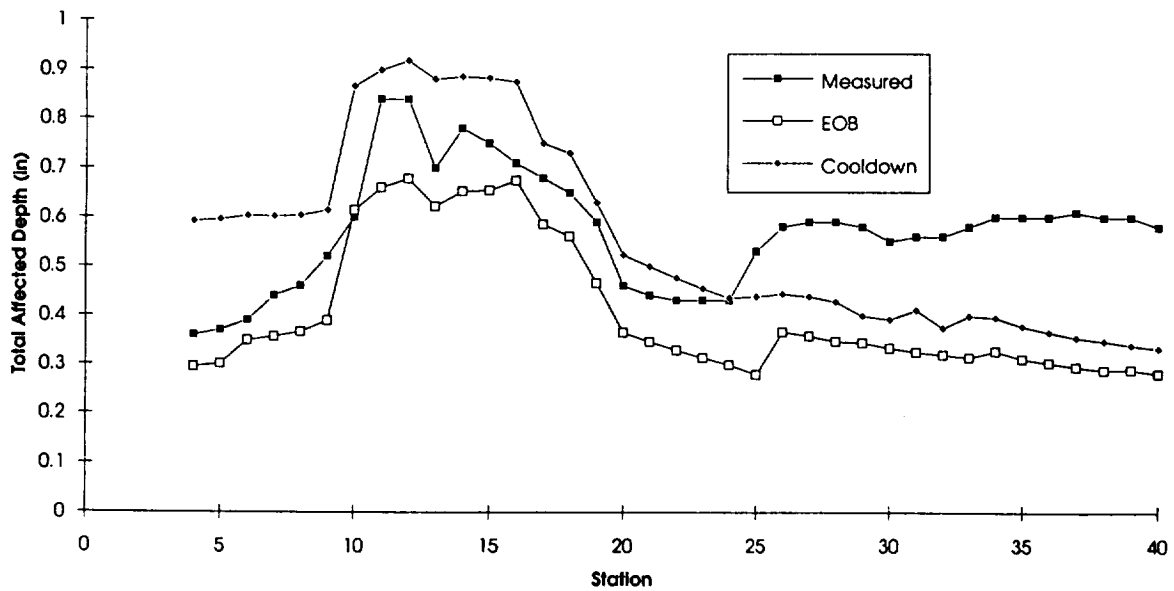


Figure 84. TAD for MNASA Nozzle

Table 10. Erosion and TAD Summary for the MNASA Nozzle

			Thermochemical Erosion			Thermochemical + Particle Erosion			Measured Depth	
Station	Axial Position (in)	Radial Position (in)	Erosion Depth (in)	Char (in)	Depth	Erosion Depth (in)	Char (in)	Depth	Erosion (in)	Char (in)
				EOB	Cooldown		EOB	Cooldown		
4	3.550	10.681	0.008	0.295	0.592	0.008	0.295	0.592	0.02	0.360
5	2.477	10.408	0.018	0.300	0.595	0.018	0.300	0.595	0.05	0.370
6	1.393	10.135	0.021	0.301	0.595	0.174	0.349	0.602	0.11	0.390
7	0.365	9.863	0.025	0.302	0.596	0.192	0.356	0.602	0.15	0.440
8	-0.701	9.590	0.029	0.304	0.596	0.214	0.366	0.603	0.20	0.460
9	-1.923	9.307	0.054	0.315	0.601	0.256	0.389	0.614	0.28	0.520
10	-2.863	9.044	0.045	0.513	0.818	0.344	0.615	0.867	0.38	0.600
11	-3.815	8.590	0.102	0.543	0.842	0.416	0.661	0.899	0.59	0.840
12	-4.232	7.694	0.171	0.571	0.861	0.434	0.679	0.918	0.55	0.840
13	-3.974	6.830	0.298	0.623	0.881	0.298	0.623	0.881	0.28	0.700
14	-3.520	6.224	0.377	0.654	0.887	0.377	0.654	0.887	0.42	0.780
15	-2.361	5.647	0.384	0.655	0.883	0.384	0.655	0.883	0.41	0.750
16	-1.681	5.309	0.439	0.676	0.875	0.439	0.676	0.875	0.40	0.710
17	-1.171	5.055	0.397	0.586	0.750	0.397	0.586	0.750	0.40	0.680
18	0.0	4.983	0.367	0.560	0.730	0.367	0.560	0.730	0.33	0.650
19	0.981	5.149	0.235	0.465	0.630	0.235	0.465	0.630	0.22	0.590
20	2.064	5.629	0.107	0.365	0.523	0.107	0.365	0.523	0.09	0.460
21	2.972	6.045	0.094	0.345	0.499	0.094	0.345	0.499	0.07	0.440
22	3.882	6.458	0.084	0.328	0.476	0.084	0.328	0.476	0.07	0.430
23	4.802	6.857	0.076	0.312	0.454	0.076	0.312	0.454	0.06	0.430
24	5.504	7.145	0.069	0.298	0.431	0.069	0.298	0.431	0.06	0.430
25	6.172	7.430	0.065	0.278	0.437	0.065	0.278	0.437	0.04	0.530
26	6.888	7.712	0.186	0.365	0.443	0.186	0.365	0.443	0.15	0.580
27	7.354	7.893	0.170	0.357	0.437	0.170	0.357	0.437	0.14	0.590
28	7.782	8.070	0.154	0.346	0.427	0.154	0.346	0.427	0.13	0.590
29	8.292	8.245	0.150	0.344	0.398	0.150	0.344	0.398	0.12	0.580
30	9.273	8.584	0.135	0.333	0.390	0.135	0.333	0.390	0.10	0.550
31	10.182	8.912	0.122	0.325	0.410	0.122	0.325	0.410	0.09	0.560
32	11.148	9.229	0.113	0.319	0.373	0.113	0.319	0.373	0.08	0.560
33	12.088	9.534	0.106	0.313	0.398	0.106	0.313	0.398	0.07	0.580
34	14.966	10.386	0.091	0.302	0.386	0.147	0.326	0.395	0.12	0.600
35	17.975	11.154	0.075	0.288	0.371	0.130	0.310	0.377	0.11	0.600
36	20.789	11.838	0.063	0.277	0.358	0.130	0.302	0.365	0.12	0.600
37	23.756	12.457	0.054	0.269	0.348	0.126	0.294	0.355	0.12	0.610
38	26.706	13.010	0.048	0.263	0.340	0.124	0.288	0.347	0.12	0.600
39	29.675	13.499	0.042	0.256	0.331	0.150	0.289	0.339	0.14	0.600
40	31.005	13.701	0.040	0.253	0.326	0.137	0.281	0.333	0.13	0.580

4.3 ASRM NOZZLE EROSION

Erosion depths calculated for the ASRM nozzle are presented in Figure 85. This figure presents erosion depth as a function of station. The figure also includes the material thickness at each analysis location. Results are presented for both thermochemical erosion and combined thermochemical and particle erosion. Station 6 is the nozzle throat. Following are comments relative to these results.

1. The magnitude and characteristics of the thermochemical erosion are consistent with those predicted and measured in the MNASA nozzle.
2. The augmented heating at the exit cone material interface does not appear to cause excessive erosion.
3. The particle erosion in the throat entrance regions is extremely severe and probably excessive.
4. The particle erosion in the nozzle exit cone is not calculated to be excessive.

This erosion was calculated based on the "backed out" mass fluxes from the MNASA nozzle. Figure 86 compares the shape for the two nozzles. This figure presents surface angle as a function of normalized axial position. The surface angle is presented beginning at the nozzle throat and continuing to the exit plane of the nozzle. The axial position is normalized based on the axial length from the throat to the exit plane. Since the nozzle contours are not identical, the mass flux results were applied to the ASRM nozzle based on the local surface angle, i.e., an MNASA exit cone mass flux level was applied at the location in the ASRM nozzle which had the same surface angle. This figure shows that the ASRM would be expected to experience less severe erosion than the MNASA and it would occur further aft.

Figure 87 presents the TAD's calculated for the ASRM nozzle. Again results are presented at the end of the motor firing and after two minutes of cool down. This plot also includes the local material thickness for comparison. A summary of the calculated erosion and TAD results is presented in Table 11. This table also includes the safety margin calculated for each of the analysis positions. For these calculations the safety margin is defined as follows:

$$\text{safety margin} = \left\{ \frac{t_l}{2x_e + 1.25x_c + d_i} \right\} - 1$$

where,

t_l	=	liner thickness
e	=	erosion depth
c	=	char depth at the end of burn
d_i	=	depth to the 100° F isotherm for analysis stations 1 through 13 and depth to the 350° F isotherm for analysis stations 14 through 17.

Based on this definition of safety margin, it appears the design is inadequate throughout the nozzle. This is especially true in the entrance regions of the nozzle where particle

impact effects were calculated to be the most severe. For the majority of the remaining analysis positions the safety margin is only a small negative number (or positive in some cases) and is therefore not as great of a concern.

4.4 ASRM FLEX SEAL RESPONSE

The response of the flex seal for the ASRM nozzle was analyzed using the polyisoprene model described in Appendix B and the convective heating conditions described in section 3. As described in Appendix B, the two dimensional conduction effects of the polyisoprene/carbon phenolic configuration do not appear significant. Therefore, these material response calculations were performed with the CMA computer code rather than with ASTHMA. Results from this calculation are presented in Figure 88. This figure presents the recession response for both the polyisoprene and the carbon phenolic. The polyisoprene is calculated to recede at very rapid rates. In fact, the calculation shows the polyisoprene should ablate completely through in about 80 seconds. This calculation is probably conservative in several respects:

1. The polyisoprene model was developed from the MNASA motor data for which there was probably particle erosion present. Particle impact conditions for the ASRM flex seal location should be significantly less. Because of this, the model may be somewhat conservative and tend to over predict recession in a pure convective/radiative heating environment.
2. The modeling of the polyisoprene does not account for the substantial differential recession which will occur between the polyisoprene and the carbon phenolic. This difference in recession can allow the carbon phenolic to shield the polyisoprene from both the convective and radiative heating environments. This effect was not taken into account in these analyses.

In spite of these conservative aspects of the calculation, it is obvious that the flex seal is a potential problem area and needs additional attention. Section 6 provides some recommendations for addressing the flex seal.

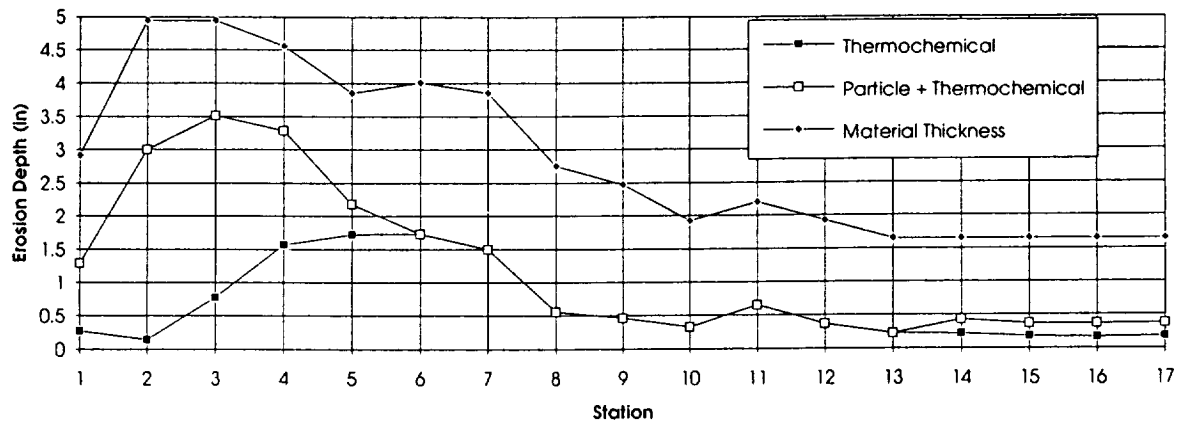


Figure 85. Calculated Erosion Depths for the ASRM Nozzle

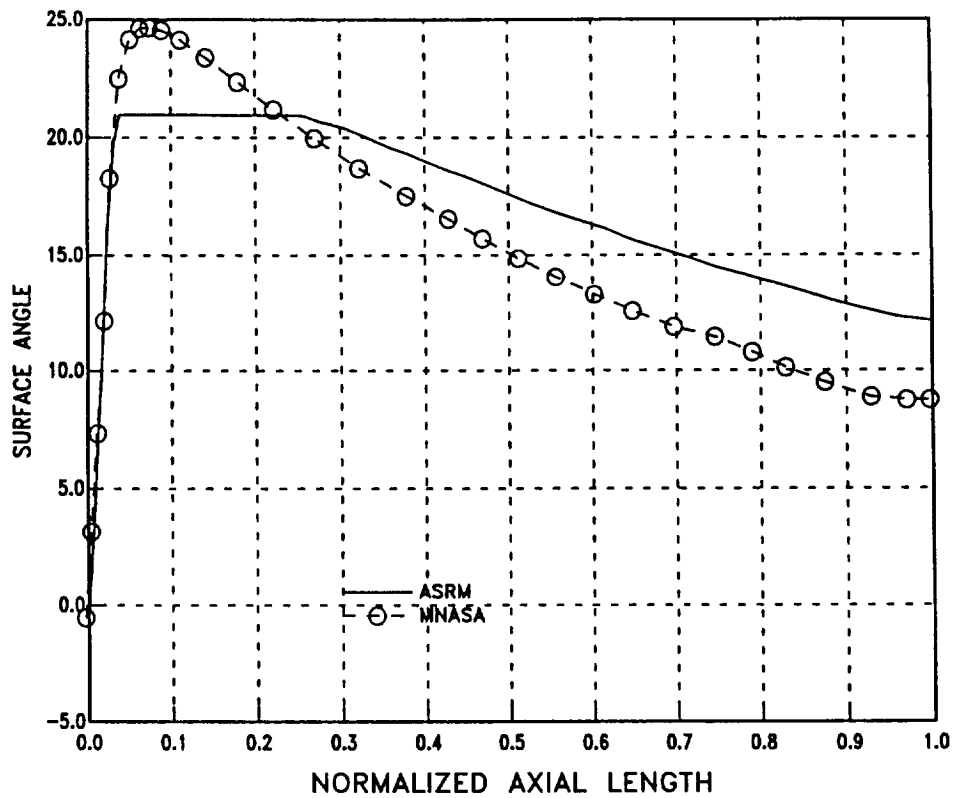


Figure 86. Surface Angles for the MNASA and ASRM Nozzles

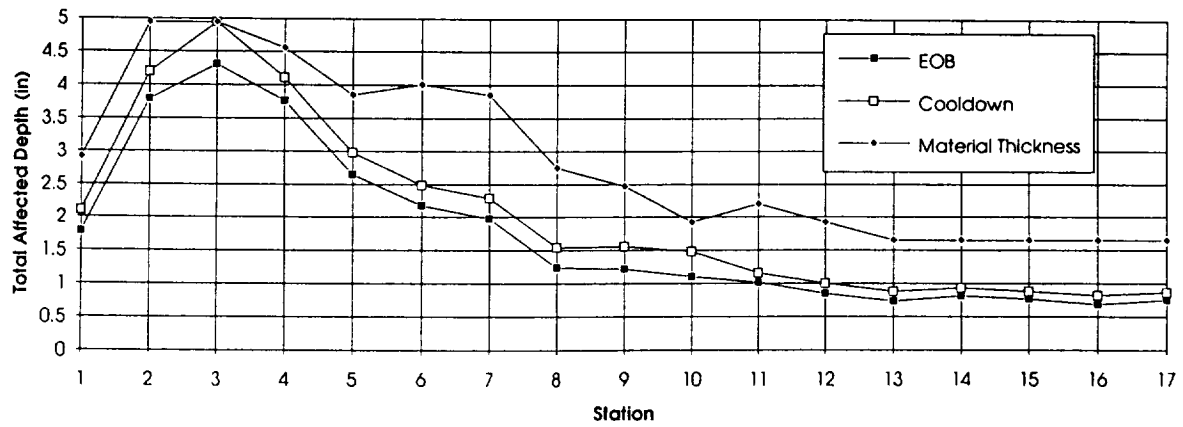


Figure 87.TAD for ASRM Nozzle

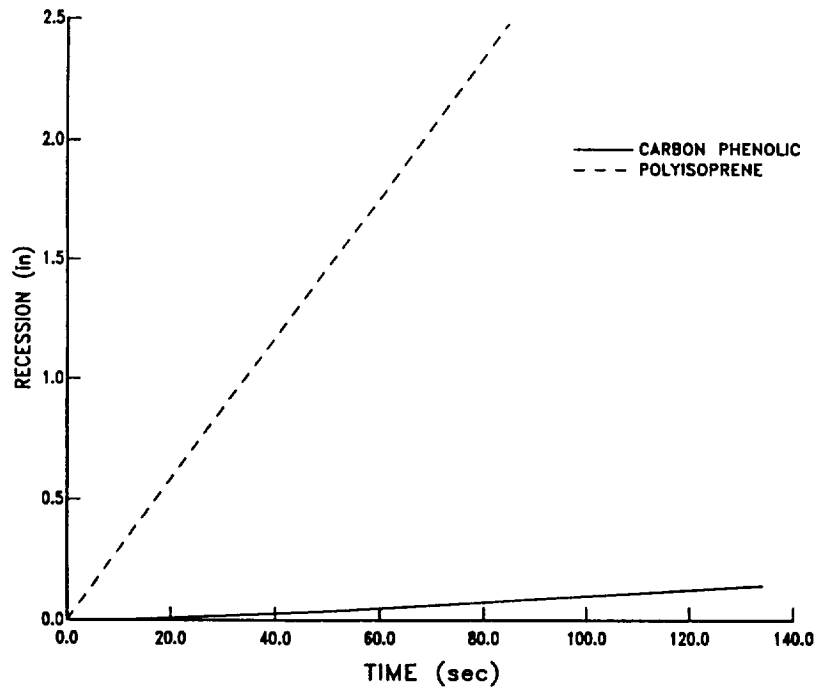


Figure 88. ASRM Nozzle Flex Seal Recession

			Thermochemical Erosion			Thermochemical & Particle Erosion			
Station	Axial Position (in)	Radial Position (in)	Erosion Depth (in)	TAD (in)		Erosion Depth (in)	TAD (in)		Safety Margin
				EOB	Cooldown		EOB	Cooldown	
1	429.23	44.84	0.270	1.255	1.688	1.293	1.778	2.101	-0.2436
2	422.17	38.99	0.141	1.222	1.666	3.003	3.792	4.198	-0.3640
3	423.69	36.01	0.772	1.645	2.098	3.512	4.307	4.940	-0.4297
4	427.01	32.86	1.569	2.040	2.346	3.286	3.763	4.113	-0.4261
5	432.49	30.13	1.722	2.183	2.512	2.180	2.645	2.976	-0.3099
6	437.34	28.39	1.733	2.176	2.487	1.733	2.176	2.487	-0.1231
7	446.01	27.24	1.503	1.978	2.289	1.503	1.978	2.289	-0.0878
8	450.83	28.32	0.554	1.236	1.546	0.554	1.236	1.546	-0.0034
9	462.44	32.78	0.461	1.220	1.554	0.461	1.220	1.554	-0.1200
10	479.59	39.36	0.326	1.105	1.482	0.326	1.105	1.482	-0.2216
11	490.46	43.50	0.654	1.014	1.158	0.654	1.014	1.158	0.0857
12	511.77	51.05	0.364	0.844	1.002	0.364	0.844	1.002	-0.0224
13	541.11	60.13	0.220	0.730	0.879	0.220	0.730	0.879	-0.1614
14	544.00	60.81	0.206	0.719	0.866	0.428	0.814	0.933	-0.0638
15	569.00	67.57	0.166	0.685	0.826	0.366	0.763	0.879	-0.0014
16	577.52	69.54	0.159	0.679	0.819	0.366	0.757	0.871	0.0001
17	586.00	71.46	0.143	0.664	0.802	0.367	0.751	0.863	0.0006

930907

Table 11. Erosion, TAD and Margin of Safety Summary for the ASRM Nozzle

5.0 CONCLUSIONS

In conclusion, this study has been extremely beneficial in increasing the understanding of the MNASA motor and applying its results to the development of the ASRM motor. Several key aspects of the MNASA calculations include:

1. The analytical procedures used in performing these analysis do an excellent job of predicting the heating and material response for the MNASA nozzle.
2. The method developed to account for the augmented heating at the exit cone material interface does an adequate job of predicting the measured material response.
3. The particle flow calculations and mechanical erosion predictions used in this study represent an improvement over standard procedures used in the solid rocket motor industry. Only the larger particle sizes (120 μm) are calculated to impact the nozzle in the throat entrance region. The calculated results were found to be consistent with the measured data.
4. No particle impacts were calculated to occur in the nozzle exit cone. However, the measured data suggests impacts do occur. To account for this modeling deficiency an empirical approach was used to "backout" impacting particle mass fluxes.
5. The TAD's calculated for the MNASA motor compare very well to the measured values for the MX4996 material. The TAD's are significantly underpredicted for the FM5939 material.
6. A material response model was developed for the polyisoprene flex seal material from the MNASA motor firing data. This model treats the polyisoprene as a surface sublimator. However, because of uncertainties in the MNASA environment, this model may be somewhat conservative when applied to the ASRM motor.

Using the models developed and the lessons learned from the MNASA nozzle analysis, similar analyses were conducted for the ASRM nozzle. Based on these calculations the following conclusions can be drawn:

1. Particle erosion will cause excessive material removal in the throat entrance region and therefore, large negative margins of safety.
2. Augmented heating at the exit cone material interface will cause only slightly excessive erosion (based on small negative safety margins).
3. Particle impacts in the exit cone will not cause excessive erosion (safety margins of about zero).
4. The polyisoprene in the flex seal is calculated to ablate completely through in only 80 seconds and appears to be a significant problem area.

6.0 RECOMMENDATIONS

There are several aspects of the results which suggest that further studies are needed to better quantify margins of safety for the ASRM nozzle. The following recommendations, in order of importance, describe areas which require additional study.

1. Additional effort needs to be directed toward understanding the polyisoprene material response. This should include testing of the polyisoprene in controlled environments so that the material recession mechanisms can be better understood. At this point it is not clear if the material behaves as a surface sublimator or if the shear environment plays an important role in the material removal. Additionally, the role of thermochemical erosion is not known. The best place to quantify these effects is in arc plasma generator tests where the convective heating and thermochemical environments can be controlled and made to duplicate the environments of the ASRM nozzle.
2. The particle erosion of the throat entrance region needs to be better understood. In order to further validate the procedures used in this study, the same procedures should be evaluated against the RSRM motor firing data. This motor in many respects does a much better job of duplicating the erosion environment of the ASRM than does the MNASA motor. Comparing to data from this motor should add a great deal to understanding the erosion in the ASRM nozzle as well as understanding the accuracy of the analysis procedures.
3. Material response models for the MX4996 and FM5939 need to be developed so that margins of safety, especially with regard to char depth can be more accurately predicted. These models should be developed with the use of analog and arc heater testing so that material response data from representative and well quantified environments are used to understand the material response. This model development is especially needed for the FM5939 since there was such a large difference in calculated and measured TAD's for this material.

REFERENCES

1. Tran, Tony, Final Test Report for ASRM 48-5 Motor (Nozzle Material Evaluation Test), June 18 1992, Gencorp Aerojet ASRM Division, Iuka Mississippi.
2. Aerotherm Corporation, Nozzle Aero Thermochemistry (NAT) Computer Code, Version 1.0, April 1992, Aerotherm Corporation, Huntsville, Alabama.
3. Baker, P.J. and B.W. Martin, "Heat Transfer in Supersonic Separated Flow Over a Two Dimensional Backward-Facing Step," International Journal of Heat and Mass Transfer, 9:1081-1088, 1966.
4. Lamb, J.P. and Hood, C.G., "Prediction of Heat-Transfer Rates Downstream of a Backstep in Supersonic Turbulent Flow", ASME Paper No. 70-HT/SpT-39 (June 1970).
5. Nestler, D.E., et al, "Heat Transfer to Steps and Cavities in Hypersonic Turbulent Flow," AIAA Journal, Vol. 7, No. 7, July 1969, pp. 1368-1370.
6. Lamb, J.P., "Convective Heat Transfer Correlations for Planar, Supersonic, Separated Flows", Journal of Heat Transfer, Volume 102, May 1980, pp. 351-356.
7. Salita, Mark, "Application of Internal Flow Field Modeling To Solid Rocket Motor Design", Pages 93 -115, CPIA Publication 512, JANNAF Combustion Subcommittee Workshop, July 14-15, 1988, Boston, Massachusetts.
8. Hunter, S.C., Cherry, S.S., Waldman, C.H., Kilegel, J.R., "One Dimensional Reacting Three-Phase Flow with Mass Transfer Between Phases, Volume I - Final Technical Report, AFRPL-TR-81-103, April 1982.
9. Chiba, Z. , Johnson, P.A., Abbett, M.J., Particle Impact Erosion Volume I: Recession Prediction Methodology for Rocket Nozzle Entrance and Throat Regions, May 1983, AFRPL TR-83-013, Acurex Corporation Aerotherm Division, 485 Clyde Ave., Mountain View, CA 94042.
10. Wernimont, Eric, Personal Communication - Telecon on July 20, 1993 with Forrest Strobel.
11. "Users Manual: Aerotherm Charring Material Thermal Response and Ablation Program (CMA87S)", Acurex Report UM-87-13/ATD, November 1987.
12. "Users Manual: Aerotherm Axi-Symmetric Transient Heating and Material Ablation Program (ASTHMA88), Acurex Report Um-88-11/ATD, October 1988.

APPENDIX A

INTERIM THERMAL RESPONSE MODELS FOR MX4996 AND FM5939 CARBON PHENOLICS

This Appendix presents the interim thermal response models which have been developed to model the standard density MX4996 carbon phenolic and the low density FM5939 carbon phenolic used in the MNASA ASRM 48-5 nozzle and the full scale ASRM nozzle. These models used thermal conductivity and TGA data generated at Southern Research Institute (SRI), Birmingham, Alabama. Specific heat of the materials was estimated based on similarity to other carbon phenolic materials. Additionally, chemical composition of the virgin materials was measured under this program. These measurements were made at Galbraith Laboratories in Knoxville, Tennessee. The composition of the pyrolysis gases have been inferred from these measurements of virgin material composition and the assumption that the char materials are composed entirely of carbon. It should be stressed that these are only interim models and that more data needs to be gathered before thermal response calculations can be made with a high level of confidence. This data should be in the form of analog tests at Southern Research Institute and arc plasma tests conducted at Aerotherm.

The interim thermal response model developed for MX4996 carbon phenolic is presented in Tables A-1 through A-6 and Figures A-1 through A-3. Data is presented in both tabular and graphical form. The char thermal conductivities used in this model were estimated based on dynamic thermal conductivities determined by Aerotherm for other similar carbon phenolics. These estimated values were used in place of the laboratory measured values since the laboratory values traditionally underpredict thermal response data by a significant amount. A comparison of the estimated and measured values is provided in Figure A-3.

The interim thermal response model developed for the low density FM5939 carbon phenolic is presented in Tables A-7 through A-12 and Figures A-4 through A-6. The conductivities in this case are taken from the SRI measured data. Estimated conductivities were not developed since the low density material was believed to be significantly different from other materials for which models were available.

Reaction	Initial Density	Residual Density	Pre-Expo Factor	Dens Factor Expon	Act Energy Factor	Min React Zone Temp
1	WZERO(I) (Lbm/Ft ³)	RR(I) (Lbm/Ft ³)	B(I) (1/SEC)	PSI(I) (-)	E(I) (DEGR)	TRES(I) (DEGR)
A	3.6202	.00000	334.19	1.2900	9702.2	540.00
B	2.5668	.00000	.51330E+12	1.5200	39034	1008.0
C	169.45	146.55	15.590	1.2200	12297	729.00

WINTL = 87.818 (Lbm/Ft³)
GAMA = .500

TGA Data for MX 4996A
20 Deg C/Min Heating Rate

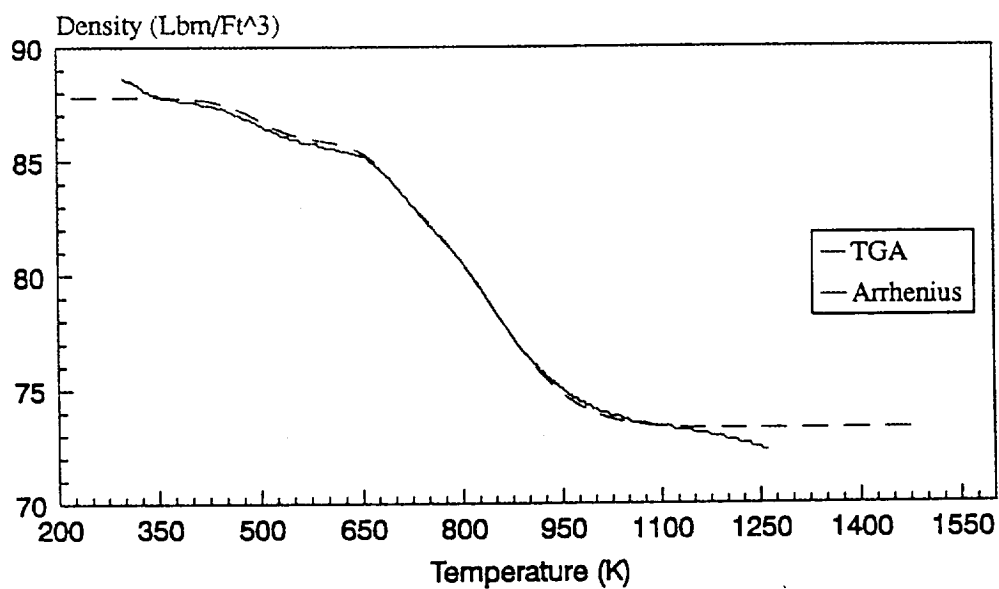


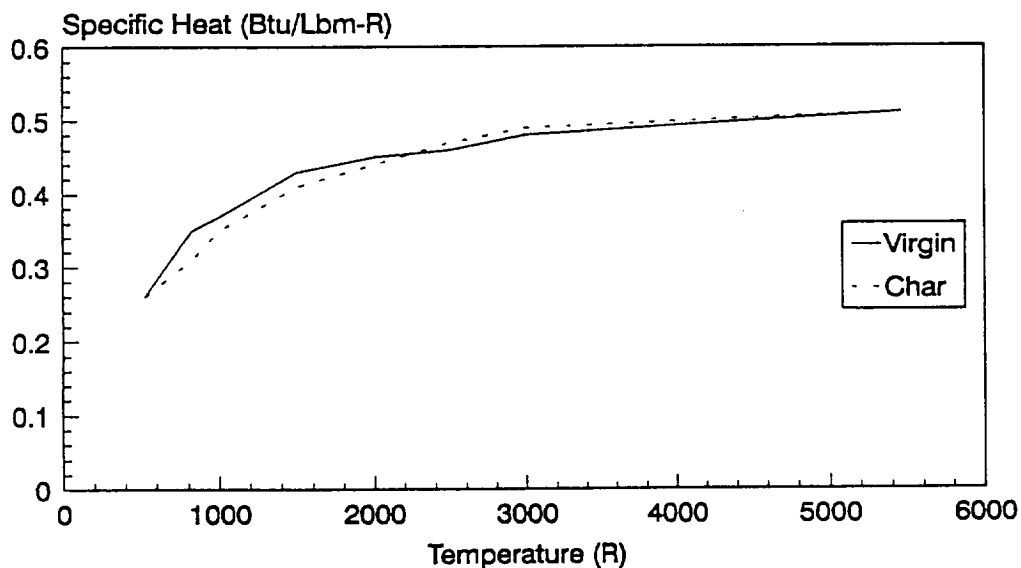
Figure A-1. Comparison of Measured and Calculated TGA Data for MX4996 Carbon Phenolic

Table A-2. Elemental Composition for MX4996 Carbon Phenolic

Element	Virgin	Pyrolysis Gas	Char
% Carbon	88.52	58.94	100
% Nitrogen	0.50	3.20	
% Oxygen	3.65	23.19	
% Hydrogen	2.31	14.67	
% Undetermined	5.02		

Table A-3. Estimated Specific Heat for MX4996 Carbon Phenolic

Temperature (R)	Virgin (Btu/Lbm-R)	Char (Btu/Lbm-R)
530	0.26	0.26
824	0.35	0.31
1000	0.37	0.35
1500	0.43	0.41
2000	0.45	0.44
2500	0.46	0.47
3000	0.48	0.49
5460	0.51	0.51



Estimated Values From Similar Materials

Figure A-2. Estimated Specific Heat for MX4996

Table A-4. RESIN DATA

Type: SC1008
 Mass Fraction: 35% (Assumed)
 Resin Heat of Formation: -1080 Btu/Lbm (Assumed)
 Material Heat of Formation: -378 Btu/Lbm

Table A-5. Virgin Thermal Conductivity for MX4996 Carbon Phenolic

Temperature (R)	Across Ply (Btu/Ft-Sec-R)	Fill (Btu/Ft-Sec-R)
460	1.505E-04	2.373E-04
610	1.505E-04	2.373E-04
810	1.505E-04	2.732E-04
935	1.505E-04	2.917E-04
1410	1.505E-04	2.917E-04
5460	1.505E-04	2.917E-04

NOTE 1: The values listed above are measured values up to a temperature of 1000 F

Table A-6. Estimated Char Thermal Conductivity

Temperature (R)	Across Ply Conductivity (Btu/Ft-Sec-R)	Fill Conductivity (Btu/Ft-Sec-R)
460	9.64E-04	2.33E-03
685	9.64E-04	E-2.3303
985	1.22E-03	2.74E-03
1935	1.27E-03	2.63E-03
2960	1.27E-03	2.43E-03
3410	1.36E-03	2.72E-03
4260	2.09E-03	4.67E-03
5160	2.77E-03	6.90E-03
5460	3.00E-03	7.73E-03

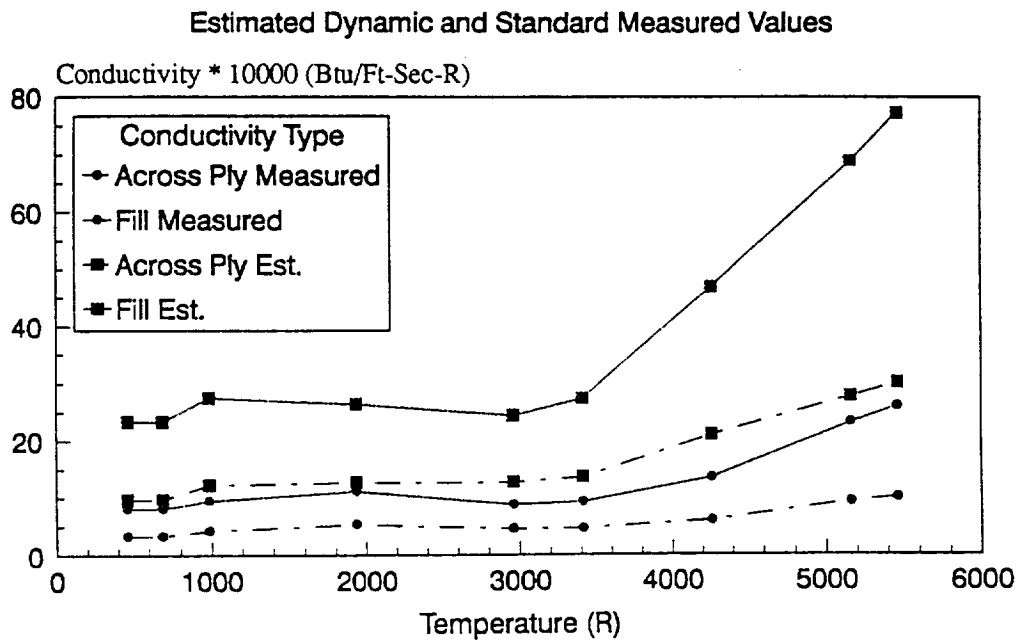


Figure A-3. Thermal Conductivity of MX4996 Char Material

Table A-7. Decomposition Kinetics for FM5939 Low Density Carbon Phenolic

Reaction	Initial Density	Residual Density	Pre-Expo Factor	Dens Factor Expon	Act Energy Factor	Min React Zone Temp
I	WZERO(I) (Lbm/Ft ³)	RR(I) (Lbm/Ft ³)	B(I) (1/SEC)	PSI(I) (-)	E(I) (DEGR)	TRES(I) (DEGR)
A	2.1890	.00000	917.51	1.3100	10646.	540.00
B	8.9951	.00000	.20191E+10	2.2700	32106.	927.00
C	114.74	100.09	5026.1	1.6600	19562.	927.00

Initial Composite Density WINTL= 62.962 (Lbm/Ft³)
 GAMA = .500

TGA Data for FM5939 LDC
20 Deg C/Min Heating Rate

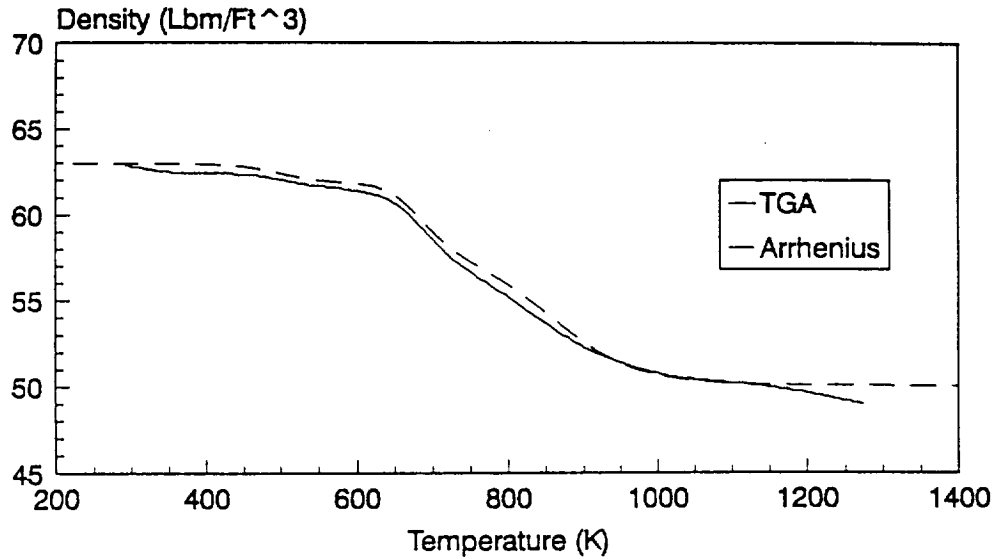


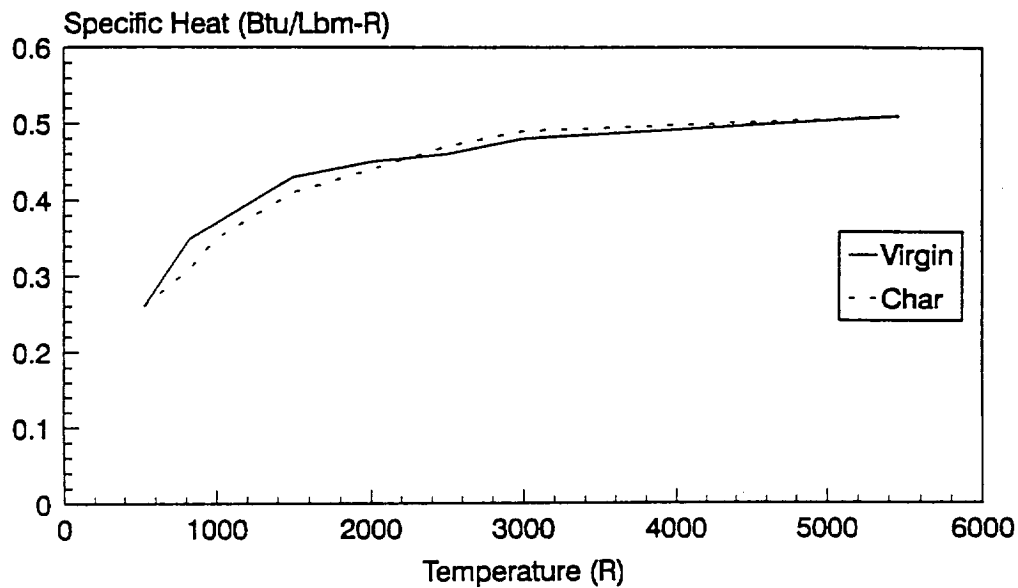
Figure A-4. Comparison of Measured and Calculated TGA Data for
 FM5939 Low Density Carbon Phenolic

Table A-8. Elemental Composition for FM5939 Low Density Carbon Phenolic

Element	Virgin	Pyrolysis Gas	Char
% Carbon	86.39	55.55	100
% Nitrogen	0.83	4.23	
% Oxygen	5.01	25.69	
% Hydrogen	2.83	14.53	
% Undetermined	4.94		

Table A-9. Estimated Specific Heat for FM5939 Low Density Carbon Phenolic

Temperature (R)	Virgin (Btu/Lbm-R)	Char (Btu/Lbm-R)
530	0.26	0.26
824	0.35	0.31
1000	0.37	0.35
1500	0.43	0.41
2000	0.45	0.44
2500	0.46	0.47
3000	0.48	0.49
5460	0.51	0.51



Estimated Values From Similar Materials

Figure A-5. Estimated Specific Heat of FM5939 Low Density Carbon Phenolic

Table A-10 Resin Data

Type: 91 LD
 Mass Fraction: 35% (Assumed)
 Resin Heat of Formation: -1080 Btu/Lbm (Assumed)
 Material Heat of Formation: -378 Btu/Lbm

Table A-11. Virgin Thermal Conductivity for FM5939 Low Density Carbon Phenolic

Temperature (R)	Across Ply Conductivity (Btu/Ft-Sec-R)	Fill Conductivity (Btu/Ft-Sec-R)
460	8.102E-05	1.331E-04
590	8.102E-05	1.331E-04
760	9.722E-05	1.528E-04
960	9.954E-05	1.713E-04
1260	1.065E-04	1.852E-04
1460	1.100E-04	1.910E-04
5460	1.100E-04	1.910E-04

NOTE 1: The values listed above are measured values up to a temperature of 1000 F

Table A-12. Char Thermal Conductivity for FM5939 Low Density Carbon Phenolic

Temperature (R)	Across Ply Conductivity (Btu/Ft-Sec-R)	Fill Conductivity (Btu/Ft-Sec-R)
460	*5.505E-05	1.331E-04
630	*21.063E-05	5.093E-04
1200	*30.862E-05	6.944E-04
1685	*34.103E-05	7.639E-04
2610	*35.610E-05	6.481E-04
3460	*34.376E-05	6.944E-04
3960	*38.732E-05	8.333E-04
5260	*57.422E-05	14.815E-04

*-Estimated value

NOTE 2: Fill conductivity values were taken from measured data pre-charred at 3500 F

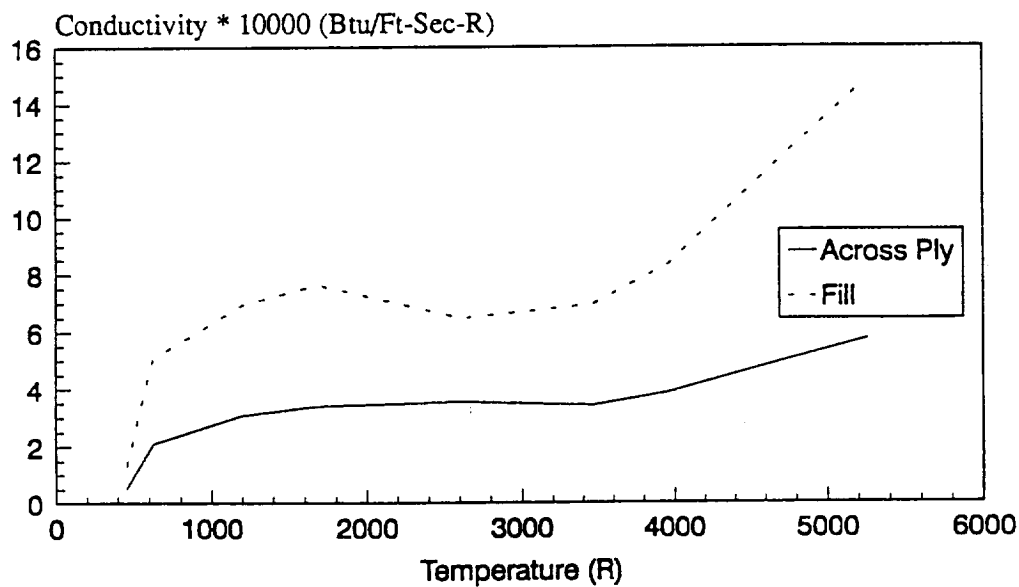


Figure A-6. Thermal Conductivity for FM5939 Low Density Carbon Phenolic Char

APPENDIX B

POLYISOPRENE ABLATION MODEL

A material response model has been developed to predict the behavior of the polyisoprene flex seal material. An initial model was developed which utilized an Arrhenius fit of polyisoprene TGA data. This model treated the material as a decomposing ablator. Thermochemistry tables were generated with the ACE module of the NAT code. These tables treated the char material as pure carbon and the pyrolysis gas as an equilibrium mixture with five moles of carbon to eight moles of hydrogen. To obtain a reasonable match of the measured erosion data, a surface fail temperature of 4500° R was used. Because of the high fail temperature, this was not believed to be a good material model in that excessively high surface temperatures would be calculated.

Because of the lack of realism of the fail temperature model, this approach was abandoned. A new model was developed which treated the material as a surface sublimator. With this approach the surface recession rate of the material is assumed to be a function of the surface temperature. This behavior was modeled with a zeroth order Arrhenius rate expression of the form:

$$\dot{s} = A \exp(-B/T_w)$$

where,

- \dot{s} is the surface recession rate
- A is the pre-exponential factor
- B is the activation energy
- T_w is the wall temperature

For this model, the material was assumed to ablate between temperatures of 1500° R and 1600° R. This temperature range was selected based on TGA results which showed the material to be fully decomposed at approximately these temperatures. Using this approach the following Arrhenius expression was developed:

$$\dot{s} = 1.0037E+29 \exp(-110,530/T_w)$$

With this expression, pseudo thermochemistry tables were developed which are compatible with the CMA computer code. Additional details on this procedure are contained in Reference B-1. CMA still uses a surface energy balance technique to calculate recession rate; however, it is significantly simplified compared to the most general case. The energy balance which is performed is illustrated in Figure B-1. This can be written in equation form as :

$$q_{\text{conv}} + q_{\text{rad}} - (\rho s)_w H_w - \sigma \epsilon T_w^4 + \dot{m}_c H_c = q_{\text{cond}}$$

All of these terms are defined as discussed in the CMA User's Manual with the exception of H_w which is given by:

$$H_w = \frac{H_{\text{gas}} + B' H_{\text{iso}}}{1 + B'}$$

where,

H_{gas} = enthalpy of propellant edge gases

H_{iso} = enthalpy of polyisoprene gases

A separate routine has been written which generates the necessary B' tables. Instead of non dimensional pyrolysis gas rate B_g' being an independent variable, the transfer rate h/C_p is the independent variable. The last important aspect in the model development is the determination/selection of a heat of formation, ΔH_f° . The heat of formation is used in determining the enthalpy of the char material, H_c . H_c is given by the following expression:

$$H_c = \Delta H_f^\circ + \int_0^{T_w} C_p dT$$

With this approach, a heat of formation was determined in an iterative fashion. A value of -4500 BTU/lbm was found to give reasonably good agreement with the polyisoprene erosion data taken from the MNASA ASRM 48-5 motor firing. Results using this model are presented in Figures B-2 and B-3. Figure B-2 presents the calculated erosion as a function of time. Total erosion is calculated to be slightly greater than 0.95 inches. This is approximately the amount measured in the ASRM 48-5 firing. Figure B-3 shows calculated temperature profiles within the material at various points in time. Notice the extremely thin heat affected depth which is calculated. This is because of the conductivity levels selected to model this material. Figure B-4 shows conductivity as a function of temperature. These values are for an ASRM internal insulator (RP7136) and were taken from Reference B-2. Of course, conductivity values above about 1600° R are meaningless in that these material temperatures are never attained.

Two dimensional conduction effects were considered a possible contributor to the polyisoprene material response. To investigate their effects, a two dimensional ASTHMA model of the flex seal specimen for the MNASA motor was constructed. This model is presented in Figure B-5. This figure shows the grid used to perform the calculation. The model includes both polyisoprene and carbon phenolic materials. These materials are contained in alternating columns of the grid. Thermal and recession calculations were performed with this grid to calculate the polyisoprene results. This calculation yielded 0.969 inch of recession for the polyisoprene. This amount is only 1.4% greater than the 0.956 inch calculated with the one dimensional approach. Based on this result it was

decided that two dimensional effects were insignificant and therefore all remaining calculations for the polyisoprene were performed with the one dimensional CMA code.

It should be stressed that this model is a "pure fabrication" in that it is only a best guess at this point. Hopefully, this best guess model will have proper sensitivity to the important parameters such that it can be used with reasonable accuracy for the full scale motor. Again, it should be stressed that this model is merely an interim and in no way should it replace the material characterization effort which is needed to better understand and model this material's behavior.

References

- B-1. Kelly, R.D., Strobel, F.A., "Duroid 5667M Ablation Model Development", Acurex Final Report 86-21/ATD, November 1986, Acurex Corporation, Huntsville, Alabama.
- B-2. Risch, T.K., Beck, R.A.S., Project Review Internal Insulation for the Advanced Solid Rocket Motor (ASRM), August 1992, Aerotherm Corporation, Mountain View, California.

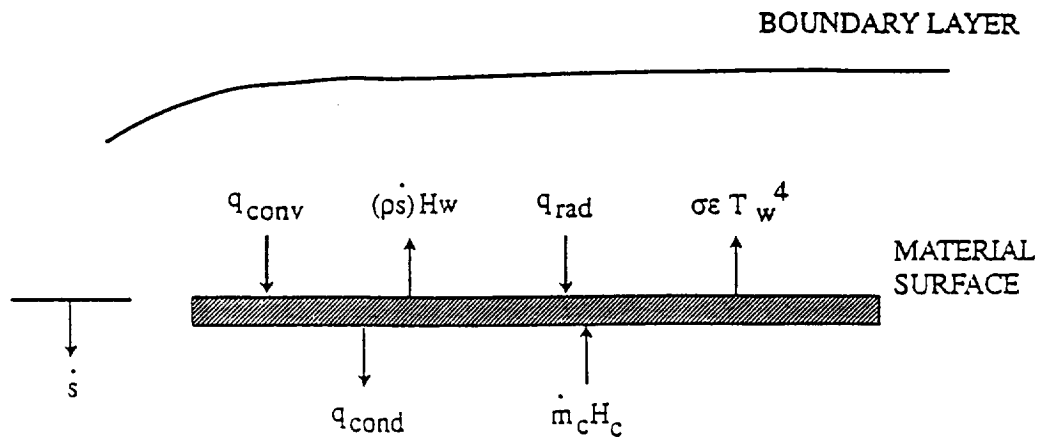


Figure B-1. Polyisoprene Surface Energy Balance

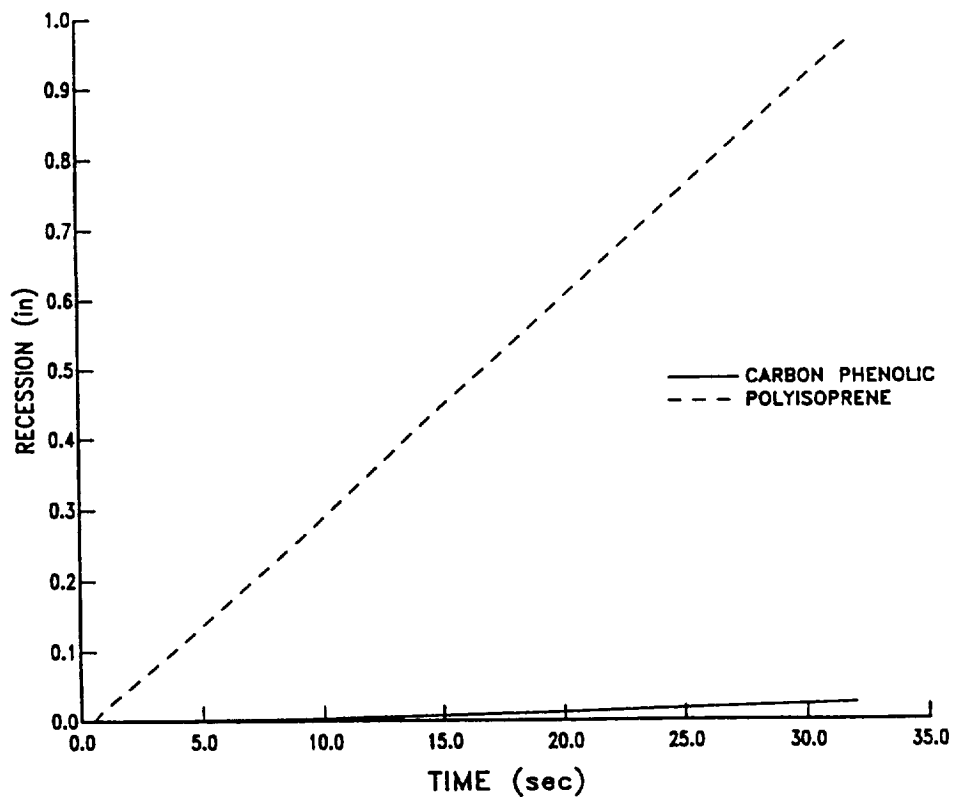


Figure B-2. Polyisoprene Recession History

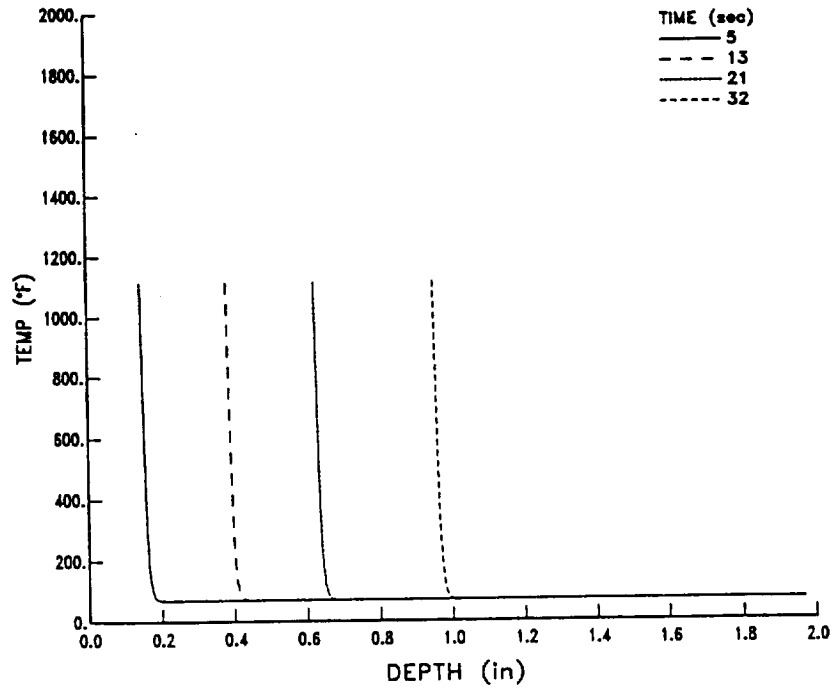


Figure B-3. Polyisoprene In-depth Temperatures

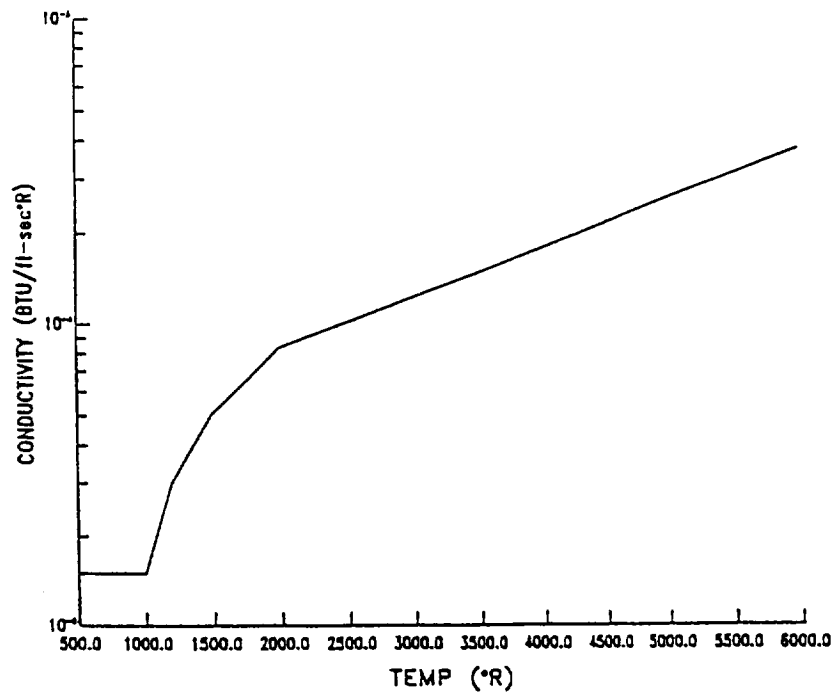


Figure B-4. Polyisoprene Thermal Conductivity

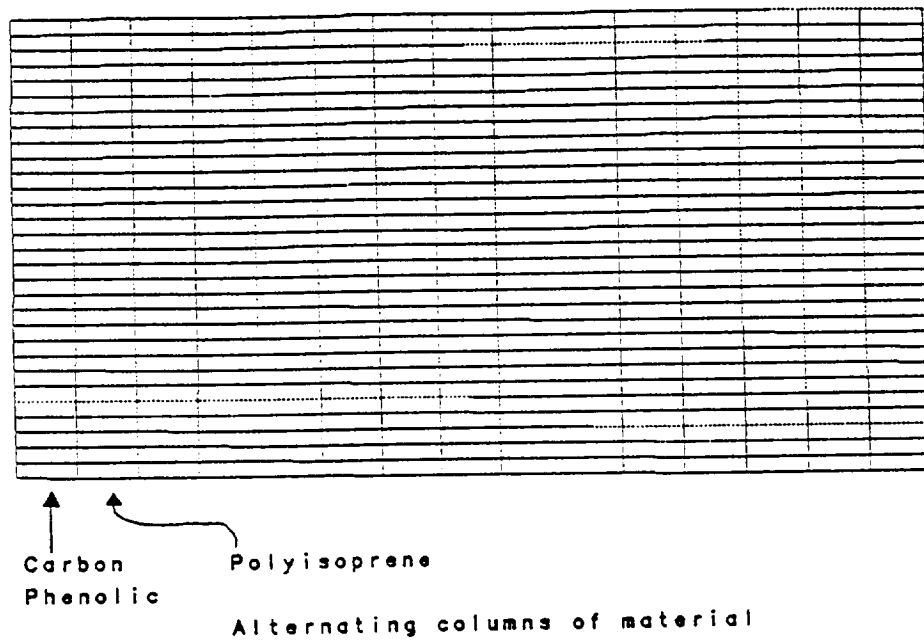


Figure B-5. ASTHMA Analysis Grid for MNASA Flex Seal Specimen



Report Documentation Page

1. Report No. Final Report		2. Government Accession No.		3. Recipient's Catalog No.	
4. Title and Subtitle Final Technical Report for ASRM Nozzle Thermal Analysis				5. Report Date November 1993	
				6. Performing Organization Code	
7. Author(s) Mr. Forrest Strobel & Ms. Belinda King				8. Performing Organization Report No.	
				10. Work Unit No.	
9. Performing Organization Name and Address Aerotherm Corporation 1500 Perimeter Parkway, Suite 225 Huntsville, AL 35806				11. Contract or Grant No. NAS8-39611	
				13. Type of Report and Period Covered Final Technical Report	
12. Sponsoring Agency Name and Address NASA/MSFC Marshall Space Flight Center, AL 35812				14. Sponsoring Agency Code	
15. Supplementary Notes					
16. Abstract This report describes results from the Nozzle Thermal Analysis contract which has been performed to support NASA/Marshall Space Flight Center in the development of the Advanced Solid Rocket Motor (ASRM). The emphasis of this study has been directed to four potential problem areas of the nozzle. These areas are: 1) the submerged nozzle region containing the flex seal, 2) the nozzle entrance region, 3) the material interface region in the nozzle exit cone, and 4) the aft region of the exit cone. This study was limited throughout by inadequate material response models, especially for the polyisoprene flex seal and the low density carbon phenolic used in the exit cone. Thermal response and particle erosion calculations were performed for each of the potential problem areas. Results from these studies showed excessive erosion (large negative safety margins) to occur in the flex seal and nozzle entrance regions. The exit cone was found to be marginally adequate (near zero safety margins) and the material interface region was found not to be a problem.					
17. Key Words (Suggested by Author(s)) ASRM Nozzle, Thermal Analysis, Flow Field Analysis, Material Models				18. Distribution Statement Unclassified, Unlimited	
19. Security Classif. (of this report) Unclassified		20. Security Classif. (of this page) Unclassified		21. No. of pages	
				22. Price	